DROP-ON-DEMAND INKJET

DROP FORMATION AND DEPOSITION

A Dissertation
Presented to
The Academic Faculty

by

HONGMING DONG

In Partial Fulfillment
of the Requirements for the Degree
DOCTOR OF PHILOSOPHY in the
School of POLYMER, TEXTILE AND FIBER ENGINEERING

Georgia Institute of Technology
AUGUST 2006

DROP-ON-DEMAND INKJET

DROP FORMATION AND DEPOSITION

Approved by:

Dr. Wallace W. Carr, Advisor
School of Polymer, Textile and Fiber Engineering
Georgia Institute of Technology

Dr. Mary Lynn Realff
School of Polymer, Textile and Fiber Engineering
Georgia Institute of Technology

Dr. David G. Bucknall
School of Polymer, Textile and Fiber Engineering
Georgia Institute of Technology

Dr. F. Joseph Schork
School of Chemical and Biomolecular Engineering
Georgia Institute of Technology

Dr. Karl I. Jacob
School of Polymer, Textile and Fiber Engineering
Georgia Institute of Technology

Dr. Jeffrey F. Morris
Benjamin Levich Institute and Department of Chemical Engineering
City College of New York

Date Approved: June 30, 2006

ACKNOWLEDGEMENTS

First, I would like to thank my advisor, Dr. Wallace W. Carr. During the last four years, Dr. Carr has guided me with his profound academic knowledge and rich experience in a variety of ways. From the selection of courses to the writing of my dissertation and papers, from experimental setup to discussion and analyses of the experimental results, Dr. Carr has put significant effort into my graduate study and research. I really admire his enthusiasm for scientific research and his kind patience with students.

I would also like to thank Dr. Jeffrey F. Morris for his active and efficient involvement in my research. His ideas often encouraged me to go forward in my research. I also acknowledge Dr. David G. Bucknall, Dr. F. Joseph Schork, Dr. Mary Lynn Realff and Dr. Karl I. Jacob for their helpful instruction and valuable feedback to my research. In addition, I thank my research group members, Dr. Heungsup Park, Dr. Hyunyoung Ok, and Mr. Xi Wang for their friendly cooperation.

I would also thank Dr. Ming Xu of Sawgrass, Inc., and Dr. Yong Zhou of Trident-ITW for providing me with useful information regarding ink and printheads. In addition, I am grateful for the kind assistance of Mr. Chris Betz and Mr. Dan Brooks, who help me build the experimental setup.

Finally, I would like to thank my parents, Xuecai Dong and Yulin Zhang, and my wife, Fenghe Lu. Without their strong and continuous support, I would not have been able to overcome many hardships.

TABLE OF CONTENTS

Page

LIST OF TABLES

LIST OF FIGURES

Page

SUMMARY

An imaging system has been developed to visualize Drop-on-demand (DOD) inkjet drop formation and drop impaction on substrates for drop sizes and impaction speeds of the magnitudes encountered in applications. Using a pulsed laser, a low-speed charge-coupled-device (CCD) camera, and signal generators, the imaging system based on flash photography is shown to be able to obtain sharp images with a temporal resolution of 200 ns and a spatial resolution of 0.81 μm/pixel. Several steps are taken to minimize the "first drop problem" so that drop formation is reproducible with a positional variation of 1 μm. In addition, a waveform generator and an amplifier are used to produce the required waveform since the optimal driving signal varies with the printhead and ejected liquid.

First, the dynamics of drop-on-demand (DOD) drop formation was studied experimentally using this imaging system with an interframe time of 1 μs. Using a piezoelectrical actuated inkjet printhead with the nozzle orifice diameter of 53 μm, experiments were conducted over a range of viscosities (1.0 - 5.0 cP) and surface tensions (35 - 73 mN/m). The effects of the driving signal, which controls the piezoelectric transducer that produces the pressure pulse to drive the liquid from the reservoir through the orifice, have been examined along with those of liquid properties. The main stages of DOD drop formation, including ejection and stretching of liquid, pinch-off of liquid thread from the nozzle exit, contraction of liquid thread, breakup of liquid thread into primary drop and satellites, and recombination of primary drop and satellites, are analyzed based on the experimental results. The breakup time of liquid threads was found to be dependent mainly on the capillary time based on the length scale of the nozzle orifice and the growth rate of the most unstable disturbance normalized by the inverse of the capillary time. However, a well-designed waveform of driving signal can

initiate an abrupt pinch-off of liquid thread from the nozzle exit. During the contraction of the liquid thread after it has pinched off from the nozzle, two modes of breakup were observed: end-pinching where the liquid thread pinches off from an almost spherical head, and multiple breakup due to capillary waves. The effects of liquid and system parameters on the formation and recombination of the primary drop and satellites were investigated. Based on experimental observations, a necessary condition for the recombination of the primary drop and satellite and the limit for liquid thread length without breakup during contraction are proposed. The primary drop size increases slightly with increasing surface tension and decreasing viscosity. The driving voltage to the piezoelectric transducer mainly determines whether satellite formation will occur and size of satellites, while it has insignificant effect on primary drop size.

Second, using the visualization system coupled with a motorized stage, micron-drop impaction on substrate was investigated over a wide range of impact velocity (U_0) (2.21 – 12.2 m/s), contact angle (θ) (6 – 107º) and drop size (D_0) (40.8 – 50.6 μm). The corresponding ranges of Weber number (We) and Reynolds number (Re) are 2.77 - 103 and 100 - 689, respectively, the typical regime for inkjet printing applications. The experimental results for micron-drop impaction show that the initial spreading ratio, $D^* = D/D_0$ where D is the diameter of the contact area of the spreading drop, is dominated by We and Re, with θ having a negligible effect. As spreading continues, the effect of θ becomes pronounced, and maximum spreading ratio, D^*_{max}, increases with θ; however, for high-We impaction (103), the effect of θ on D^*_{max} is less significant than that for low-We impaction (2.77 and 12.8). Existing models for predicting D^*_{max} give good predictions with deviations less than 10% from present experimental results for high-We impaction (We=103), even though most of these models were built based on the millimeter-drop impaction experiments. For low-We impaction, the predictions of most of these models do not agree well with present experimental results, especially on the low-contact angle surfaces. However, the model of Park, et al. [61] is an exception: it

gives a good prediction (less than 10%) for high-We impaction as well as low-We impaction. The consideration of spontaneous spreading dissipation by this model indicates that the spontaneous spreading dissipation is not negligible, which is supported by our calculations. In addition, based on our results for micron drops, the dimensionless time to reach D^*_{max} is not a constant as used in several previous investigations, but ranges from 0.6 to 2.99, depending on We and contact angle.

Drop retraction from D^*_{max} depends on the We as well as θ: For hydrophilic surfaces, the retraction height decreases as We increases; but, on the contrary, for hydrophobic surfaces, the retraction height increases with We, and rebounding occurs when We exceeds a critical value. The rebounding model of Mao's et al. [54] correctly predicts rebounding in present experiments for most cases. On the very hydrophilic surfaces, after reaching a local maximum in D* curve which is followed by slight retraction, D* continues to increase. Spreading, driven by wettability, follows the form $D^* = gt^n$, where g and n are two constants related to We and θ, respectively. The final drop position, D^*_f, increases with both θ and We.

Fingering and splashing do not occur in present experiments on dry solid substrates as well as liquid film. In the drop impaction on the liquid film, the crown was formed, but did not break up into droplets. For dimensionless parameters typically of DOD inkjet printing, splashing criteria of Cossalli et al. [15] indicates that splashing will not occur for DOD inkjet printing. Micron drops evaporate very rapidly (< 1 second) on substrates in atmospheric air in the present experiments. Drying time increases as θ increases.

Under the same We and Re, the micron-drop impaction then was scaled up to millimeter scale by using drop (the mixture of glycerin and water) with a diameter of 2.23 mm and impact velocity of 0.27 to 1.69 m/s. Our results indicate that scaling of micron-drop impaction from millimeter-drop impaction, based on three dimensionless numbers

(Re, We and cosθ), is valid. Plots of D^* vs. tD_0/U_0 and H* vs tD_0/U_0, where t is time and H* is maximum height of spreading drop scaled by D_0, for micron and millimeter drops at the same dimensionless number are similar except that D* of millimeter drops is usually slightly larger during the whole process. The discrepancy is ascribed mainly to the effect of gravity. For the millimeter drop, the role of gravity in impaction is more significant than that for the micron drop.

CHAPTER 1

INTRODUCTION

Drop-on-demand (DOD) inkjet printing is an efficient approach for depositing micron-size drops on various targets. It is compatible with various liquids and does not require contacting the substrate. DOD inkjet technology has been successfully applied in many engineering and scientific applications, such as ink jet printing, DNA micronarrays, printing of organic transistors, printing of light-emitting diodes, ceramics and biopolymer arrays [12, 16, 79].

In these applications, the final state of the material left on the substrate after solvent evaporation is significantly affected by two important processes involved DOD inkjet printing: drop formation and impaction on the substrates. Because the key stages during drop formation and impaction normally last less than 100 μs for a typical micron-size drop formed in DOD inkjet printing, normal high-speed photography is not able to capture micron-scale motions in detail. For example, a camera having the speed of 10,000 frames per second can only obtained one or two images during 100-μs period. Therefore, the fundamental dynamics of DOD inkjet drop formation and impaction on substrates have not been studied in detail and thus are not thoroughly understood. On the other hand, millimeter-scale drop formations, such as continuous jetting and dripping, and millimeter-scale drop impaction on various substrates have received extensive attentions for over one century. Many theoretical analysis and experiments have been performed to investigate these processes [24, 33, 58, 60] and provides a rich background for understanding the corresponding micron-scale processes.

The goal of the present work is to understand at a fundamental level the dynamics of DOD drop formation and micron-drop impaction on solid surfaces. Based on the flash-photography technique [64], an experimental setup of high-speed imaging system

and micron-drop generator was developed, which enable visualize the micron-scale motions involved in inkjet deposition with the temporal resolution up to 200 ns and the spatial resolution up to 0.81 μm/pixel. Through image analysis, DOD drop formation dynamics of well-characterized simple liquids and their behaviors during the impaction and spreading processes were examined.

The remainder of this thesis is organized in five chapters. Chapter 2 presents the background and literature review about the drop formation and impaction with a focus on micron scale. Chapter 3 introduces the experimental setup and protocols. The next two chapters are devoted to the experimental results and discussion: Chapter 4, the dynamics of DOD drop formation; and Chapter 5, the dynamics of micron-size drop impaction. Finally, the conclusions of the present work are summarized and some recommendations for future investigations are given in Chapter 6.

CHAPTER 2

BACKGROUND AND LITERATURE REVIEW

Drop formation and impaction occurs daily, for example, droplets dripping from faucets and raindrops falling on puddles. They are important in many engineering and scientific applications, such as ink jet printing, DNA microarray systems, deposition of reagents on diagnostic strips, and spray cooling [6].

2.1 Drop Formation

2.1.1 Dripping, Continuous Jetting, and DOD Jetting

Three common modes of producing a single drop from an orifice are dripping, continuous jetting, and drop-on-demand (DOD) jetting (Figure 2-1). Dripping occurs under the action of gravitational force when liquid exits a capillary tube at a low flow rate. The drop production rate of dripping is low since it takes a relatively long time (from several seconds to several minutes) to generate one drop. Therefore, this mode is mainly employed in some test devices, such as surface tension meters and contact angle meters. When the flow rate through the capillary tube increases, the transition from dripping to continuous jetting occurs. The continuous jet breaks into drops due to the Rayleigh instability [65]. By introducing a cyclic disturbance, a stream of uniform drops can be generated, which has been successfully applied in inkjet printing. This mode can produce drops with the high speed and frequency, but with low efficiency and requires a complicated control system. A DOD drop generator ejects out a tiny amount of liquid by applying a short pressure wave to the liquid filling the channel. Under the appropriate conditions, the blob of fluid exiting the nozzle evolves into a single drop. It is an ideal method to deposit micron-size liquid on a substrate in many applications because it is

compatible with various materials and easily controlled by tuning the driving electrical signal [47].

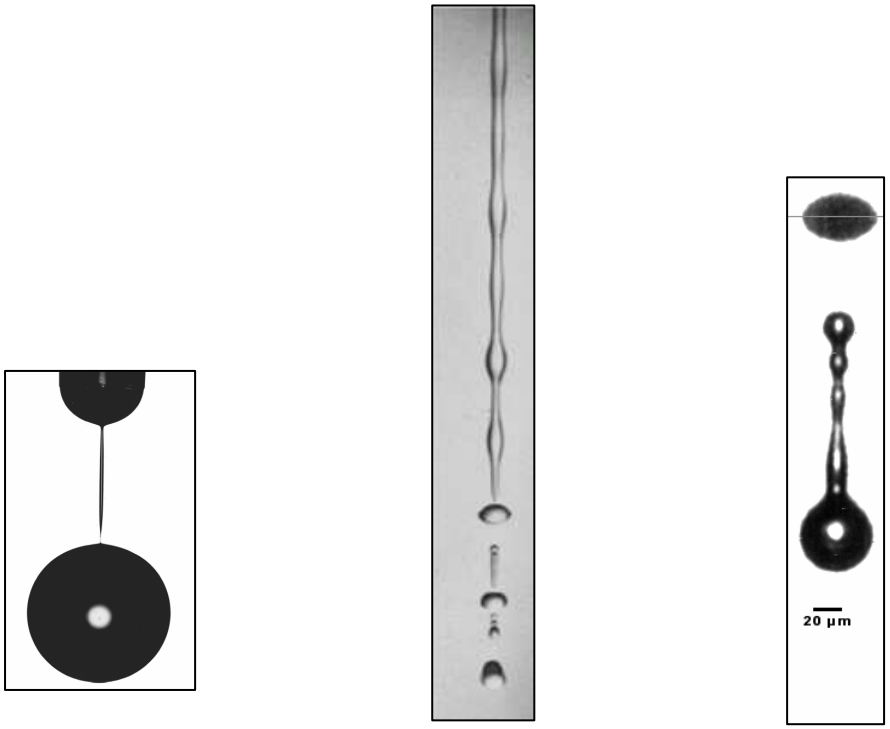

a) Dripping [76] (about 2 mm)

b) Continuous jetting [35]

c) Drop-on-demand jetting (present work)

Figure 2-1: Three modes of drop formation

The dripping and continuous jetting processes have been investigated for about one century. Excellent reviews of the literature in these topics can be found in Bogy [9], Eggers [24], Lin and Reitz [51] and Furbank and Morris [34] and Subramani et al. [82].

2.1.2 DOD Drop Formation

DOD inkjet printing, which was introduced in 1970s as a "man-made" method to generate drops, has not been well investigated even though it has been widely used in ink jet printing, DNA micronarrays, organic transistors, light-emitting diodes, ceramics and biopolymer arrays [18, 87]. The broad utility of DOD generators lies in their ability to

produce drops in the range from several to several hundred microns. However, this drop size and rapidity of formation – the entire process of its drop formation lasts only about a hundred micro-second – lead to difficulty in observing and recording with normal high-speed imaging.

Using stroboscopic or flash photography, Doring obtained a sequence of photographs of the DOD drop formation process by superimposing 100 separate images [22]. Although the sequential images did not give an accurate temporal evolution of the whole process, they exhibited several key stages of DOD drop formation. Shield et al. Rembe et al. [68] applied a similar principle referred to as pseudocinematography to record the drop ejection process from a thermal ink jet with an improved temporal resolution. The images were obtained with an exposure time of 250 ns and an interframe time of 1 μs. In related work [69], the DOD drop formation process was also captured by a ultrafast digital image system, which recorded continuously a sequence of eight images at frequency up to 100 million frames per second. Chen and Basaran [14] also used an ultrafast digital imaging system to record continually the DOD drop formation process. However, even though ultrafast digital systems [14, 69] were used, the maximum number of frames for one single process was too low for detailed analysis of the entire drop formation process. Based on the images by flash photography, the effects of ink properties on the liquid length ejected from the nozzle exit have been discussed.[25, 52]

Numerical simulations of DOD dynamics have been carried out, based on 1-dimensional model [1, 77] and 2-dimensional axisymmetric Navier-Stokes equations [27, 30]. The simulation results provide insight and understanding for DOD drop formation, and some gross comparison between the experimental results and simulation showed their agreement encouraging (reference). However, experimental observations with well-defined parameters for comparison with the simulations are lacking.

2.2 Drop Impaction

2.2.1 Drop Impaction on Various Substrates

Drop impaction on surfaces has received extensive attention over one century since Worthington observed and recorded the pattern left by water, milk, and mercury drops impact on smoked and unsmoked glass plates [88, 89].

Drop impaction may results in various outcomes depending on the circumstances of impaction [66, 91]. For most cases, drop spreads, retracts and oscillates to the equilibrium state. The details of these stages are presented by Ok [58]. The other possible outcomes of drop impact on surface are rebounding, bouncing and splashing [50, 56, 70, 71]. These outcomes of the collision are determined by the following factors: the properties of drop, kinetic parameters of the drop, properties of substrate, and the interactions of the liquid/substrate which characterized by static and/or dynamic contact angle. The significant drop parameters include viscosity, surface tension, impact speed, temperature [4], additives such as surfactant [55, 62] and polymer [17]. The parameters related to the substrate consist of roughness [63], variation of surface through chemistry [49], and substrate temperature [7, 13]. In addition, the geometry and state of the substrate are also important as shown by Hardalupas (spherical surface) [37], Rozhkov, et al. (sharp target) [72], Sikalo (inclined surface) [78], Fedorchenko et al. (liquid film or deep liquid) [26], and Lee et al.(moving substrate) [48].

Various theoretical methods have been developed to analyze and model drop impaction process [11, 31, 44]. Most of investigations on drop impaction focus on spreading process, occurrence of splash and bouncing because they play a significant role in various applications. Dimensional analysis [74] shows that the impaction process of Newtonian fluid is mainly governed by three independent dimensionless numbers, Reynolds number, Re, Weber number, We, or Capillary number, Ca, and contact angle, θ:

$$We = \frac{\rho U_0{}^2 D_0}{\gamma};\ Oh = \frac{\mu}{\sqrt{\rho\gamma D_0}} \text{ or } \mathrm{Re} = \sqrt{We}/\mathrm{Oh} = \frac{\rho \mathrm{U}_0 D_0}{\mu};$$

$$\cos\theta = \frac{\gamma_{SV} - \gamma_{SL}}{\gamma}$$

Where U_0 is the velocity of drops, D_0 is the drop diameter, μ is the liquid viscosity, γ is the surface tension or surface energy per unit area of liquid, ρ is the liquid density, γ_{SV} is the interfacial energy between substrate and air, and γ_{SL} is the interfacial energy between substrate and liquid. Note that drop radius instead of drop diameter is used as the characteristic length in Re and We by some investigators such as Schiaffino & Sonin.

Schiaffino & Sonin [74] states that the Weber number indicates the driving forces of the spreading process: At high We, the drop liquid is pushed radically outward by the impact-induced dynamics pressure gradient; at low We, it is pulled out by the capillary force. The Ohnesorge number scales the force that resists the spreading: At high Oh, the resistance is viscosity; at low Oh, it is inertia. The (We, Oh) plane contains four regions in which spreading velocity and time have different scales and driving force and resistance during spreading are different.

Based on the energy balance, several models [54, 61, 62] were built to predict the maximum spreading ratio, $D^* = D_s/D_0$, where D_s is the diameter of the contact area of drop on substrate and D_0 is the diameter of the impacting drop. These models showed satisfactory predictions for millimeter-drop impaction.

2.2.2 Micron-Drop Impaction

Most of the previous experiments about drop impaction on surfaces were conducted in the millimeter-scale regime. In inkjet printing, however, drops are generated over the range from several microns to several hundred microns. Therefore, the micron-scale impact is worthwhile to investigate because effects of dimensionless

parameters, such as roughness and capillary number, are difficult to scale up. Asia et al. [3] investigated spreading of micron-size drops from a piezoelectric inkjet printhead impacting on moving papers and built a model to predict the maximum spreading ratio, D^*.

$$D^* = 1 + 0.48We^{0.5} \exp[-1.48We^{0.22} \mathrm{Re}^{-0.21}]$$

Attinger et al. [4] investigated molten solder drops (with diameter of 50-100 um) impacting on substrates with the temperature ranging from 48 to 135°C. The transient process of impaction, wetting and solidification on substrates were recorded using a flash-photography imaging system with the temporal resolution of 5 μs. The maximum spread ratios on a high temperature substrate showed good agreement with the model predictions of Pasandideh-Fard et al. [62] without considering solidification. Using a double-flash technique, Kim et al. [45] constructed sequential images of the impaction of drops with diameter of about 200 to 300 um on a polycarbonate surface. The imaging system had a temporal resolution of less than 5 μs. Three experimental maximum spreading ratios were in a adequate agreement with predictions from the model of Mao et al. [54]. However, two of their experimental results showed that maximum spread ratio increased with We, but the model predicted two almost identical values. Thus, they concluded that We played a more important role in the micron-size regime than for the larger drops.

Dam et al. [86] studied the impaction of inkjet droplets with diameter ranging from 36 to 84 um and a velocity ranging from 0.74 to 13.8m/s on hydrophilic surfaces (with contact angle of 15°, 35°, and 75°). The sequential images of impact process were obtained by flash-photography technique with the spatial resolution of about 1.3 μm/pixel and the variation of 4 μm in droplet position along the flight direction. Their experimental results demonstrated that the early stage of drop spreading on substrates could be described well by the model of Kim et al. [44]. However, the maximum

spreading ratios were overestimated by the existing prediction models [62]. Dam et al. stated that the difference between model and experimental values are because viscous dissipation during spreading is estimated improperly in the model. Detail information on the whole micron-drop impaction process and direct comparison with that of millimeter-drops are still lacking.

2.3 Objectives of Present Work

Further understanding of the dynamics of DOD drop formation and micro-drop impaction on surfaces is important in the control of inkjet deposition. Present work is divided into two parts: the dynamics of DOD micron-drop formation and the dynamics of micron-drop impaction on surfaces. The objective of the first part is to apply flash photography to visualize the DOD drop formation process and based on the experimental results to develop a fundamental understanding of the dynamics of DOD drop formation. The objective of the second part is to determine the effects of drop size on the impaction process and to determine if the impaction process is scalable from millimeter drops to micron drops.

2.3.1 DOD Micron-Drop Formation

The literature has focused on the gross features during DOD drop formation. A thorough study on the entire process from the ejection to the formation of a single drop is needed. Due to the poor reproducibility caused by the first-drops problem of the DOD inkjet printing, previous experimental studies on DOD drop generation have done little to elucidate quantitatively the fundamental fluid mechanics of DOD drop formation. Many processes including the time evolution of liquid thread shape and velocity, breakup of liquid thread, satellite formation, and combination of satellites and primary drop have not yet been investigated for DOD drop formation. The liquid thread snapping off from the nozzle and contracting to form a single drop is a complicated hydrodynamical process. A

free liquid thread can break up into a primary drop and several satellites. Satellites are undesirable because they are detrimental to precision of drop deposition; therefore, the suppression of satellites is a topic of engineering importance for drop deposition methods including DOD.

The objective of this part is to apply flash photography to visualize the DOD drop formation process. A fundamental understanding of the dynamics of DOD drop formation is developed based on experimental results. Key stages are identified and defined. The effects of the driving signal producing the pressure wave by means of a piezoelectric transducer and of the liquid properties on DOD drop formation are analyzed.

2.3.2 Micron-Drop Impaction

The present imaging system coupled with the motorized stages allows visualization of the micron-drop impaction process with a temporal resolution up to 200 ns and spatial resolution of 0.81 μs/pixel. The whole system provides a better resolution and reproducibility than those in previous studies [14, 22, 68, 69]. In addition, in present study, surfaces with a wide range of contact angles (both hydrophilic and hydrophobic) are used. The drop diameter and impaction speed are also selected in an appropriate range according to the normal applications of DOD inkjet printing. Thus, corresponding dimensionless parameters lie in $O(10) < Re < O(10^3)$ and $O(1) < We < O(10^2)$, which are in the regime typical for inkjet printing [32]. The variation of diameter of contact area and height of drop on substrate with time were measured to express the whole impaction process. Other potential behaviors that have been observed for millimeter drops impacting surfaces, such as splashing and bouncing did not occur; however, rebounding was observed. The distinct behaviors of micro-drop impaction were identified. The experimental results, such as maximum spreading ratio and time to reach the maximum spreading, oscillation of drop on surfaces, were compared with predictions of several

existing models and/or conclusions obtained under millimeter scale to examine their applicability for micron-drop impaction. Finally, the micron-drop impaction was scaled up to millimeter size to examine the validity of existing scaling dimensionless parameters.

CHAPTER 3

EXPERIMENTAL

In this chapter, the experimental setup based on the flash technology is described first, and some key parameters of the imaging system are discussed. And the approaches to minimize the "first drops problem" in DOD inkjet printing and improve the reproducebility of process are discussed. Finally, the experimental protocols for DOD drop formation and impaction are described.

3.1 Experimental Setup

3.1.1 Apparatus

The method used for visualizing on the DOD drop formation and drop impaction is based on flash photography [64] (see Figure 3-1) and utilizes the setup shown schematically in Figure 3-2. The camera, printhead, and collimator are fastened on an optical base and optical tabletop (Melles Griot) to minimize vibration. The key technical requirements are synchronization of the laser flash with the image capture to a charge-coupled-device (CCD) camera and the ability to delay these processes relative to the liquid ejection at micron resolution. Using the pulsed laser, CCD camera, an inkjet printhead, signal generators and other control devices, sharp images at 200 ns temporal resolution were obtained. The technique used is to adjust delay times for the camera and laser relative to drop generation by piezoelectric transducer actuation in the printhead, while shutter operation of camera and laser flash are synchronized in order to obtain one image during each drop formation. By increasing the delay times of the camera and laser relative to the piezo transducer actuation in steps up to 200 ns, images progressively farther in time from the initiation event (the actuation) are captured. These images are combined to obtain a sequence of images of drop formation.

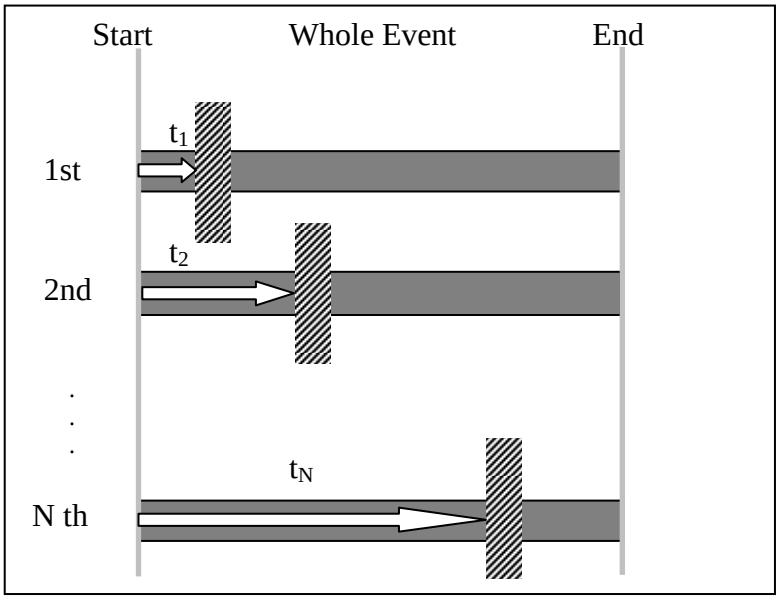

Figure 3-1: Flash photographic technique. The shutter opens after a delay time t_i (from the beginning of the event), and the whole event is repeated N times; thus, N images are obtained, representing the status of the event at time, t_i.

To achieve synchronization, a triggering signal is sent to a waveform generator (Tegam 2414B), the waveform generator then sends a driving pulse to the amplifier (Trek Model PZD 350) and a TTL signal, which is in sync with the driving pulse, to a delay generator (BNC 500). After amplification, the driving pulse is applied to the piezo transducer in the printhead (Trident) to eject liquid. The amplitude and shape of the driving pulse can be programmed according to the requirements of printhead and liquids. Upon receiving the TTL trigger signal, the delay generator sends out two signals: a 5-volt TTL signal to the CCD camera (SensiCam), and a burst of TTL signals with a preprogrammed number of cycles to the pulsed Cu vapor laser (Oxford Lasers, Cu 10). For drop impaction test, the delay generator sends out a third signal: a TTL signal is sent to the motorized translation stage (OptoSigma). The delay time and width of TTL signals

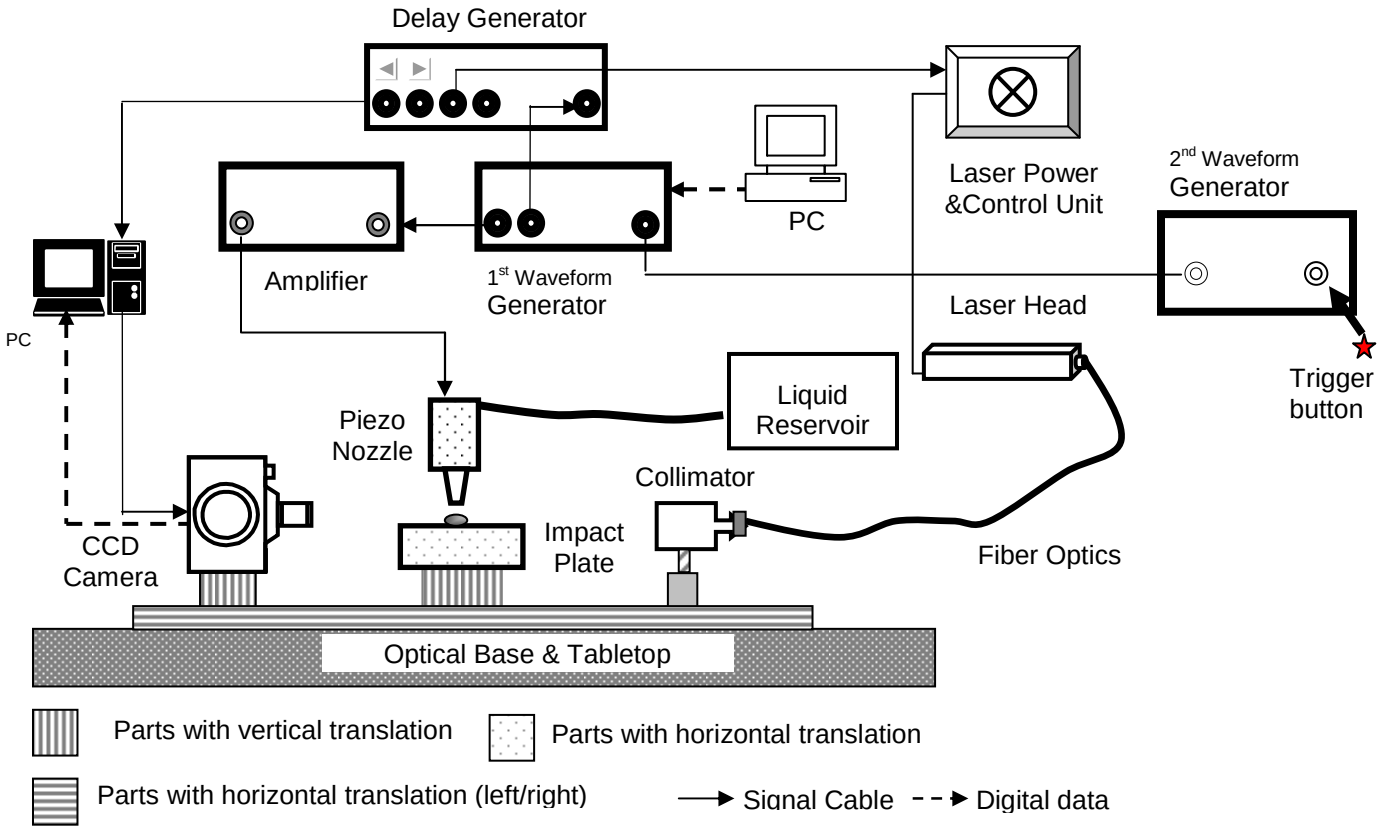

Figure 3-2: Experimental setup

are parameters that are set before the experiment begins. By adjusting delay times for the camera and laser, the drop generation by the printhead, shutter operation of the camera and laser flash are synchronized. Hence, one image can be obtained. Through changing the delay times of the camera and laser, images with different delay time from drop ejection are captured. These images are combined to obtain a sequence of images of drop formation and/or impaction.

For drop impaction experiments, through a signal switch, the motorized stage is triggered by the third TTL signal from the signal delay generator (note that the other two are sent to waveform generator and laser). The stage speed, waiting time and step length are programmed according to liquid and substrate requirements. Between impactions, the stage moves quickly and then stops. This allows each drop to impact fresh, stationary surface.

There are 640×480 pixels on the CCD sensor used in this study with the dimension of 6.3 mm by 4.8 mm. Using a group of microscope objectives with a working distance of about 25.4 mm, the spatial resolution of image is up to 0.81 μm/pixel with this system; the resolution could, in principle, be increased by use of a higher-resolution CCD (operating at low frame rate). However, for the visible light with the wavelength of about 550 nm as used in present experiments, the resolution of a compound microscope lenses is about 250 nanometers according to the Rayleigh criterion[80]. The camera system can be triggered via an external, edge active TTL signal. The CCD camera has a maximum frame rate of 30 frames per second and a storage capability of 727 images. The image data are read from the camera and transferred via PCI-Bus to the PC memory once the storage memory is full.

As shown schematically in Figure 3-3, the Trident Printhead is based on a push-mode design (Trident User's Manual, 1997). When voltage is applied to the transducer,

the transducer contracts, enlarging the ink chamber and causing ink to fill it. When the voltage is rapidly released from the transducer, the transducer resumes its original length,

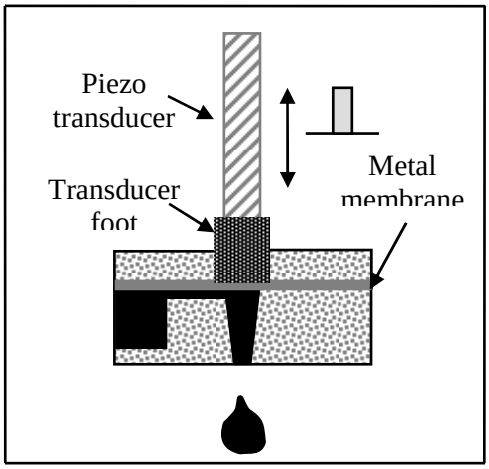

Figure 3-3: A push-mode piezoelectric drop-on-demand generator

which creates a sudden pressure pulse on the liquid in the ink chamber. A sufficient and well-shaped pressure pulse causes liquid to be ejected from the nozzle (D = 53 μm and L = 75 μm) at the end of the chamber, and a drop is generated.

3.1.2 Properties of the Imaging System

In order to obtain a sharp image on the micron-scale field of view, a light pulse with sufficiently short duration and high intensity is required. In order to saturate the CCD sensor, the pulse intensity should reach a critical value. In our imaging system, the CCD sensor has a full well capacity of about 35000 e^- and a quantum efficiency of 32% at a wavelength of 540 nm; so, the intensity of a 25-ns pulse reaching the CCD should be approximately 250 W/cm^2 (see appendix A). For a micron-scale object with a speed of 10 m/s, the maximum permissible exposure time to capture this motion is about 150 ns[64]. In present experiments, a pulsed Cu-vapor laser (Oxford Lasers), which emits green-yellow (510/578 nm) flash pulses with pulse duration of about 25 ns and energy of

2mJ, is used. In response to the external burst of TTL signals, the laser begins lasing in phase with the burst of TTL signals. The duration of each pulse is short enough not to heat the objects. Using a fiber-optic coupler, the laser output is delivered to a collimator through a fiber optic cable. The collimator provides a uniform and intense backlighting field.

The time resolution and accuracy of the imaging system depend on the exposure time and delay time settings of the camera, delay time settings of the delay generator and response time of the pulsed laser to the external signal. The resolution of the delay generator is 200 ns, and the camera has a resolution of 100 ns. When the two devices are combined, the time resolution of the imaging system is 100 ns. For times over which drop formation occurs (~ 1000 μs), the temporal accuracy of the delay generator is < 30 ns. The temporal accuracy of the camera shutter is < 40 ns. Thus the temporal accuracy of the imaging system is < 70 ns. After the camera and laser were synchronized, the delayed time of camera and laser was increase or decreased by the same amount. White images were obtained for each of the experiments. Shifting the delayed time of the camera in increments of 100 ns (minimum step for the camera) resulted in black images, revealing that the camera and laser were no longer synchronized. This test was repeated over 100 times with the same result. Therefore, the response time of the laser to the external signal is quite stable, and the laser pulse can be synchronized with the camera shutter.

The camera, printhead and collimator are positioned on X-Y-Z translation stages (Melles Griot), which can be moved with resolution of 3 μm in each direction. The impact substrates are placed on a motorized translation stage (OptoSigma), which has vertical and horizontal deviations of less than 2 μm over the 50 mm travel range. All the devices are fastened on an optical base and optical tabletop (Melles Griot) to minimize the impact of the system vibration. In the present experiments, vibration does not have significant influence under these precautions.

The uncertainty of the experimental results of drop formation impaction results from determination of exact impaction instant as well as the reproducibility of drop formation and variation of surface wettability. The accurate impact instant (t = 0) is often interpolated from two consecutive images, which causes some uncertainty less than the interframe time of images. At the early stage of impaction (t <2 μs), the uncertainty is significant, especially for low-speed impaction. For example, 1-μm positional deviation for a drop with a speed of 2 m/s leads to a time deviation on impaction of 0.5 μs, which causes a wide distribution in measured spread diameter and height of impaction drop on substrate in the initial spreading. The distribution decreases dramatically as spreading time increases and the uncertainty in time relative to spreading time is reduced.

3.1.3 Reproducibility of Tested Processes

The reproducibility of the process under study is the major concern for flash photography, because it is assumed that taking images at different times in individual tests in a series of tests will allow reconstruction of the dynamics representing the process (single drop formation and impaction). Several factors which can make the size and formation dynamics of the first few drops inconsistent are fluctuation of signal amplitude, accuracy of time setting, surrounding air current, wetting of nozzle plate, and the "first drop problem" of inkjet printing [42]. Although all of the factors may affect reproducibility, the last one is the most significant in the present experiments. The "first drop problem" is caused by the evaporation of ink at the nozzle exit. The evaporation of ink depends on the idle time of the nozzle. In order to minimize the "first drop problem", a pulse train from an external waveform generator (Agilent 33220A), instead of a single pulse, is applied to trigger the whole system in present experiments. Hence, for each trigger, not a single drop, but a drop stream is generated, and the idle time between two drops is constant. After several drops, the drop formation becomes consistent with a position variation less 1 μm (see Figure 3-4). The number and frequency of drops

generated per trigger are changed through programming the length and frequency of the pulse train in the external waveform generator. Depending on the liquid components, the length of the pulse train per trigger is increased until the required number of consistent drops is generated. The frequency of the pulse train is adjusted to match the camera's continuous working speed.

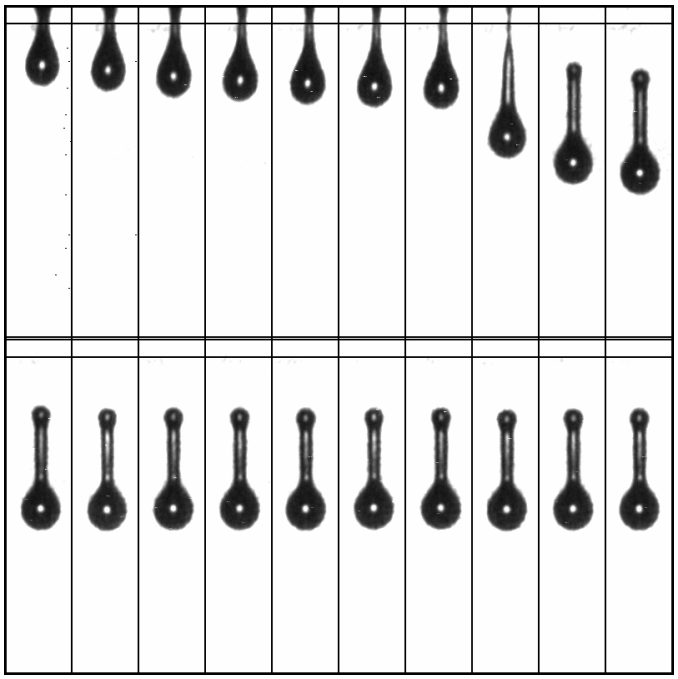

Figure 3-4: Reproducibility of drop generation of Mixture GW using the double-peak waveform shown in Figure 3-5 with voltage amplitude = 21.6 V and frequency = 20 Hz. After about ten drops, drop ejection becomes identical.

The reproducibility of the drop impaction process depends on the reproducibility of the drop formation process. After several drops are formed, drop formation becomes consistent with a positional variation < 1 μm over the region of drop formation which about 200 μm. As the drop moves further from the nozzle, the positional variation increases. For the distance between the nozzle exit and the substrate used in present experiments (about 2 mm), the variation of drop position was about 2 μm. The effect on

time uncertainty decreases as the speed of the drop increases; uncertainty in time is 1 and 0.2 μs for drop speeds of 2 and 10 m/sec, respectively. Other factors affecting reproducibility of the drop impaction process are the flatness of the substrate and substrate wettability. Since the substrate is moved to provide fresh surface, the substrate position varies. For an experiment involving 20 drops, the variation in drop-impaction position of the substrate is 0.5 micron, which introduces an uncertainty in the time of impaction of 250 and 50 ns for drop speed of 2 and 10 m/s, respectively. The reproducibility of impaction process also becomes worse because the wettability of substrates varies slightly with impaction position. In our experiments, the impactions of the last ten drops in a sequence of 20 drops were studied. The contact diameter of the spreading drop was measured, and the coefficient of variation was less than 3% for time > 10 μs after impaction.

3.1.4 Waveform of Driving Signals

The two types of signal waveforms that are suggested by the manufacturer for driving a Trident piezo transducer are shown in Figure 3-5. One is a double-peak waveform (Figure 3-5 (a)), and the second is a single-peak waveform (Figure 3-5 (b)).

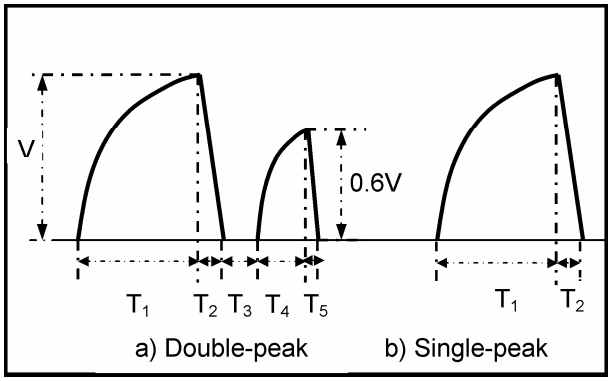

Figure 3-5: Two signal waveforms used in present experiments. The single-peak waveform is obtained by removing the minor peak from the double-peak waveform.

First, consider how the push-mode piezoelectric drop-on-demand generator responds to the double-peak waveform signal. During the rising time (T_1), the piezo transducer contracts so that the liquid fills the nozzle chamber. A slow rising time is used to prevent air from being sucked into the channel through the nozzle orifice. During the falling time (T_2), the reduction of voltage makes the transducer extend to its original length, thus a pressure is created on the liquid in chamber and liquid is ejected from the nozzle orifice. After the voltage falls to zero, it is held there for a short time (T_3). Then a smaller pulse is applied to the transducer. The shape is similar to the initial pulse, but the voltage maximum amplitude is smaller, and the corresponding rising time (T_4) is shorter. After the voltage reaches its maximum, it falls over a falling time (T_5) in a fashion similar to that of the initial pulse. The smaller pulse is used to promote separation of liquid from the nozzle orifice by producing a negative pressure (suction) in the nozzle during the small pulse rise time. The falling pressure decelerates the liquid causing it to break from the nozzle orifice. The single-peak waveform (signal b) is identical with the large peak of the double-peak signal (signal a); the smaller pulse is left off.

Table 3-1: Parameters of four driving signals.

Signal	Voltage (volts)	Rising time T_1 (μs)	Falling time T_2 (μs)	Dead time T_3 (μs)	Rising time T_4 of small pulse (μs)	Falling time T_5 of small pulse (μs)
1	21.6	10.6	2.6	5.3	4.4	3.0
2[a]	21.6	10.6	2.6	…..	…..	…..
3	21.6	14.4	2.6	5.3	4.4	3.0
4	21.6	10.6	5.0	2.4	4.4	3.0

[a] Single-peak waveform

In order to investigate the effect of the parameters of signal waveform on DOD drop formation, four kinds of signal waveforms were used in present experiments. Their parameters are listed in Table 3-1. Signal 3 has a longer T_1 of 14.4 μs and is otherwise similar to the signal 1. Signal 4 has a longer T_2 and similar other parameters to the signal 1. The single-peak waveform (signal 2) is identical with the large peak of the double-peak signal (signal 1); the smaller pulse is left off. For most of experiments, signal 1 is applied, and the other three signals are used in demonstrating the effects of signal waveforms on DOD drop formation process.

3.2 Experimental Materials and Protocols

3.2.1 Parameters for Drop Formation

Distilled water, a mixture labeled GW (glycerin and water, 48/52 on a mass basis), and a mixture labeled GWI (glycerin, water, and isopropanol, 34/53/13 on a mass basis) were used in the present experiments (Table 3-2). By adding glycerin to water to produce GW, viscosity was increased from 1.0 cP (water) to 5.0 cP, while decreasing surface tension only slightly (73 to 68 mN/m). Temperature was maintained near 20ºC. The addition of isopropanol as a minor component to form GWI allowed decreasing surface tension to 35 mN/m without greatly affecting viscosity. Viscosity and surface tension were measured using a viscometer (Brookfield DV-I+) and a bubble pressure tensiometer (Kruss BP2), respectively. The values of viscosity and surface tension of liquids were selected to fall into the normal ranges for commercial ink and to be compatible with the Trident printhead.

In order to avoid the “first drop problem” that was discussed in Section 2.1, we used a 20-signal train to generate 20 drops for every trigger. A drop formation frequency of 20 Hz was used in all the experiments, which allows the CCD camera to capture every

drop. The first ten drops often have poor reproducibility and are excluded from data analysis. Drop formation of the last ten drops is very similar with a positional variation of less than 1 μm (Figure 3-4).

Table 3-2: Properties of liquids in experiments on DOD drop formation at 20°C

Liquids (weight fraction)	Density (g/cm^3)	Viscosity (mPa·s)	Surface tension (mN/m)	Time scale (μs), t_{v*}	Length scale (μm), l_{v*}
Water	1.00	1.0	73	0.000193	0.0139
GW (Glycerin/water, 48/52)	1.12	5.0	68	0.0256	0.3
GWI (Glycerin/water/isopropanol 34/53/13)	1.05	5.0	35	0.103	0.708

*length scale $l_v = \frac{\rho\nu^2}{\gamma}$ and time scale $t_v = \frac{\rho^2\nu^3}{\gamma^2}$, where ρ, ν and γ denote the density, kinematic viscosity and surface tension respectively. The significance of length and time scale shown here will be mentioned in Chapter 4.

Cleaning the printhead was accomplished using test liquid. The liquid flowing out from nozzles was collected, and its surface tension and viscosity were measured. The process was repeated until there is no measurable difference in viscosity and surface tension from those of the sample liquid.

Each experiment was repeated three times to ensure that consistent results were obtained.

3.2.2 Parameters and Substrates for Micron-Drop Impaction

Experiments of micron-size drop impaction (see Table 3-3) were conducted using distilled water drops with three different speeds and sizes. The different velocities and diameters were obtained by varying the signal amplitude sent to the piezoelectric transducer. The corresponding ranges of Reynolds number, Re, and Weber number, We,

of drops are 1-100 and 10-1000, respectively, which cover a typical regime for inkjet printing [32]. Due to the slow response of the motorized stage to external triggering signal and the requirements of reproducibility, for each delaying time setting, the frequency of drop formation was reduced from 20 Hz used in the drop formation experiments to 2 Hz. A 20-signal train with a frequency of 2 Hz was applied to trigger the imaging system and motorized stage.

Five substrates including glass slide (Fisher), thermal oxide silicon wafer, and three kinds of self-assembled monolayers (SAMs) on gold coated silicon wafers were used as the impact substrates. The contact angles of water on these surfaces are listed in Table 3-4. Polished silicon wafers were used as substrates to ensure the minimum effect of roughness on the impaction process. Silicon wafers were treated to produce the film of thermal oxide on the silicon wafer, which makes the surface more stable. Oxidation of the surface of the silicon wafer was performed for four hours in a thermal oxidation furnace containing dry O_2 at a temperature of about 1000 °C.

Table 3-3: Experimental parameters for micron-drop impaction

Impact velocity (m/s)	Drop size (um)	Re	We	Oh
2.21	40.9	100.9	2.77	0.0165
4.36	48.8	238	12.8	0.0151
12.2	50.5	689	103	0.0148
Inkjet printing		$O(10)$-$O(10^2)$	$O(1)$-$O(10)$	
Spray cooling		$O(10^2)$-$O(10^3)$	$O(10)$-$O(10^2)$	
Spray coating		$O(10^3)$-$O(10^4)$	$O(10^2)$-$O(10^3)$	

The monolayers were prepared by immersing freshly evaporated gold-coated (about 1000 Å thin) silicon wafer into 1mM solution of thios in ethanol for 12 hours [5]. Before the thermal evaporation of gold, the silicon wafer was precoated with chromium (about 50 A) to improve the adhesion. The samples were washed with ethanol and blown dry with a stream of N_2. The two thiols, 11-Mercapto-1-undecanol [$HS(CH_2)_{11}OH$] and 1-Octadecanethiol [$CH_3(CH_2)_{17}SH$], were used to vary the amounts of hydrophilic (-OH) and hydrophobic (-CH_3) groups in the monolayer [49]. The contact angle of water on the monolayers varied with the content of the two thiols in solution, as shown in Table 3-4.

Table 3-4: Equilibrium contact angles of water on surfaces

Impact substrates	Contact angle of water (^{o})	Contact angle of glycerin/water mixtures (^{o})
Glass slide,	~6	--
Thermally oxidized silicon wafer	31±2	24±2
9:1 OH/CH_3 SAM on gold coated silicon wafer	67±2	62±2
7:1 OH/CH_3 SAM on gold coated silicon wafer	88±2	--
100% CH_3 SAM on gold coated silicon wafer	107±2	99±2

Surfaces with low contact angles, such as thermally oxidized silicon wafer and glass slide, are easily contaminated due to the adsorption of gas and dust. Thus, their contact angles increase gradually with storage time, for example, in one case contact angle for thermal oxide coated silicon wafer was observed to increase to 70^o. The following procedures were conducted to clean the surfaces with low contact angle: soak the surface in the NanoStrip (Cyantek Corp.) at 60 ºC for 30 minutes; rinse the surface extensively with distilled water; and blow dry the surface with N_2. The fresh-cleaned

surface had constant contact angle for several hours (approximately 4 hours); so the impact test were conducted during this period. After that, the surface was re-cleaned.

Other surfaces (with a contact angle larger than 60°) could be re-used if they were cleaned with ethanol and blown dry with N_2 just before use; however, the contact angle was measured before every test to ensure that the surface had not changed.

3.2.3 Scaling up of Micron-drop Impaction Into Millimeter Size

In order to identify the distinct characteristics of micron-drop impaction, millimeter- and micron- scaled impaction tests were conducted at the same values of Oh (or Re) and We. The matching millimeter tests were conducted using the drop with a diameter 2.23 mm, and liquid properties and drop speed were adjusted to obtain the required Re and We. Mixtures of glycerin and water were selected as the working liquids. The experimental parameters for the millimeter-drop impaction tests are listed in Table 3-5.

Table 3-5: Experimental parameters for millimeter-drop impaction*

Liquids (weight fraction)	Viscosity (cP)	Impact velocity (m/s)	Drop size (mm)	Re	We	Oh
Mixture 1 (Glycerin/water 53/47)	6.7	0.27	2.23	101.6	2.74	0.0163
Mixture 2 (Glycerin/water 50/50)	6.1	0.58	2.23	241	12.7	0.0148
Mixture 3 (Glycerin/water 49.5/50.5)	6.0	1.67	2.23	700	105	0.0146

*For three mixtures, density = 1.13 g/cm^3, surface tension = 67 mN/m. [85]

The millimeter drops were generated through the dripping mode using the modified experimental setup of Ok [58]. The liquid was pushed out of a syringe with a 28-gauge needle at a flow rate of 0.02 ml/min, producing a drop with a diameter of about

2.23 mm. Drop impact speed was changed by varying the distance of the nozzle tip from the impacted substrate. A CCD camera (Photron, 1280×1024 pixels) was used to record the whole impaction process at the speed of 4000 fpm and exposure time of 1/32,000 s. The spatial resolution of imaging system is 26.6 μm/pixel.

3.3 Imaging Process and Data Analysis

The present experimental results are based on pictures captured by the high-speed imaging system. More than 500,000 TIFF images were obtained in the study. About 100,000 images among them were selected and analyzed. Since a qualitative description from these images is not enough to understand the process accurately, detail analysis of the images was performed. Several representative points in the liquid were selected, and variations of their positions with time were measured to form a series of curves that were used to describe quantitatively the dynamics of drop formation and impaction. For the drop formation tests, the positions of several representative points in the ejected liquid were selected (as seen in Figure 3-6). Their axial distances from the nozzle exit are denoted $x_1(t) - x_5(t)$, respectively, with t being time measured from the first appearance of liquid from the nozzle. The interpretation of these points and generated curves will be discussed in details in Section 4-1. For drop impaction, the diameter of contact area and height of drop above substrate after impaction (see Figure 3-7) were measured to obtain the impaction curves as many have done [58, 60].

The representative points in the liquid were determined by manually counting pixels using MS Paint. We attempted to use Matlab code to process these images; however, the results were not satisfactory due to the uneven image background caused by variation in the laser pulse intensity, both within and between frames. Most of images shown here were obtained after cropping using Matlab image toolbox. In order to convert pixel values to positional values in X-Y coordinates, the image system was calibrated. After the imaging system with microscopic lenses was focused, a standard micron ruler (Nikon Stage Micrometer, 1 mm) was used to determine distance per pixel in the focused plane. The micon-scale and millimeter-scale tests use different microscopic lenses with spatial resolution of 0.81 and 26.6 μm/pixel, respectively.

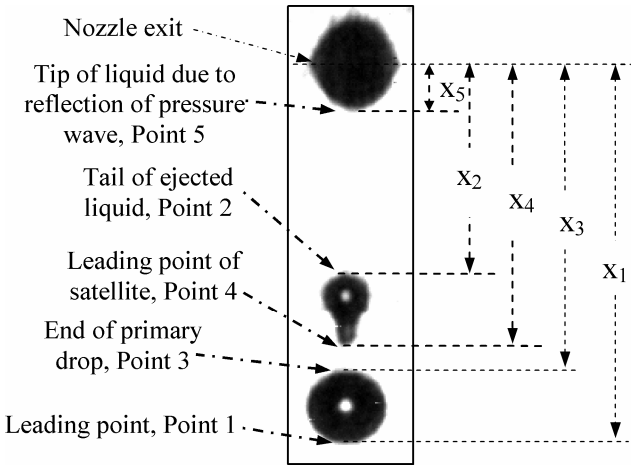

Figure 3-6: Several representative points during the evolution of the ejected liquid

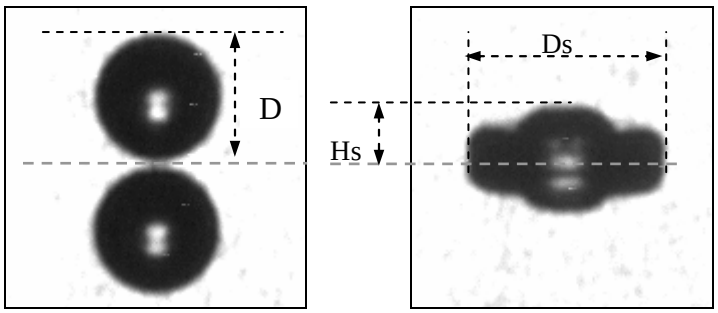

a) Before impact b) After impact

Figure 3-7: Parameters for drop impaction on substrate

CHAPTER 4

DOD DROP FORMATION

The experimental results and discussions on DOD drop formation are presented in this chapter. A general description of DOD drop formation is given first. Then important stages during DOD drop formation, which include ejection and stretching of liquid, breakup(s) of liquid thread, contraction of liquid thread, and formation and combination of primary drop and satellites, are discussed, respectively. Finally, the effect of waveform of driving signal on DOD drop formation is demonstrated.

4.1 General Description of DOD Drop Formation

A sequence of images during DOD drop formation is shown in Figure 4-1, revealing the main features of this process. A general description of DOD drop formation is presented using results from these images. The graphical method we have developed for representing the DOD process is described first.

4.1.1 Graphical Representation of DOD Drop Formation

In order to discuss quantitatively DOD drop formation process, the positions of several representative points (see Figure 3-7) in the ejected liquid are plotted versus time to produce the curves of DOD drop formation (see Figure 4-2). The axial distances of Points (1) – (5) from the nozzle exit are denoted $x_1(t)$ – $x_5(t)$, respectively, with t measured from the first appearance of liquid from the nozzle. Initially, Point (1) is the leading edge of the liquid ejected from nozzle and later becomes the tip of the primary drop. Point (2) is the first pinch-off point of liquid from the nozzle exit, and also the tail of the free liquid thread; its first appearance corresponds to the initial breakup time t_{b1}.

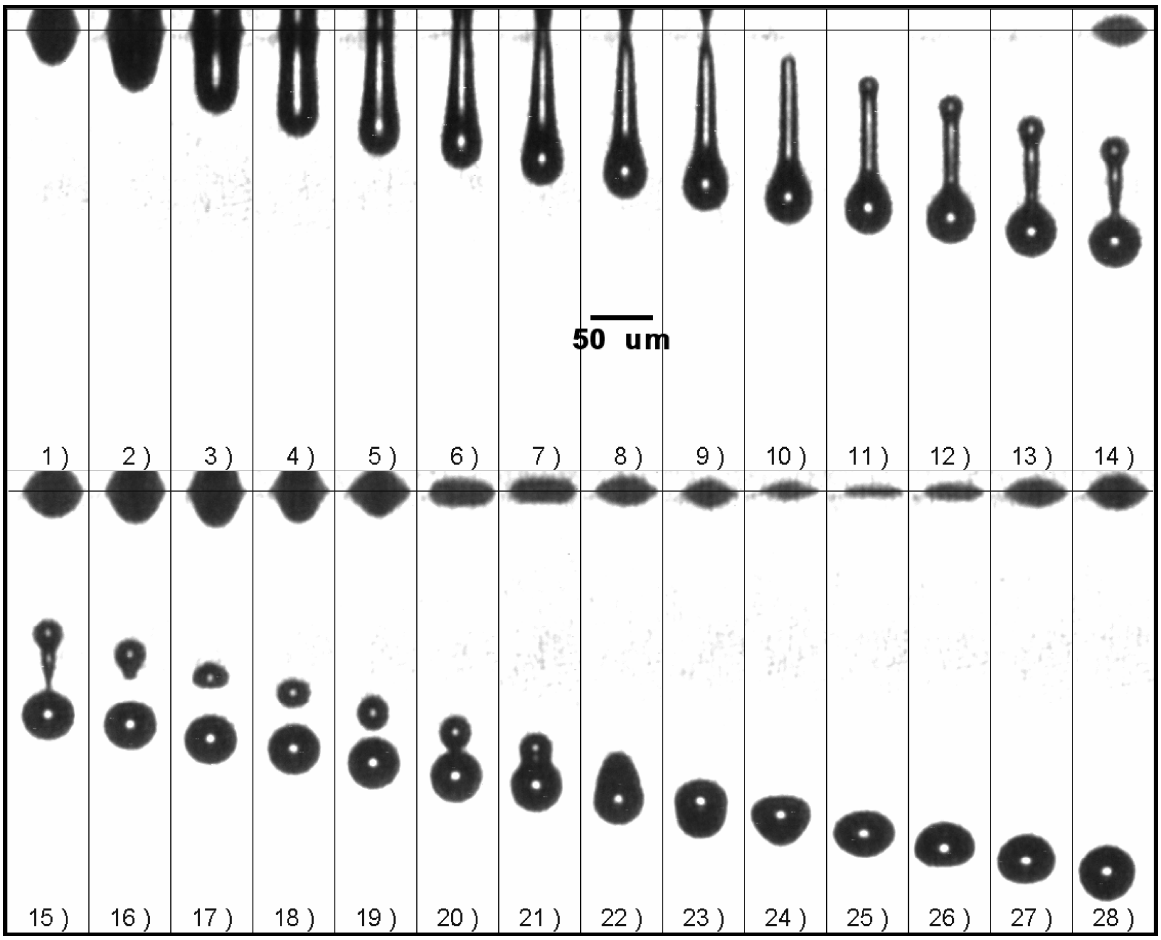

Figure 4-1: Sequence of images of DOD drop formation for GW using the double-peak waveform in Figure 3-5 with voltage amplitude = 21.6 V and frequency = 20 Hz. Interframe time = 3 μs and image size = 65 μm × 373 μm. GW is a mixture of glycerin/water with viscosity = 5.0 cP and surface tension = 68 mN/m

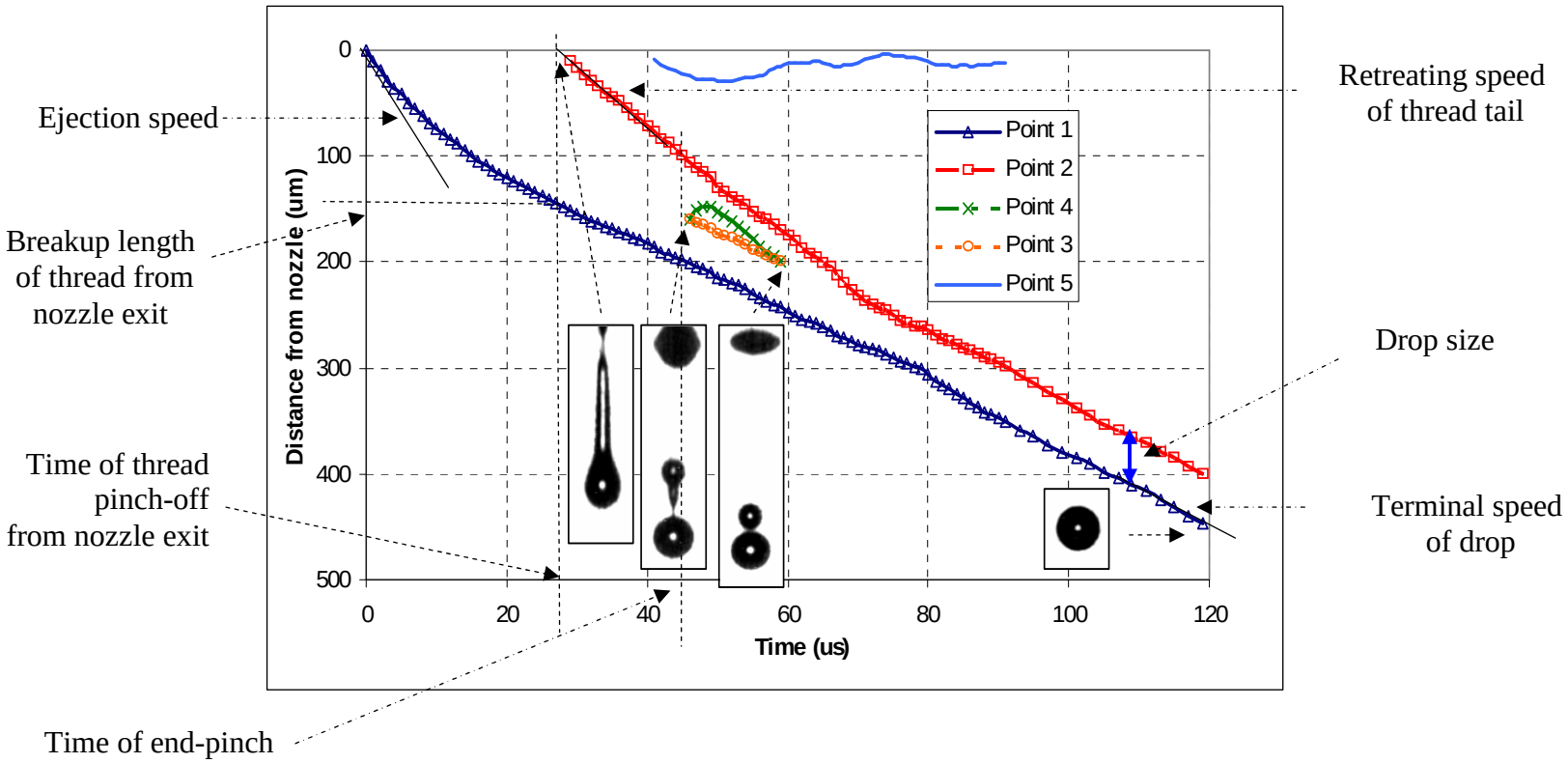

Figure 4-2: Curves of DOD drop formation corresponding to the images shown in Figure 4-1.

Points (3) and (4) are the lower and upper points produced by the second pinch-off, and the curves associated with these points initiate at the second breakup time t_{b2}; these curves form a closed loop if (in the case of a single satellite drop) the satellite recombines with the main drop (as seen in the events of Figure 4-2) or may continue separately if the satellite survives as a discrete body of liquid. Later, Point (3) becomes the tail of the primary drop, and Point (4) becomes the head of the secondary free liquid thread or satellite. Between Points (2) and (4), other pinch-off points may occur, but are not considered here. Point (5) is the tip of liquid protruding from the nozzle orifice due to multiple reflections of the pressure wave inside the ink chamber. Figure 4-2 can be used to calculate parameters related to the drop formation. These parameters include speed of these representative points at various positions, speed of primary drop and satellites, pinch-off length and time of the liquid thread from the nozzle exit, time of breakup of liquid thread into satellite and primary drop, sizes of primary drop and satellite, drop oscillation frequency, and the life expectancy of satellites. However, the evolution of the profile of the ejected liquid versus time cannot be determined from these curves; this requires detailed analysis of the radial extent of the liquid from the flow axis.

4.1.2 Ejection and Stretch of Liquid

When the contracted transducer expands, liquid in the nozzle is accelerated and pushed out of the nozzle orifice. Initially, the meniscus then quickly extends outward until a liquid column with a round leading edge is formed (images 1-3 in Figure 4-1). After a short time (starting at approximately image 4), the liquid flow rate from the nozzle decreases. The difference in axial velocity between the column head and the liquid at the nozzle exit causes the liquid column to stretch. The speed of the liquid at the nozzle exit continues to fall until no additional liquid flows into the column and possibly even some liquid is sucked back into the nozzle due to the negative pressure associated with the second pulse of the waveform causing contraction of the piezoelectric

transducer. The volume of the liquid column remains constant, and the inertia of the liquid continues to extend the column. The rate of extension decreases as new surface is created with the corresponding increase in the surface energy.

4.1.3 Necking and Pinch-off of Liquid Thread From Nozzle

During the stretching of the liquid column, the liquid at the tail (at the nozzle exit) necks. This necking position remains at the nozzle exit, and the radius of the liquid thread here continuously thins (images 5-9 in Figure 4-1). A second necking point (see images 5 and 6) begins to appear towards the head of the column, eventually producing a bulbous head. Thus, a long transitional liquid column is created, reaching from the nozzle to the head. Finally, the tail of the liquid thread pinches off from the nozzle exit, creating a free liquid thread with a bulbous head. In the graphical representation of Figure 4-2, the pinch-off is associated with the appearance of Point 2, at a time of t_{b1} =28 μs.

4.1.4 Recoil of Free Liquid Thread

Recoil occurs because pressure is high in the tail tip at pinch-off. The surface contracts to reduce its surface energy. Since the two ends attached to the liquid thread are not symmetrical, the head and tail behave differently. The tail recoils toward the head as can be seen from Figure 4-2 by the approach of the curve x_2 (tail) toward that of x_1 (head).

4.1.5 Breakup of the Free Liquid Thread

During the shrinkage of the liquid thread, a second neck near the bulbous head continues to evolve until the liquid thread breaks up into two parts, a primary drop and a free secondary and unsymmetrical liquid thread (images 13-16 in Figure 4-1); this corresponds to the appearance of Points 3 and 4 in the graphical representation of Figure 4-2 at a time of t_{b2} = 47 μs. The lower end of the secondary liquid thread literally moves

up the axis toward the nozzle due to the rapid retraction of the thread (seen by the initial positive slope of the $x_4(t)$ curve) while the shape of the upper end is bulbous. Depending on its length, the secondary liquid thread may shrink into a smaller drop or satellite (as illustrated in image 16 in Figure 4-1), or break up into two or more parts. Contraction of the satellite towards a spherical shape may cause the satellite to oscillate as seen in the case considered here in images 16-19 in Figure 4-1, and graphically evident from Figure 4-2 in the minimum in vertical separation between curves x_2 and x_4 (implying flattening of the satellite) seen at a time of about 50 μs.

4.1.6 Formation and Recombination of Primary Drop and Satellite(s)

Breakup of the free liquid thread leads to the generation of a primary drop and satellite(s). In some but not all conditions, the satellite recombines with the primary drop to form a larger drop. In the case illustrated in Figure 4-1, the satellite merges with the primary drop (images 17-20).

If the satellite and the primary drop merge, excess surface energy is transformed into oscillatory kinetic energy of the liquid. Surplus energy is viscously dissipated until an equilibrium state is reached (images 21-28 in Figure 4-1).

After pinch-off of liquid from the nozzle exit, the oscillation of the pressure inside the liquid chamber leads to liquid alternately being forced out of and being sucked back into the chamber, as seen in the behavior of Point 5 in the graphical representation of Figure 4-1 after t = 42 μs and the appearance of liquid at the orifice in images 14-28 in Figure 4-1. For most cases, the weak reflection of pressure wave is not strong enough to cause the liquid to detach from the nozzle exit, so it oscillates with smaller and smaller amplitude until the pressure wave disappears due to viscous dissipation in the chamber.

4.2 Ejection and Stretch of Liquid

In Figure 4-3, the ejection and stretching stages for three liquids are compared under two voltage amplitudes of 21.6 volts and 25.6 volts; voltage will here always imply the peak voltage applied to the piezoelectric transducer. At the early stage of ejection, the liquid thread head exhibits a nearly parabolic profile for the two 5-cP liquids, while for water (1 cP), the profile is nearly flat. In Figure 4-4, the position of the leading edge measured from the nozzle exit versus the radial position measured from the left wall of the nozzle is plotted for the three liquids at time of 4 μs and voltage amplitude of 21.6 V. When a second order polynomial equation is used to fit the data, close fits are obtained for GW and GWI (R-squared value greater than 0.99), showing that the profiles are nearly parabolic. However, the fit of a quadratic function for water is poor (R-squared value of 0.7708) since the profile is nearly flat away from the wall. The early shapes of the liquid thread head are believed to be due to the velocity profiles at the nozzle exit. For flow through a conduit, the length of channel required to obtain fully developed flow where a parabolic profile occurs varies proportional to Reynolds number [59]. As the liquid viscosity decreases, the required entrance length for fully developed flow increases.

Apparently, the viscosity of the 5-cP liquids is sufficiently high for fully developed flow to be approached at the nozzle exit, but the viscosity of water (1 cP) is too low and nearly plug flow occurs at the nozzle exit. Under the voltage amplitude of 21.6 volts, the Reynolds number ($\mathrm{Re} = 4Q\rho/(\pi D_{noz}\mu)$) for water, GW and GWI is approximately *Re* = 219, 33 and 30, respectively. In the relationship for Re, Q is volumetric flow rate, ρ is density, D_{noz} is nozzle diameter, and μ is viscosity.

At the early stage of ejection, surface tension does not have a significant effect on the shape of ejected liquid. However, during the stretching process, the high surface

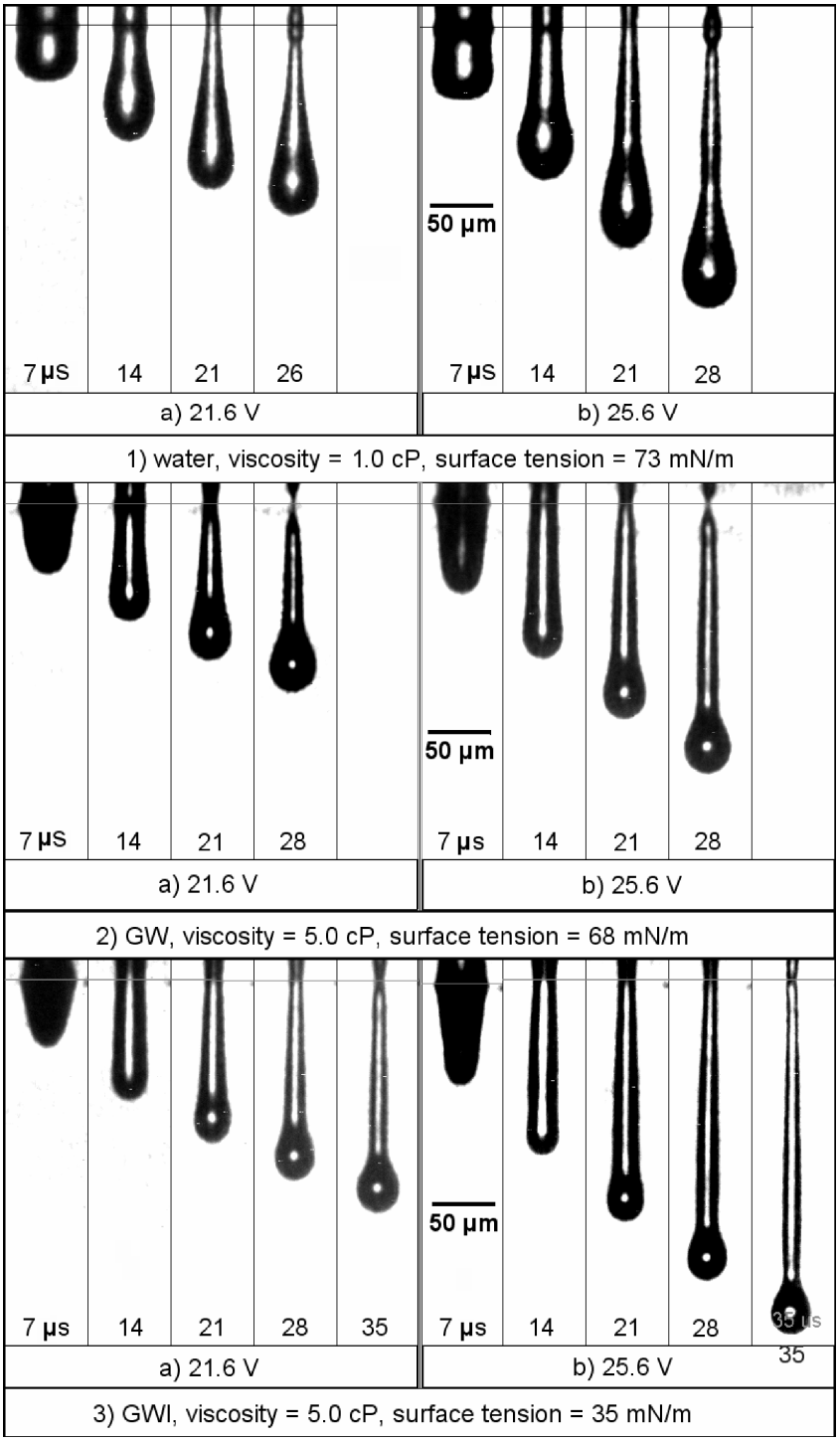

Figure 4-3: Sequential images of ejection and stretching of three liquids (top to bottom: water, GW, and GWI) using the double-peak waveform in Figure 3-5 with voltage amplitudes of 21.6 and 25.6 V and frequency = 20 Hz.

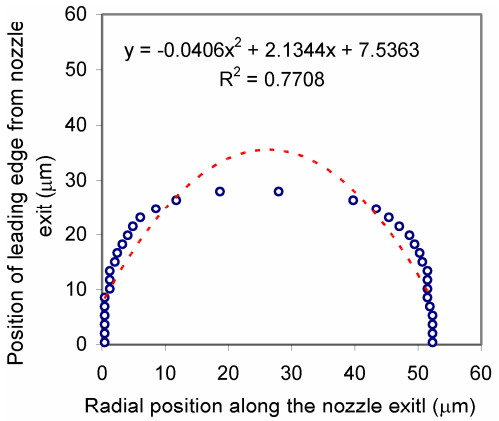

a)

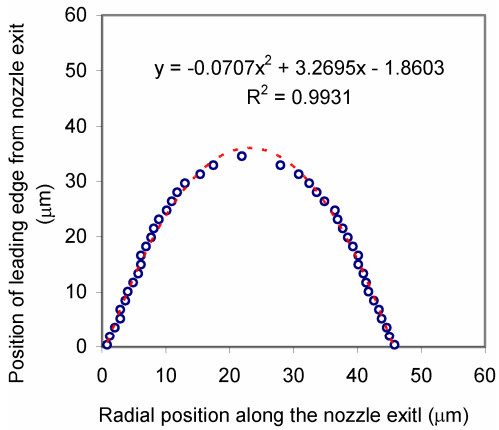

b)

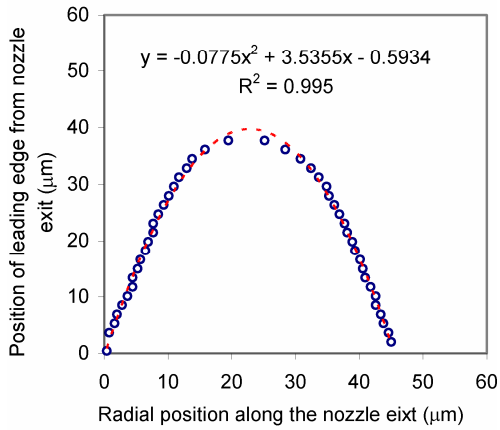

c)

Figure 4-4: Position of leading edge of Water, GW and GWI at 4 μs using the double-peak waveform with voltage amplitude = 21.6 V and frequency = 20 Hz. X-axis is the radial position along the nozzle exit, and Y-axis is the distance of the leading edge from the nozzle exit. The dashed line is the fitted curve using 2nd polynomial regression, and "◦" indicates the measured values.

tension liquid necks faster and forms a larger bulbous head. The bulbous head for water (1 cP) is larger than that for the 5-cP liquids, and the taper in the surface from the head to the nozzle exit appears to be straight for water, but has an observable inflexion for the 5-cP liquids. For the water ejected using the higher voltage, capillary waves on the long transitional section of the water thread are observed (see Figure 4-3 (1-b), 28 µs), and these lead to multiple breakup as will be discussed in Section C. The pinch-off for water is much more abrupt than for the higher viscous liquids, and a small bulbous tail appears soon after pinch-off (see Figure 4-3 (1a-and 1b), 26 and 28 µs, respectively).

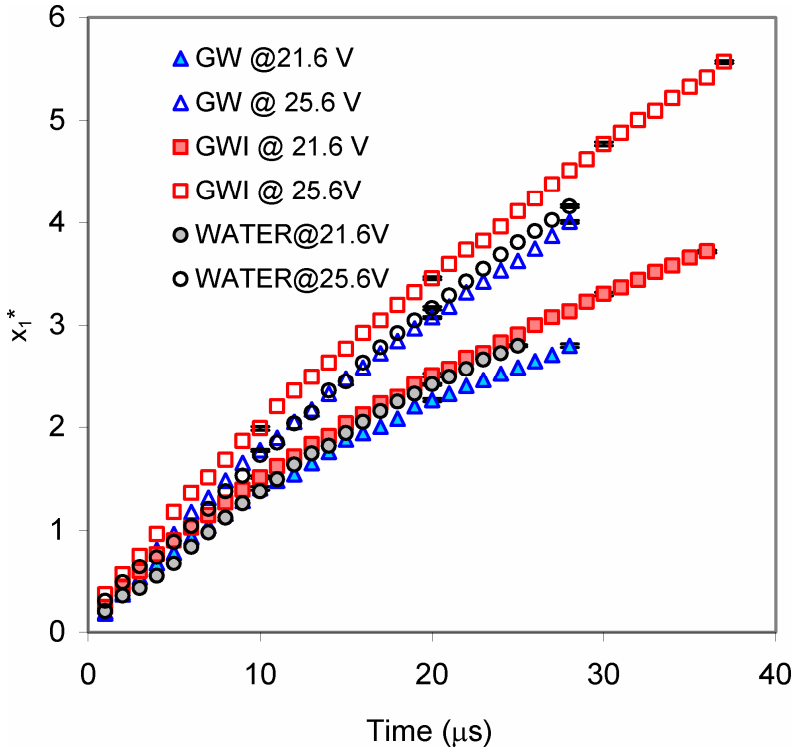

Figure 4-5: Temporal variation of x_1* before pinch-off from the nozzle exit for three liquids using the double-peak waveform in Figure 3-5 with voltage amplitudes of 21.6 and 25.6 V and frequency = 20 Hz. x_1* is the ratio of the distance of Point 1 from nozzle, x_1, to the nozzle diameter (53 µm). Highest time shown for each plot corresponds to the time of pinch-off from nozzle exit. The standard deviations of position are less than 1 µm.

In Figure 4-5, the temporal variation of x_1 is shown for the three liquids. Pinch-off occurs at the last time shown in each of the plots. The liquid pinch-off length, $l_b = x_1$ at t_{b1}, increases with the driving voltage amplitude. The speed of Point 1 (dx_1/dt) decreases as it moves away from the nozzle, and is higher for a driving voltage of 25.6 volts than for 21.6 volts. The ejected liquid separates from the nozzle exit in less than 40 µs (see last time in each of the plots in Figure 4-5). Separation occurs much faster for DOD ejection than for the dripping mode where it takes about 100,000 µs.

Table 4-1: Ejection speed and speed of Point 1 at pinch-off from nozzle exit.

Liquid	Voltage (volt)	Ejection Speed, v_e (m/s)	Speed of Point 1 at pinch-off from nozzle exit, v_{b1} (m/s)
Water	21.6	6.8	4.2
	23.6	7.4	4.9
	25.6	9.2	6.3
GW	21.6	8.2	3.4
	23.6	9.0	4.9
	25.6	10.5	6.1
GWI	21.6	8.2	3.8
	23.6	9.5	4.8
	25.6	10.9	5.9

The speed of Point 1 depends on surface tension and the time to pinch-off. The higher the surface tension, the more kinetic energy is required to form new surface. As the pinch-off time increases, the stretching increases, resulting in more new surface being formed. At pinch-off, the velocity (v_{b1}) of Point 1 for the three liquids differs slightly, but the shapes of the liquid thread are significantly different.

In order to investigate further the flow behaviors during ejection and stretching, the volume and surface area of liquid ejected are calculated at different times. The edges

of the 2-D images of the liquid thread are identified as a function of distance from the nozzle. Assuming axisymmetry, a body of rotation is formed, and the volume and surface areas are computed. Results for three liquids under voltage amplitude of 21.6 V are given in Figure 4-6. Ejection time (t_e), time from emergence of liquid from the nozzle until the ejected volume reaches its maximum, is about 10 μs for water and GW, and 9 μs for GWI. Stretching (including suction of liquid back into the nozzle) ensues until the liquid thread snaps off from the nozzle. After that, the volume of the free liquid thread remains constant, but the surface area decreases toward a minimum value, a spherical shape, which occurs at about 65, 75, and 240 μs for water, GW, and GWI (for which the complete time is not shown in Figure 4-6 (b)), respectively. The final ejected liquid volumes for GW and GWI, which have the same viscosity, are similar and are about 40% smaller than that of water.

Average flow rates from the nozzle during the ejection stage can be determined from the plots in Figure 4-6 (a). The average flow rates for water, GW and GWI are 9.1×10^{-3} ml/s, 6.1×10^{-3} ml/s and 5.9×10^{-3} ml/s, respectively. When the signal waveform and signal amplitude are fixed, the average flow rate during ejection depends on the liquid viscosity, with the reduction seen here being roughly one-third with a factor of five increase in viscosity.

The volume (see Figure 4-6 (a)) of ejected liquid decreases after about 10 μs indicating that some of liquid is sucked back into the nozzle, but surface area (see Figure 4-6 (b)) continues to increase until a maximum surface area is reached when the liquid thread pinches off from the nozzle exit (marked by "+"). Stretching of the liquid thread before pinch-off from the nozzle exit is apparently caused by not only the inertial motion of the liquid head, but also by the negative pressure in the nozzle which pulls some liquid back into the nozzle. This negative pressure to produce this suction may result from the

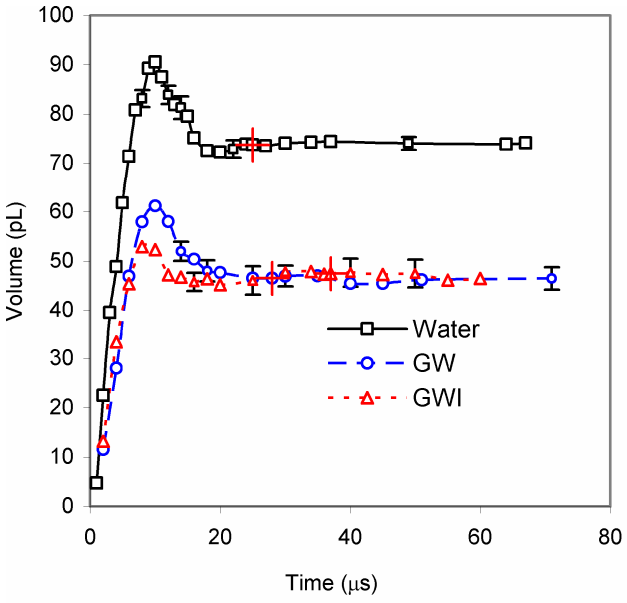

a)

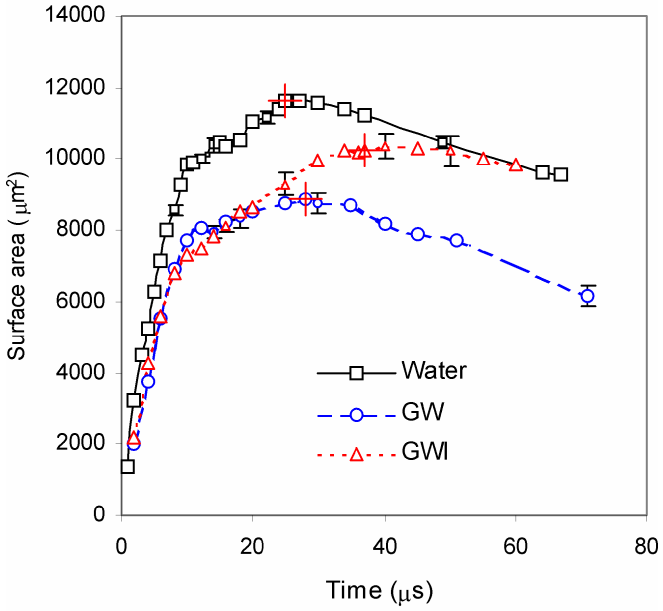

b)

Figure 4-6: Volume and surface area of ejected liquid vs. time using the double-peak waveform with voltage amplitude = 21.6 V and frequency = 20 Hz. Marker "+" indicates the time of liquid separation from the nozzle exit. The error bar stands for one standard deviation.

signal waveform, pressure wave reflections in the channel [21, 38, 67] and the liquid-reservoir pressure. It is, in principle, tunable within certain limits through the waveform.

The pinch-off time (t_{b1}), required for the ejected fluid to stretch and then pinch off from the nozzle exit, varies little with the voltage amplitude of the driving signal. For water, GW and GWI, t_{b1} is approximately 25, 28 and 37 μs, respectively. The surface tensions of these three fluids are 73, 68 and 35 mN/m, respectively. Thus, the liquid with lower surface tension and higher viscosity survives stretching longer before pinching off from the nozzle exit. Pinch-off time is meaningful in application, as it fundamentally sets the maximum rate of drop formation for the DOD generator, and can be changed by varying the signal waveform, as will be discussed in Section 4-7.

4.3 Breakups of Liquid Thread

The breakup of a liquid thread has been studied for drop formation in the drip and continuous modes and in surrounding viscous liquids. Eggers [23] determined the scaling functions that define the shape of the thread and the velocity field within the liquid thread close to the pinch-off point. Shi et al. [76] observed in their dripping experiments that the primary thread evolved a secondary thread and sometimes a tertiary thread. Henderson et al. [40] found in their dripping experiments that the primary thread necks into a secondary thread exhibiting a wave-like instability that leads to breakup without a preferred Rayleigh wavelength. Similarly, Kowalewski [46] observed that the secondary threads of continuous jetting also have instability to disturbances with a broad distribution of wavelength. Stone et al. [81] showed that the relaxation and breakup of initially stretched drops in viscous fluid depended on the viscosity ratio of the two liquids and stretching length. Two modes of breakup of liquid thread were observed in their experiments: multiple breakup due to capillary waves in a sufficiently long thread and a new breakup mechanism that was referred as “end-pinching,” where spherical drop pinches off from the end of the liquid thread.

In order to capture liquid thread breakup, most of the previous experimental studies were performed using millimeter drops and/or highly viscous liquids so that the necking process would be slow enough to be observed using a high-speed camera. Kowalewski [46] investigated liquid thread breakup into micron-scale drops for continuous jetting; however, no investigation was found in the literature for liquid thread breakup for DOD drop formation. Our experimental results were obtained from a DOD drop generator using low viscosity fluids and at micron scale.

4.3.1 Modes of Liquid Thread Breakup

Two modes of liquid thread breakup were observed in our experiments: end-pinching and multiple breakup due to the wave-like instability. Figure 4-7 demonstrates liquid thread breakup of three liquids ejected from a DOD generator for several voltages. For water (Figure 4-7-1), the evolution of the liquid thread is related to the length of the liquid thread at pinch-off which increases with voltage. For the shorter water threads (Figure 4-7-1-a and b), a capillary wave is not observed, and satellite formation resulted from end-pinching, a process where the liquid thread pinches off from an almost spherical head. For longer water threads (Figure 4-7-1-c and d), a wave-like instability occurs along the thread. The capillary wave does not show any preferred wavelength as predicted by Lord Rayleigh [65]. As the amplitude of the capillary wave increases the liquid thread breaks up at several different times forming several parts of varying sizes. The longer the liquid thread, the more satellites are formed. For higher viscosity liquids (Figure 4-7-2 and 3), capillary waves do not appear, but end-pinching is observed. There is no further breakup within the secondary liquid thread for most cases. The secondary thread eventually contracts into a single drop. However, at higher voltages (25.6 volts in Figure 4-7-3), necking is observed in the secondary thread during its contraction, and breakup of the secondary thread occurs at approximately 130 μs (see Figure 4-8).

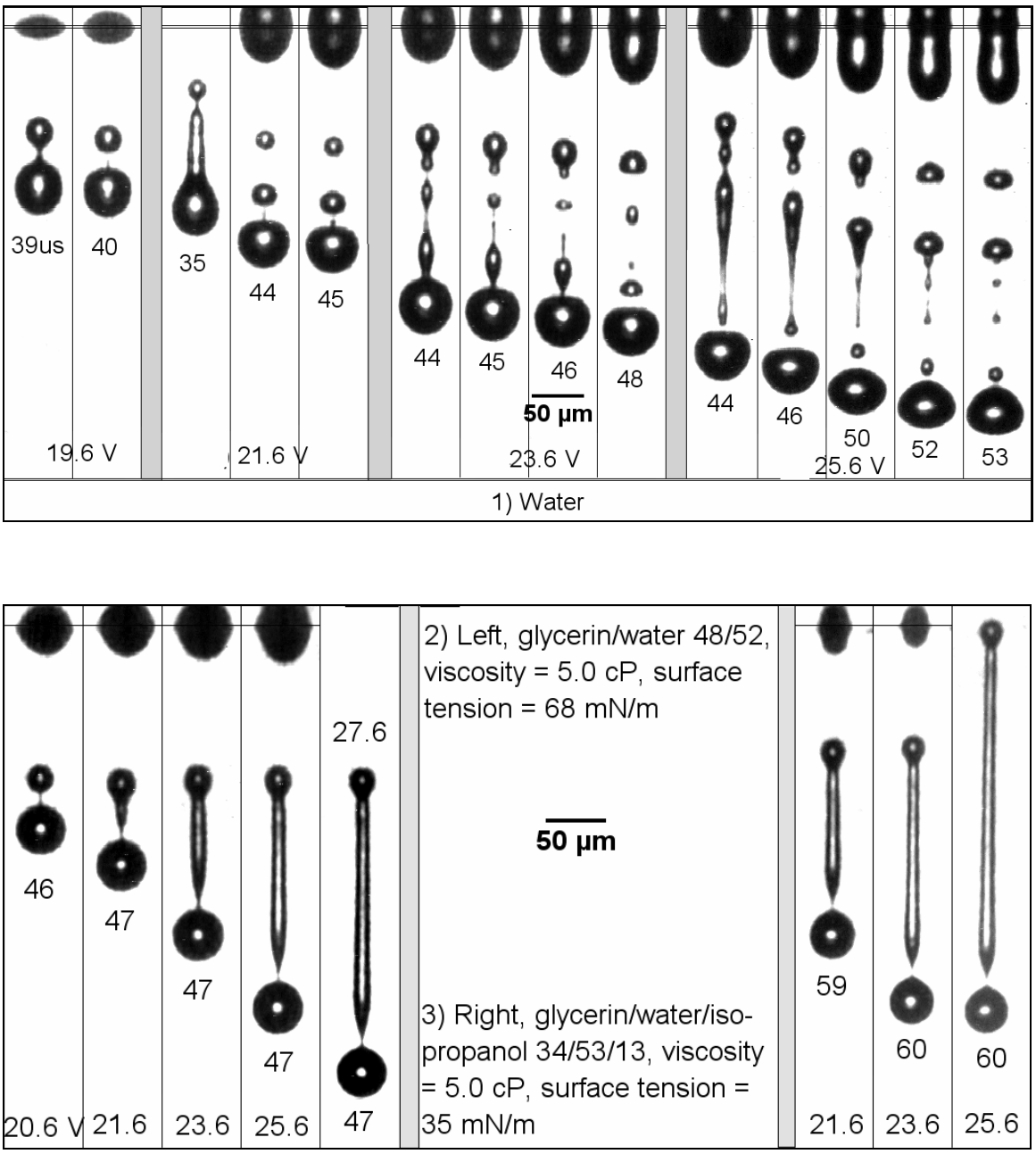

Figure 4-7: The effect of driving voltage and liquid properties on the breakup(s) of the liquid thread using the double-peak waveform with several voltage amplitudes and frequency = 20 Hz. Times below each drop are in microseconds from first fluid exit from orifice, and value at the bottom of each frame is the voltage amplitude of driving signals.

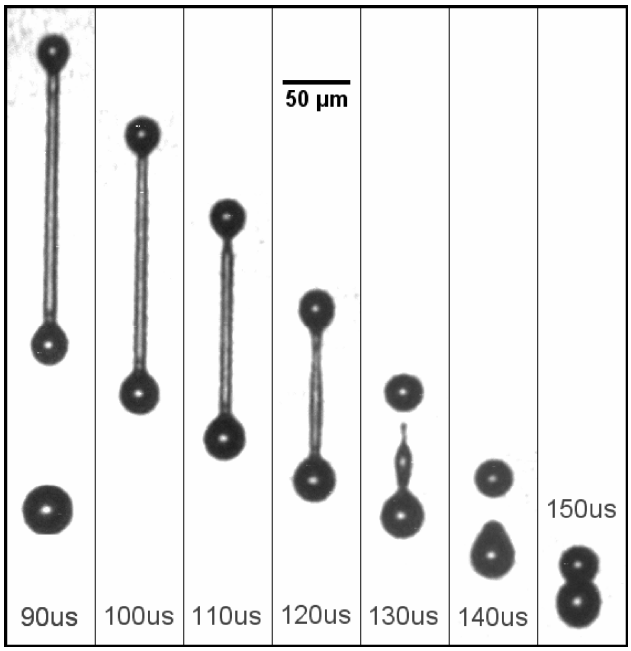

Figure 4-8: Breakup of the secondary liquid thread for GWI at using the double-peak waveform with voltage amplitude = 25.6 V.

Multiple breakups evolving from the wave-like instability complicate the generation of satellites and are unfavorable for DOD drop formation. Increasing the liquid viscosity can eliminate multiple breakups. Although end-pinching of the liquid thread may occur, it is more predictable. Prior studies have provided criteria for the observation of end-pinching, and we consider our results in comparison with these criteria.

Brenner et al. [10] examined the stability of Eggers' similarity solution to perturbations and found that the perturbations either decayed or grew depending on the value of the similarity variable ζ compared to its value at the stagnation point of thread ζ^*. Analysis of the local growth rate shows that perturbations originating for $\zeta > \zeta^*$ are damped. Depending on their initial amplitude, perturbations starting with $\zeta < \zeta^*$ become either 1) a blob, which distorts the shape of the interface as wave-like disturbances, or 2) a neck, a transitional region between primary and secondary threads.

Schulkes [75] performed numerical simulations which predicted that end-pinching does not occur when the Ohnesorge number, $Oh = \mu / \sqrt{\rho r_0 \gamma}$ (μ is the viscosity of liquid, ρ is density, γ is surface tension, r_0 is radius of thread) is greater than a critical value, Oh^*, which is in the range of $0.005 < Oh^* < 0.01$. In the present experiments, end-pinching occurred for GW and GWI with Oh of 0.112 and 0.161 based on the radius of the nozzle (greater than the liquid thread radius), respectively, which the Schulkes numerical simulations predict would not occur. However, the present experimental results agree well with the prediction of Notz and Basaran [57], which showed that when Oh< O(0.1), the filaments with sufficiently large initial aspect ratios pinch-off daughter drops from their ends through the so-called end-pinching mechanism.

Another criterion for the pinch-off of liquid threads was proposed by Henderson et al. [39]. If the most unstable wave mode has the longest wavelength that fits the finite length of the thread, then the liquid thread pinches off near its ends (end-pinching). If the wavelength with the most unstable wave mode is shorter than the length of the thread, then pinch-off occurs at one or more interior points (multiple breakup). This idea along with a simple linear stability estimate of the most unstable mode is used in the next section to analyze the breakups of liquid thread in DOD drop formation.

4.3.2 Breakup Time of Liquid Threads

Multiple breakup and end-pinching both originate from the growth of disturbances along liquid thread. For a normal-mode disturbance that can be modeled as a traveling wave along the axis of the thread, z, the amplitude of disturbance is given by

$$\varepsilon' = \hat{\varepsilon} \exp(ikz + \alpha t) \tag{1}$$

where $\hat{\varepsilon}$ is the initial amplitude of disturbance, $k = 2\pi/\lambda$ is the wave number, λ is the wavelength, α is the temporal growth rate, z is the distance along the axial direction of liquid thread and t is time.

Using the results from the linear instability analysis (see Egger, 1997), the fastest growth mode can be approximated by

$$x_{\max}{}^2 = (k_{\max} r_0) = \left(\frac{2\pi r_0}{\lambda_{\max}}\right)^2 = \frac{1}{2+\sqrt{18}Oh} \quad (\lambda_{\max} \text{ is the corresponding wavelength})$$

(2)

The corresponding grow rate is

$$\alpha_{\max}{}^* = \alpha_{\max}\left(\frac{\rho r_0{}^3}{\gamma}\right) = \left\{\left[\frac{1}{2}x_{\max}{}^2\left(1-x_{\max}{}^2\right)+\frac{9}{4}Oh^2 x_{\max}{}^4\right]-\frac{3}{2}Oh\, x_{\max}{}^2\right\}$$

(3)

If we assume that the first pinch-off from the nozzle exit or end-pinching are both caused by the most unstable disturbance, then the radius of this disturbance grows as,

$$\varepsilon = \varepsilon_{\max} \exp(\alpha_{\max} t) \tag{4}$$

where ε_{max} is the initial amplitude of the disturbance corresponding to $\alpha_{max.}$

Hence, if the radius of thread r_0 is scaled by the radius of the nozzle exit, R_{noz}, and the liquid thread breaks up when the amplitude of disturbance reaches the radius of liquid thread, the time at which the liquid thread pinches off can be approximated by

$$t_b = \frac{1}{\alpha_{\max}{}^*}\left(\frac{\rho R_{noz}}{\gamma}\right)^{1/2} \ln\left(\frac{R_{noz}}{\varepsilon_{\max}}\right) = C\frac{t_{ca}}{\alpha_{\max}{}^*} \tag{5}$$

where $C = \ln\left(\frac{R_{noz}}{\varepsilon_{\max}}\right)$ which is a constant only related with radius of nozzle and external noise amplitude; $t_{cp} = \left(\frac{\rho R_{noz}{}^3}{\gamma}\right)^{1/2}$, the capillary time of the liquid.

Thus, the breakup time of a liquid thread should depend only on the capillary time and $\alpha_{\max}{}^*$. This agrees well with our experimental results. Table 4-2 lists the time of the pinch-off from nozzle and end-pinch of three liquid threads ejected under different

Table 4-2: Breakup times of three liquid threads and related parameters.

Liquid	Voltage (volt)	t_{b1} (μs)	t_{b2} (μs)	t_{ca} (μs)	Oh	α_{max}^{*}	$\frac{t_{ca}}{\alpha_{\max}^{*}}$ (μs)	C_1	C_2
Water	19.6	24	40	16.0	0.0227	0.337	47.5	0.29	0.63
	21.6	25	43					0.32	0.69
	23.6	27	44					0.36	0.72
	25.6	28	44					0.38	0.72
GW	21.6	28	46	17.4	0.112	0.286	60.8	0.30	0.59
	23.6	28	47					0.30	0.61
	25.6	28	47					0.30	0.61
	27.6	28	47					0.30	0.61
GWI	21.6	37	59	23.5	0.161	0.264	89.0	0.31	0.56
	23.6	39	60					0.34	0.57
	25.6	38	60					0.32	0.57

driving voltages. The pinch-off times do not vary with voltages or ejection speeds and ejection lengths.

For the pinch-off of the liquid thread from the nozzle exit or the first breakup, the constant $C_1 = \frac{t_{b1} - t_e}{t_{ca} / \alpha_{\max}^*}$ is in the range of 0.3 - 0.4, and for the end-pinching or the time, and t_{b2} is the second breakup time. Here, the ejection time, t_e, is subtracted from the experimental breakup time to obtain real breakup time because the liquid thread is completely formed after completing ejection stage (Figure 4-1). It should be noted that the first breakup from nozzle and end-pinching have different mechanisms, which leads to different values. The first breakup occurs during stretching of the liquid thread, while the end-pinching takes place during contraction of thread.

The variation in C_1 and C_2 for water is larger than for the viscous liquid. From the definitions of C_1 and C_2, we can find that the $R_{noz} / \varepsilon_{\max} > 1$ for the two pinch-offs. However, one of the assumptions for linear instability analysis is $r_0 / \varepsilon_0 >> 1$. Therefore, there must be some other better mechanisms to describe the DOD two breakups. However, the linear instability analysis still can provide good approximations for the breakup times of liquid threads

4.3.3 Breakup Length of Liquid Thread

The breakup length of the liquid thread at pinch-off from the nozzle varied with signal voltage and therefore with the ejection speed as shown in Table 4-3. The ratio of breaking length to nozzle radius varied from 4.8 to 11.4. Lopez et al. (2002) suggested that there is a lower limit of breaking length to nozzle radius for ejection to occur.

From our study, it can be concluded that the breakup time, i.e., growth time of disturbances, is almost constant. Therefore, the breakup length of the liquid thread is determined by time and ejection speed. The breakup of liquid thread occurs only if the

disturbance has enough time to grow before the liquid is sucked back into the nozzle. For a given liquid, breakup length increases with increasing driving voltage because the breakup time was constant while the ejection speed is higher.

Table 4-3: Breakup length of three liquid threads under various driving voltages

Liquid	Voltage (vlot)	Breakup length/radius of nozzle, l_b/r_0	Wavelength of most unstable wave /r_0
Water	19.6	4.8	9.1
	21.6	5.8	
	23.6	7.0	
	25.6	8.4	
Glycerin/water 48/52	21.6	5.6	9.9
	23.6	6.9	
	25.6	8.1	
	27.6	9.5	
Glycerin/water /isopropanol 39/61/15	21.6	7.4	10.3
	23.6	9.1	
	25.6	11.4	

4.4 Contraction of Liquid Thread

After the liquid snaps off from the nozzle exit and becomes a free-flying thread, the thread tail (Point 2) recoils rapidly under the action of the surface tension. Eggers[23] provided a model for predicting the retreating speed of the liquid thread tail; however, the analysis of Eggers is valid only in the pinch-off region, i.e., $l/l_v < 1 \text{ and } t/t_v < 1$, where l is the distance that the free end has moved from the pinch-off point, t is time measured from pinch-off, $l_v = \rho\nu^2/\gamma$ and $t_v = \rho^2\nu^3/\gamma^2$, and ρ, ν and γ denote the density, kinematic viscosity (μ/ρ) and surface tension, respectively. For low viscosity liquids that the DOD drop generator normally utilizes, this prediction has little

engineering significance for drop formation processes because it provides the speed at only extremely small values of *l* and *t*, i.e., at pinch-off (see Table 3-2). Hence, we will focus our attention on the retreating of the liquid thread tail beyond the pinch-off region in an effort to provide a basis for predicting its retraction speed.

Some experimental studies [40, 46] have reported that the retreating speed of the tail of the liquid thread had a power-law dependence on time. Numerical simulations [57, 75] also found that the relationship between retreating speed and time was nonlinear. Without considering effects of viscosity, Keller [43] derived the following equation giving the end position *Z* of a liquid thread lying along the *z* axis after its breakup:

$$Z(t) = t^{2/(2+\beta)} \left(\frac{\gamma(2\beta+1)(2+\beta)^2}{\rho b(3\beta+2)} \right)^{1/(2+\beta)} \tag{6}$$

where β and b are the constants in $r(z) = bz^{\beta}$ and $r(z)$ is the radius of a thread with a circular cross section.

The sequential images and curves of DOD drop formation obtained in this work show that the tail of liquid thread retreats at an almost constant speed and the leading edge of the liquid thread also moves at almost constant speed until the second breakup occurs. Kowaleski [46] also found in his continuous jetting experiments that the macro-thread speed is almost constant for a while, and then decreased when it began to form a spherule. From the DOD drop formation curves, we obtain the average retreating speed of Point 2, $v_r = \left| dx_2 / dt \right\|_{t_{b1} \to t_{b2}}$, from pinch-off from the nozzle to the second breakup, and the speed of the liquid thread head (Point 1) at the second breakup, $v_{b2} = \left| dx_1 / dt \right\|_{t_{b2}}$. These speeds are tabulated in Table 4-4. As the signal voltage rises, the thread head speed increases while the retreating speed remains almost constant. The retreating speed is determined primarily by liquid properties.

If the retreating speed is constant as found in our results, then, in equation (6), $\beta = 0$, and $b = r_0$ (r_0 is the radius of a liquid thread). The retreating speed, v_r, is

Table 4-4: Speed of liquid head, retreating speed of liquid tail, capillary speed, and parameter *a*.

Liquid	Voltage (volt)	Speed of Point 1 at second breakup (v_{b2}) (m/s)	Retreating speed of tail ν_r (m/s)	Capillary speed ν_{ca} (m/s)	*a* (ν_r/ν_{ca})
Water	21.6	3.4	4.7	1.66	2.8
	23.6	4.5	4.9		3.0
	25.6	5.8	4.8		2.9
GW	21.6[a]	2.9	5.4	1.53	3.5
	23.6[a]	4.1	5.3		3.5
	25.6	5.5	5.3		3.5
	27.6	6.7	5.3		3.5
GWI	21.6[a]	3.6	4.0	1.13	3.5
	23.6	4.9	3.9		3.5
	25.6	6.0	3.9		3.5

[a] Recombination of satellite and primary drop occurs

$$v_r = \frac{dZ}{dt} = \left(\frac{2\gamma}{\rho\, r_0} \right)^{1/2} \tag{7}$$

Note that r_0 here is the radius of the liquid thread. If the radius of liquid thread is scaled by the radius of the nozzle, R_{noz}, then

$$v_r \approx a v_{ca} \tag{8}$$

where a is a constant and $v_{ca} = \left(\frac{\gamma}{\rho R_{noz}} \right)^{1/2}$, referred to as capillary speed. Thus for a given liquid, capillary speed can be used to estimate the retreating speed. The speed of the liquid head, retreating speed of the liquid tail, capillary speed, and the parameter a for three liquids ejected for three driving voltages are given in Table 4-4. The results indicate that the parameter a is approximately constant for each of the three liquids over the range of driving voltages used. The value of a for water (1cP) is slightly lower than for the 5-cP liquids.

4.5 Primary Drop and Satellite

4.5.1 Size

The evolution of the free flying liquid thread depends on the liquid and driving voltage. If driving voltage is sufficiently low, no satellites are formed, as will be discussed in Section 4.6. At higher voltages, breakup of the free flying liquid thread occurs, and satellites are formed. As discussed in Section 4.3, the mode of breakup is multiple breakup for water while it is end-pinching for the 5-cp liquids. The number of satellites for water varies with driving voltage: 0, 1, 2, 4, and 5 for voltages of 17.6. 19.6, 21.6, 23.6 and 25.6 volts, respectively. A wide distribution of satellite size occurs for water, as can be seen in Table 4-5. Although the number of satellites varies greatly with driving voltage, the outcome for a given voltage is reproducible.

For the 5-cP liquids, the free flying liquid thread creates a primary drop and a liquid thread. In most cases, there is no further breakup within the liquid thread, and it eventually contracts into a single satellite. However, at higher voltages (25.6 volts in Figure 4-7-3), necking is observed in the liquid thread during its contraction, and breakup of the thread occurs. Although two separate satellites are formed, they quickly recombine to form a single satellite, as shown in Figure 4-8.

The diameters of the primary drops and satellites for the three liquids under different driving voltage are given in Table 4-5. As driving voltage is increased, the size of the primary drop increases slightly for water, but does not vary significantly for the 5-cp liquids. As driving voltage is increased, the size and number of satellites depend on the liquid. For water, the number of satellites increases, and various sizes of satellites are

Table 4-5: Sizes of primary drops and satellites.

Liquid	Voltage (volt)	Primary drop		Satellites	
		d_p(μm)	d_p/D_{noz}	d_s (μm)	d_s/D_{noz}
Water	17.6	47.5±0.3[a]	0.90	No satellite	--
	19.6	46.5±0.5	0.87	26.9±0.7	0.51
	21.6	48.6±0.4	0.92	Two satellites 18.9±0.6 / 24.2±0.5	036/0.46
	23.6	50.0±0.5	0.94	Four satellites (4.2±0.7 /13.1±1.2 / 19.6±0.6 / 24.7±0.9)	0.08/0.25/0.37/0.47
	25.6	51.0±0.5	0.96	Five satellites (9.2±0.9 / 9.7±0.6 / 14.7±0.6 / 25.5±0.7 / 26.9±0.5	0.17/0.18/0.28/0.48/0.51
GW	21.6	42.6±0.4	0.80	26.3±0.3	0.50
	23.6	43.6±0.4	0.82	31.5±0.5	0.59
	25.6	43.9±0.3	0.83	36.3±0.4	0.68
	27.6	43.8±0.3	0.83	40.8±0.3	0.77
GWI	20.6	39.9±0.6	0.75	30.3±0.5	0.57
	21.6	39.7±0.3	0.75	32.2±0.5	0.61
	23.6	39.4±0.3	0.74	36.6±0.4	0.69
	25.6	39.2±0.5	0.74	40.5±0.3	0.76

a. one standard deviation

found. For the 5-cp liquids, only one satellite is formed with one exception. At a driving voltage of 25.5 volts for GWI two satellites are formed; however, the two satellites quickly merge into a single satellite. Satellite size increases with driving voltage, and at higher voltages, it is comparable to primary drop size. The size of the primary drop depends on liquid properties. The ratio of primary drop diameter of water to diameter of GW and GWI is 1.15 and 1.27, respectively. The ratios of the diameter of the primary drop to the diameter of the nozzle lie in the range of 0.75-1.0.

4.5.2 Combination of Primary Drop and Satellites

In some cases, the primary drop and satellite merge into a large drop. Without considering the action of the surrounding air, the necessary condition for their merger is that the speed of the satellite, v_s, should be higher than that of the primary drop, v_p. However, when primary drop and satellites move through the ambient air, the drag force exerted by air slows them down. According to Dijksman (1984), the deceleration, a, of a drop with a radius of r_d and velocity, v, is:

$$a = -4.577\left(\frac{\rho_{air}^{2/5}\mu_{air}^{3/5}}{\rho_{liquid}}\right)\left(\frac{v^{7/5}}{r_d^{8/5}}\right) \qquad (9)$$

where ρ_{air} is the density of the surrounding air, ρ_{liquid} is the density of drops, and μ is the viscosity of the air. From Figure 4-9, for a drop with a diameter of 20-50 μm and speed of 3-5 m/s, the deceleration is in the order of 10^3 m/s^2 (or 10^{-3} μm/μs^2). For a 10-μm satellite, it is about 10^4 m/s^2 (or 10^{-2} μm/μs^2). Thus, smaller satellites encounter larger deceleration in air than larger primary drops. For smaller satellites generated due to multiple breakups, as occurs in the water thread, the air drag tends to cause them to rear-merge, i.e., the tiny drops merge with the last larger satellite. In our experiments, when rear-merging occurred, the at least one satellite did not merge with the primary drop. For

larger satellites produced by end-pinching, as occurs in the 5-cPs threads, the drag force is less important, and merger occurs sometimes.

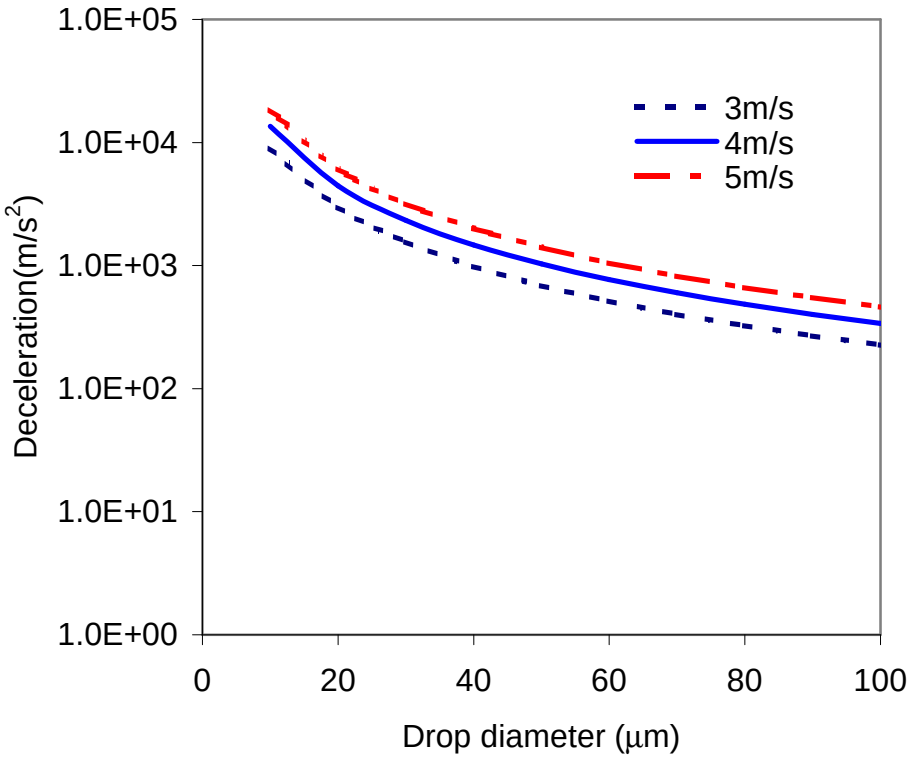

Figure 4-9: Deceleration vs. drop size and speed due to the air drag (ambient fluid: air. $\rho_{air} = 1.2 kg/m^3$, $\rho_{liquid} = 1000 kg/m^3$, $\mu_{air} = 1.85 \times 10^{-5}$ Pa·s).

In the following discussion, the drag force is neglected and a necessary condition for merger of the satellite, formed via end-pinching, with the primary drop to form a single drop is determined. For the discussion, several velocities will be used: capillary velocity (v_{ca}), primary drop velocity (v_p), satellite velocity (v_s), final single drop velocity (v_d), velocity of Point 1 at the second breakup (v_{b2}), and the retreating speed (v_r).

When the flying thread breaks up into a primary drop and a secondary thread (see Figure 4-1), the head of the secondary thread (Point 4) recoils from Point 3, and the

distance between Point 4 and Point 2 ($|x_2-x_4|$) decreases. Thus the speed of Point 4 is lower than the retreating speed (speed of Point 2), and the final speed of the satellites will not exceed the speed of the thread tail, i.e., $v_s < v_r$. On the other hand, when end-pinching occurs, the speed of Point 1 varies little (for example, see Figure 4-2). Thus the speed of the primary drop, v_p, is the same as the speed of Point 1 of the ejected thread at end-pinching, v_{b2}. Thus a necessary condition for merger of the satellite with the primary drop is that the speed of the primary drop

$$av_{ca} \approx v_r > v_s > v_p \approx v_{b2} \tag{10}$$

The importance of the relative magnitudes of v_{b2} and v_r in determining whether or not the satellite and primary drops merge can be illustrated using data for GW in Table 4-4 and curves of drop formation shown in Figure 4-10. For GW, when the voltage amplitude is 23.6 volts, $v_r > v_{b2}$; but when the voltage amplitude is 25.6 volts, $v_r < v_{b2}$. In the first case (see Figure 4-10 (a)), the satellite and primary drop merge at time = 190 μs while in the second case (see Figure 4-10 (b)), the distance between primary drop and satellite increases with time, and this indicates that they do not merge. More examples are listed in Table 4-4.

The maximum speed that the final drop can have for DOD drop formation can be estimated by considering the kinetic energy of the final drop and using the relationships between v_p, v_s, and v_r. Before the recombination of the primary drop and satellites, the total kinetic energy is $1/2m_p{v_p}^2 + 1/2m_s{v_s}^2$. The kinetic energy of the final drop is $1/2m_d{v_d}^2 = 1/2(m_{p/2} + m_s){v_d}^2$, where m_d, m_p, and m_s are the masses of the final drop, primary drop, and satellite, respectively; and v_d, v_p, and v_s are the speeds of the final drop, primary drop, and satellite, respectively. If the effect of surface energy is neglected, the kinetic energy of final single drop should be less than the total energy of

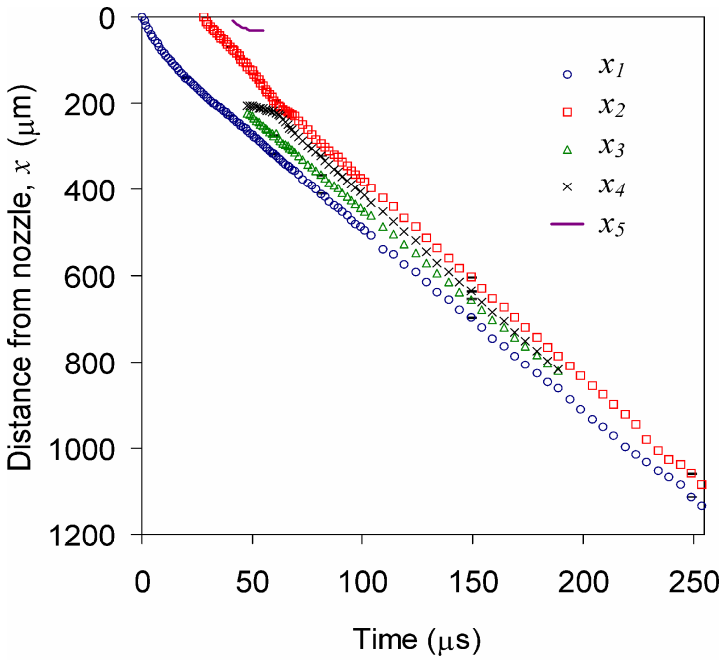

a)

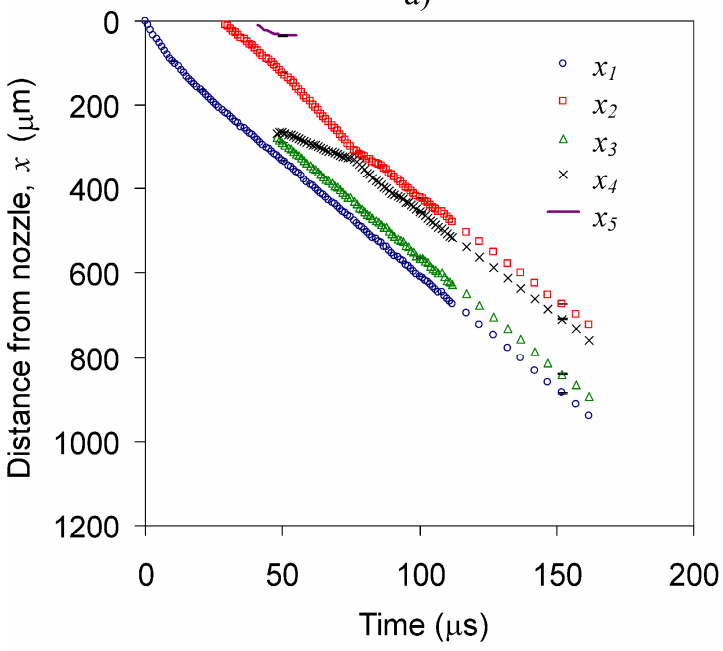

b)

Figure 4-10: DOD drop formation curves for GW using the double-peak waveform with voltage amplitudes of 23.6 and 25.6 V and frequency = 20 Hz. The primary drop and satellite: a) recombine for driving voltage of 23.6 V and b) do not recombine for driving voltage of 25.6 V.

primary drop and satellite due to the viscous dissipation associated with the flow due to recombination, i.e.,

$$\frac{1}{2}(m_p + m_s){v_d}^2 < \frac{1}{2}m_p{v_p}^2 + \frac{1}{2}m_s{v_s}^2$$

Since $v_r > v_s > v_p$ if recombination is to occur, then

$$\frac{1}{2}(m_p + m_s){v_d}^2 < \frac{1}{2}m_p{v_r}^2 + \frac{1}{2}m_s{v_r}^2 = \frac{1}{2}(m_p + m_s){v_r}^2$$

Thus,

$$v_d < v_r \approx a v_{ca} \tag{11}$$

This result indicates that for DOD generator, the speed of the single drop resulting from the combination of a satellite and the primary drop has an upper value, which is proportional to the capillary speed, $v_{ca} = \left(\frac{\gamma}{\rho R_{noz}}\right)^{1/2}$. The value of the proportionality coefficient for the liquids in our experiments ranges from 2.8 to 3.5. Note that Keller's theory suggests, when retreating speed is constant as in our experiments, a linear relationship between the retreating speed and capillary speed (see equation 7)

4.6 Criteria for Satellite(s) Control

Satellites are undesirable for most applications of DOD drop generators because they increase the difficulty of precise deposition, particularly on a moving substrate. Thus, the avoidance of satellites for DOD generation is of importance in applications. Two cases when a single drop is produced are:

1) The liquid thread ejected from the nozzle breaks up, and then the satellite and primary drop recombine to form a single drop. A necessary condition for this to occur is given in equation (10) (See Section E for a discussion of this case); and

2) The liquid thread ejected from the nozzle contracts into a single drop without breaking up.

The second case is discussed here. The liquid thread ejected from the nozzle will contract into a single drop without breaking up if the length of liquid thread at pinch-off, l_b, does not exceed a limiting value l_b^*. If the liquid thread contracts into a drop (with a radius of r_d) before a second breakup occurs, then

$$l_b - 2r_d \le (t_{b2} - t_{b1})(v_r - v_{b2})$$

Since $t_{b2} - t_{b1} = (C_2 - C_1)\dfrac{t_{ca}}{\alpha_{\max}^*}$ and $v_r = a v_{ca}$ (see equation 8), then

$$l_b - 2r_d \le (C_2 - C_1)\cdot a \cdot \frac{t_{ca} v_{ca}}{\alpha_{\max}^*}(1 - \frac{v_{b2}}{v_r}) = (C_2 - C_1)\cdot a \cdot \frac{R_{noz}}{\alpha_{\max}^*}(1 - \frac{v_{b2}}{v_r})$$

Replacing r_d with R_{noz} (since $r_d \approx R_{noz}$, as can be seen in Table 4-5) and rearranging gives

$$\frac{l_b}{R_{noz}} < (C_2 - C_1)\cdot a \cdot \frac{1}{\alpha_{\max}^*}\cdot(1 - \frac{v_{b2}}{v_r}) + 2 < (C_2 - C_1)\cdot a \cdot \frac{1}{\alpha_{\max}^*} + 2 \qquad (12)$$

So the limit of the thread length for the single drop generation is

$$\frac{l_b}{R_{noz}} < \zeta \frac{1}{\alpha_{\max}^*} + 2 = \frac{l_b^*}{R_{noz}} \qquad (13)$$

where $\zeta = (C_2 - C_1)\cdot a$ and varies from 0.9 to 1.1 for our experiments. This prediction has a good agreement with our experimental results (see Table 4-6). The simulation results of Notz and Basaran [57] showed that the critical value of the initial aspect ratio for liquid thread breakup increased with the value of Oh.

From equation 12, the pinch-off length without the breakup is limited by C_1, C_2, and $\alpha_{\max}^*$ ($\alpha_{\max}^*$ is related to the liquid properties and the nozzle radius alone). Our experimental data indicate that C_1 depends significantly on the signal waveform. When results for the double-peak waveform (Figure 4-1) are compared with those for the single-peak waveform with the same voltage amplitude of 21.6 V (see Figure 4-11), the first breakup time is about 40 us, much longer than the 28 μs observed for double-peak waveform. However, C_2 does not appear to be strongly influenced by the waveform for

Table 4-6: Normalized maximum pinch-off length compared with prediction value using Eq. 13.

Liquid	Voltage (volt)	l_b^* (μm)	l_b^*/R_{noz}	
			Experimental	Predicted value from Eq. (13), $\zeta = 1$
Water	18.6	119	4.5	5.0
GW	19.6	129	4.9	5.5
GWI	19.6	148	5.6	5.8

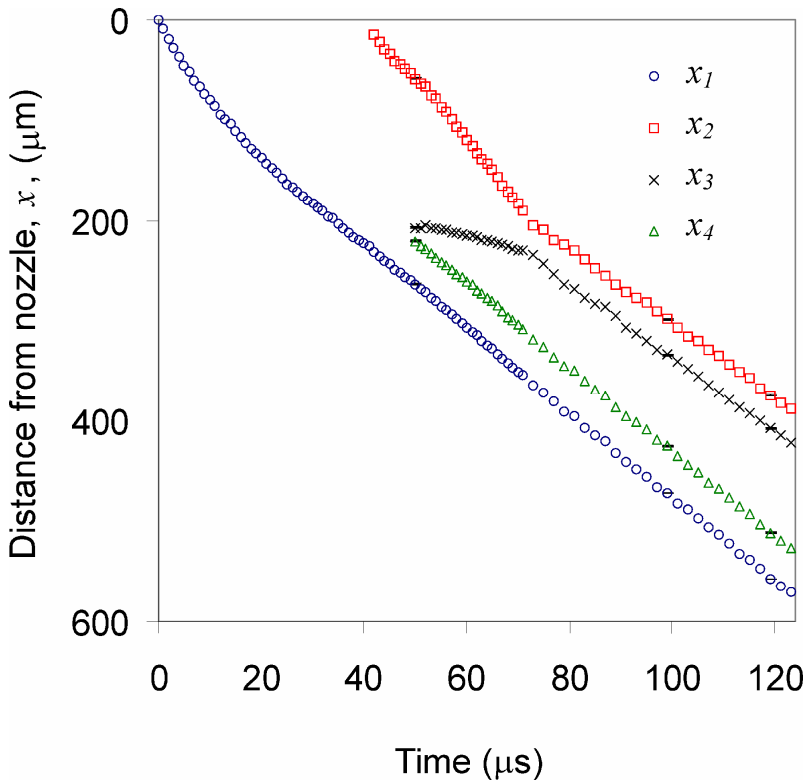

Figure 4-11: DOD drop formation curves for GW using the single-peak waveform with voltage amplitude = 21.6 V and frequency = 20 Hz. The primary drop and satellite do not merge.

our conditions since the second breakup time is 50 μs for the single-waveform and 48 μs for double-peak waveform. An optimum signal waveform should be designed to obtain a shorter t_{b1}, and correspondingly lower value of C_1. As a result, the maximum value of l_b will be larger.

For most applications, assuming the waveform is not a user input, liquid properties are easier than other system parameters to adjust for a DOD drop generator. In equation (12), the only parameter related with liquid properties is $\alpha_{\max}^*$, the grow rate of the most unstable disturbances, which is a function of Oh as shown in Equation (3). The relationship between $\alpha_{\max}^*$ and the surface tension/viscosity of liquids is shown in Figure 4-12. The value of $\alpha_{\max}^*$ decreases with liquid viscosity. For a low viscosity liquid (1 cp)

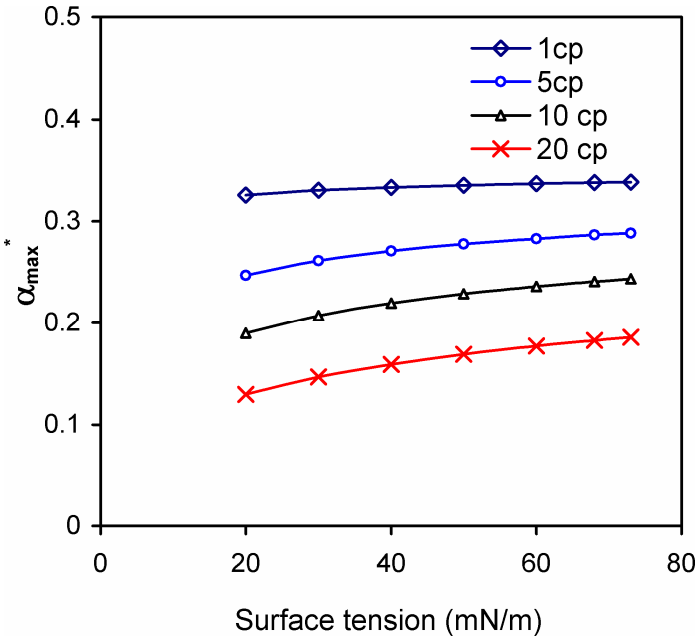

Figure 4-12: $\alpha_{\max}^*$ vs. surface tension for several viscosities, assuming a density of 1.0 g/cm^3 and nozzle diameter of 53 μm.

the surface tension has little influence on $\alpha_{\max}^{*}$, while for higher viscosity liquid (20 cP), $\alpha_{\max}^{*}$ increases with surface tension, especially at lower surface tension. According to Equation 12, longer liquid threads without breakup can be achieved by increasing liquid viscosity and decreasing surface tension. Since the range over which viscosity can be varied is much wider than the range for surface tension, more significant effects on l_b^{*} are achievable by changing liquid viscosity.

4.7 Effects of Waveform on DOD Drop Formation

Sequences of images during DOD drop formation for the four driving signals (1-4) described in Table 3-1 are shown in Figure 4-1 and 4-13 (a-c) respectively. Although the voltage amplitudes of the four driving signals are the same, waveform differences lead to four distinct drop formation processes.

Let us first discuss the differences in drop formation for signals 1 and 2. Signal 1 has a double-peak waveform while signal 2 has a single-peak waveform. The single-peak waveform is identical with the double-peak signal with the smaller pulse omitted. From Figure 4-1 and 4-13-(a), it can be seen that the smaller pulse in signal 1 initiates an early pinch-off of liquid from the nozzle exit at 28 μs. Without the smaller pulse, the pinch-off of the liquid is delayed to 42 μs. The corresponding liquid pinch-off length increases from 148.3 to 231.5 μm. This is caused by the smaller pulse producing a negative pressure (suction) within the nozzle, which promotes the stretching and necking of the liquid thread. Moreover, under the action of the smaller pulse, the pinch-off of liquid from the nozzle exit is more uniform, with less influence from the nozzle plate. The liquid thread near the nozzle is almost straight for waveforms containing the second peak, but deviates sideways for the single-peak waveform (see Figure 4-13-(b), from 33 μs to 42 μs). However, the negative pressure resulting from the smaller pulse reduces the

kinetic energy and volume of the ejected liquid generated by the first larger pulse. Hence, the double-peak waveform generates a smaller primary drop and satellite with lower speed (see Table 4-7). Another difference is that with the double-peak waveform the primary drop and satellite merge after 15 μs, but for the single-peak waveform, the primary drop and satellite do not recombine.

Next signals 1 and 3 are compared. Both of the signals are double-peak waveforms, but the rising time, T_1, is 10.6 μs for signal 1 and is 14.4 μs for signal 3. Changing T_1 affects the DOD drop formation as can be seen in Figure 4-1 and 4-13 (c). Increasing T_1 cause the liquid thread length at pinch-off to increase from 148.3 to 210.3 μm, the primary drop and satellite to become larger, and the speed of the primary drop to increase. T_1 corresponds to the time over which the piezo transducer contracts causing the ink chamber to enlarge which draws in ink. If T_1 is too small, the system does not have enough time to respond and insufficient ink is sucked into the chamber. On the other hand, if T_1 is too large, air may be sucked into the nozzle and cause jettability problems. Therefore, an appropriate rising time, which depends on not only the geometry and material of printhead, but also the liquid properties such as viscosity, is required.

Figure 4-1 and 4-13 (c) show the differences of drop formation process between signals 1 and 4. Both of the signals are double-peak waveforms, but the falling time, T_2, is 2.6 μs for signal 1 and 5.0 μs for signal 4. Increasing T_2 result in a longer pinch-off length and a larger primary drop having a higher speed. For signals 1 and 4, the primary drop and satellite merge, but for signal 4, recombination of the primary drop and satellite takes about 150 μs, much longer than 12 μs for signal 1. It is believed that the amplitude of the pressure wave in the nozzle is related to T_2 [14]. The shorter falling time for signal 1 generates higher amplitude of the pressure wave. Experimental results show that 5-μs falling time leads to a higher final drop speed of 4.0 m/s versus 3.4 m/s for a falling time of 2.6 μs, which would seem to be counter to the argument of increasing peak magnitude

pressure pulse with the shorter pulse. However, it is the time-integrated pressure pulse which is related to the momentum imparted to the drop and hence the longer pulse may lead to larger speeds for this reason. Since the rising times and voltage amplitudes of the two signals are identical, the same amount of liquid should have been sucked into the chamber from the ink reservoir, and, it might be expected that the ejected volumes for the two signals to be identical. However, the 5-μs falling time leads to an ejected liquid volume 22.3% greater than ejected liquid volume for the 2.6-μs falling time.

Seemingly slight variations in driving signal waveform may result in significant change in the DOD drop formation. It is expected that the DOD drop formation process will be influenced greatly by the amplitude of the major pulse of driving signal, ratio of amplitudes of major pulse and smaller pulse, as well as liquid properties such as surface tension, viscosity and additives, and the geometry of printhead (chamber and nozzle).

Table 4-7: Effect of four waveforms on DOD drop formation.

Signal	Time of pinch-off from nozzle (μs)	Length of liquid thread at pinch- off from nozzle (μm)	Velocity of primary or final drop (m/s)	Diameter of primary drop size± 1 standard deviation (μm)	Diameter of satellites ± 1 standard deviation (μm)	Recombi-nation of primary drop and satellites
1	28	148.3	3.4	42.6±0.3	26.3±0.4	yes
2	42	231.5	4.1	45.1±0.4	33.0±0.4	no
3	30	210.3	5.0	45.6±0.3	36.6±0.3	no
4	28	171.0	4.0	44.9±0.3	31.8±0.3	yes

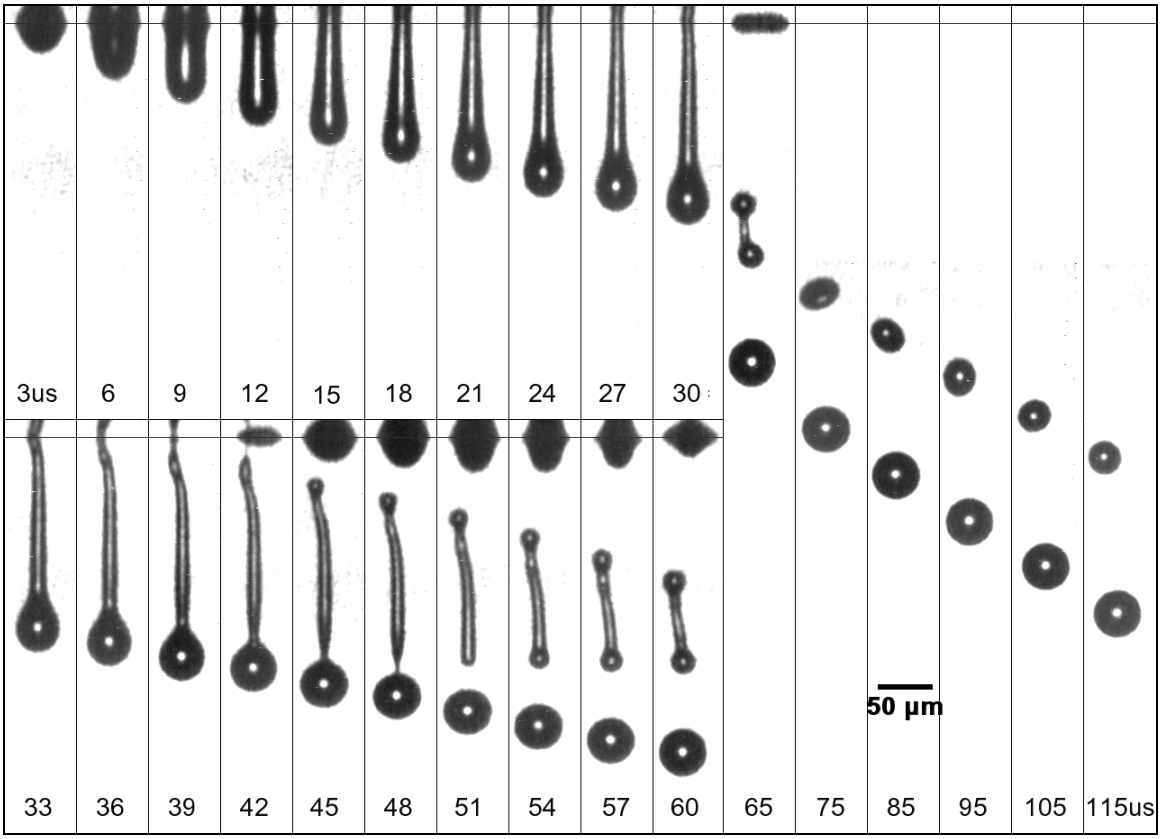

(a)

Figure 4-13: Sequential images of DOD drop formation under four signal waveforms (see Table 3-1), (a) signal 2, (b) signal 3, and (c) signal 4, and signal 1 is shown in Figure 4-1; the number at the bottom of each frame indicates time (µs). Waveform parameters are provided in Table 3-1. Mixture of glycerin and water (48:52), viscosity = 5.0 cP, surface tension = 68 mN/m.

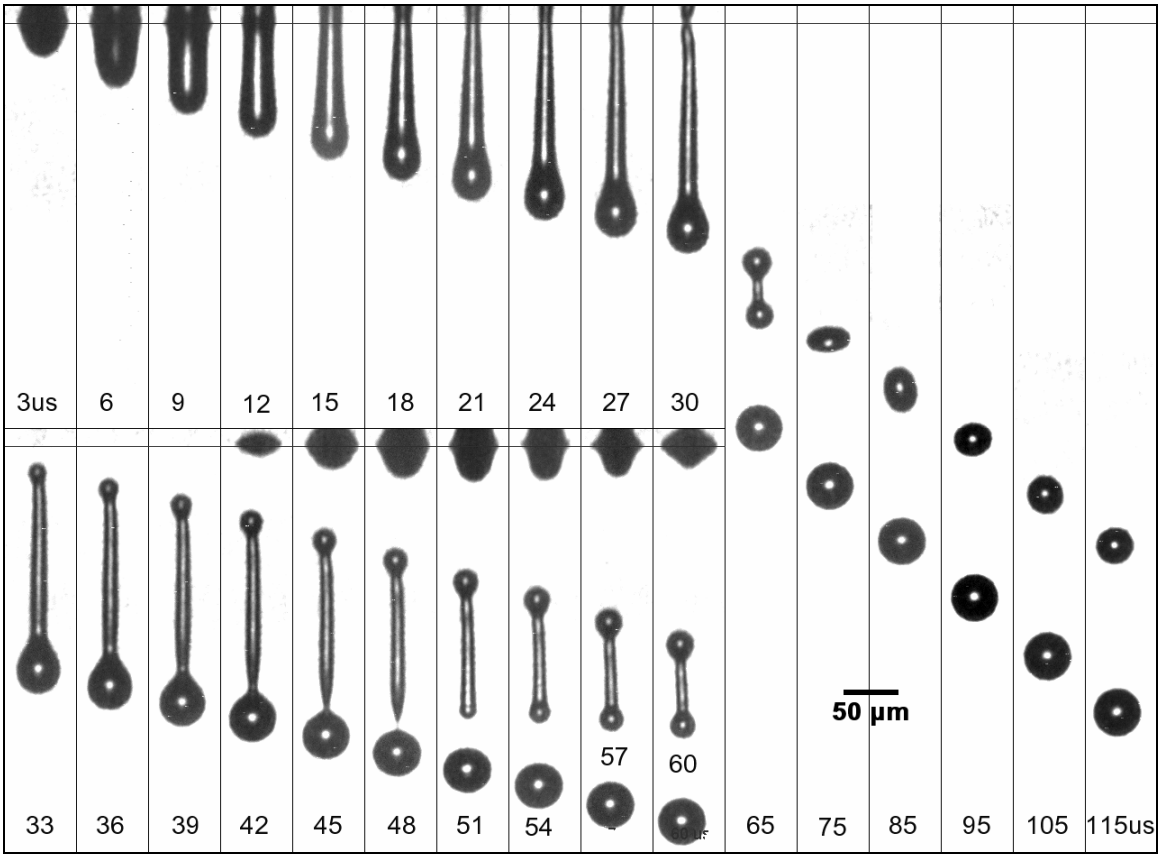

(b)

Figure 4-13: Sequential images of DOD drop formation under four signal waveforms (see Table 3-1), (a) signal 2, (b) signal 3, and (c) signal 4, and signal 1 is shown in Figure 4-1; the number at the bottom of each frame indicates time (µs). Waveform parameters are provided in Table 3-1. Mixture of glycerin and water (48:52), viscosity = 5.0 cP, surface tension = 68 mN/m.

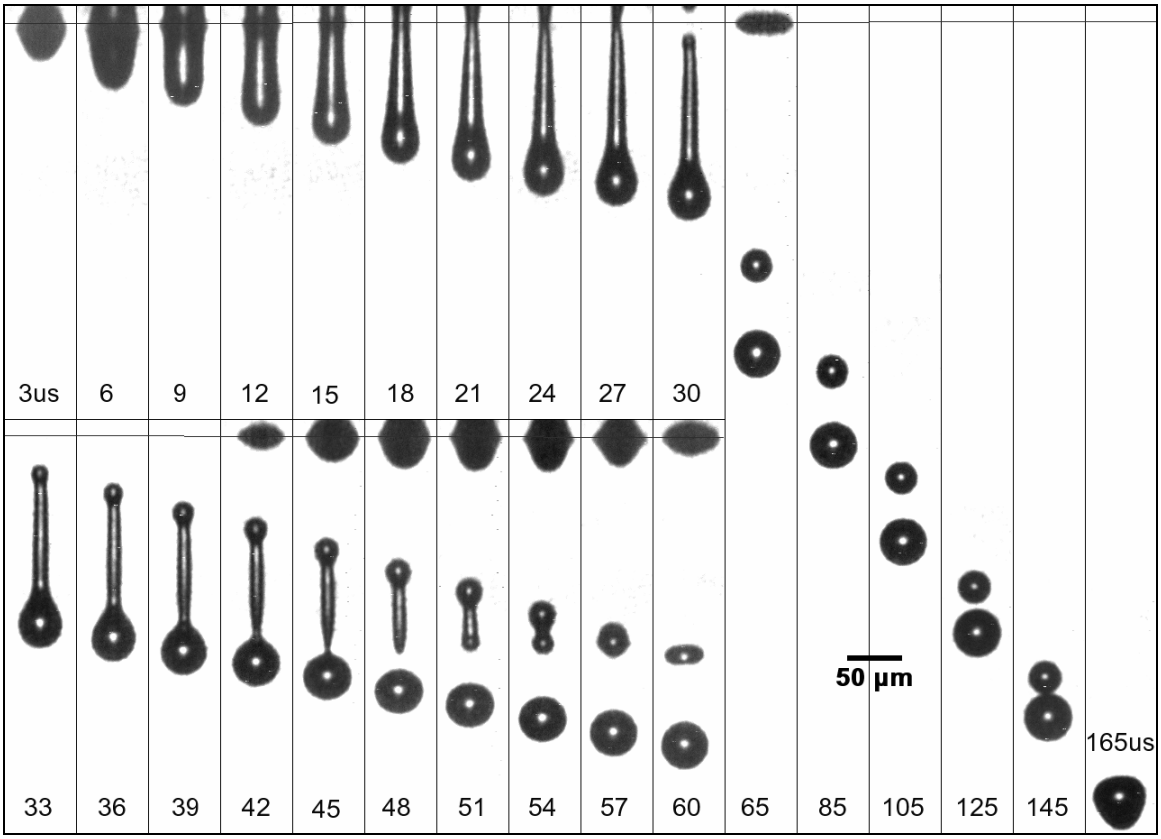

(c)

Figure 4-13: Sequential images of DOD drop formation under four signal waveforms (see Table 3-1), (a) signal 2, (b) signal 3, and (c) signal 4, and signal 1 is shown in Figure 4-1; the number at the bottom of each frame indicates time (µs). Waveform parameters are provided in Table 3-1. Mixture of glycerin and water (48:52), viscosity = 5.0 cP, surface tension = 68 mN/m.

CHAPTER 5

MICRON-DROP IMPACTION ON SUBSTRATES

In this chapter, the experimental results and discussion of micron-drop impaction are presented first. Then, the results for micron-drop impaction are compared with those for millimeter-drop impaction. Finally, the scalability of the impaction process from millimeter drops to micron drops is discussed.

5.1 Evolution of Micron-Drop Impaction on Substrates

The sequential images of water drop impaction for three different impact speeds (2.21, 4.36, and 12.2 m/s), with corresponding $1 < We < 100$ and $100 < Re < 1000$, on five surfaces (contact angles of 6°, 31°, 67°, 88°, and 107°) are shown in Figures 5-1, 5-2 and 5-3. The variation of dimensionless diameter or spreading ratio ($D^* = D_S/D_0$) and dimensionless height ($H^* = H_s/D_0$) with time are plotted in Figures 5-4, 5-5 and 5-6. Although the same drop generator is used, drop size varies from 40.9 to 50.5 μm under different driving voltage amplitudes required to produce the three drop speeds, as discussed in Chapter 4. At drop speed of 2.21 m/s, a single drop is generated for each driving pulse. Since no satellite is generated, the impaction process can be observed for time up to approximately 13,000 μs. For longer times, the errors in the delay times produced by the delay generator are larger than camera exposure time (1 μs in most cases), and the camera and laser are no longer synchronized. However, the observation time is sufficient to record the entire impaction process. At drop speeds of 4.36 and 12.2 m/s, satellites are produced; thus, observation times from primary drop impaction until the first satellite reaches the substrates are limited to 800 μs and 120 μs, respectively. However, the times are sufficient to observe the main stages of the micron-drop impaction.

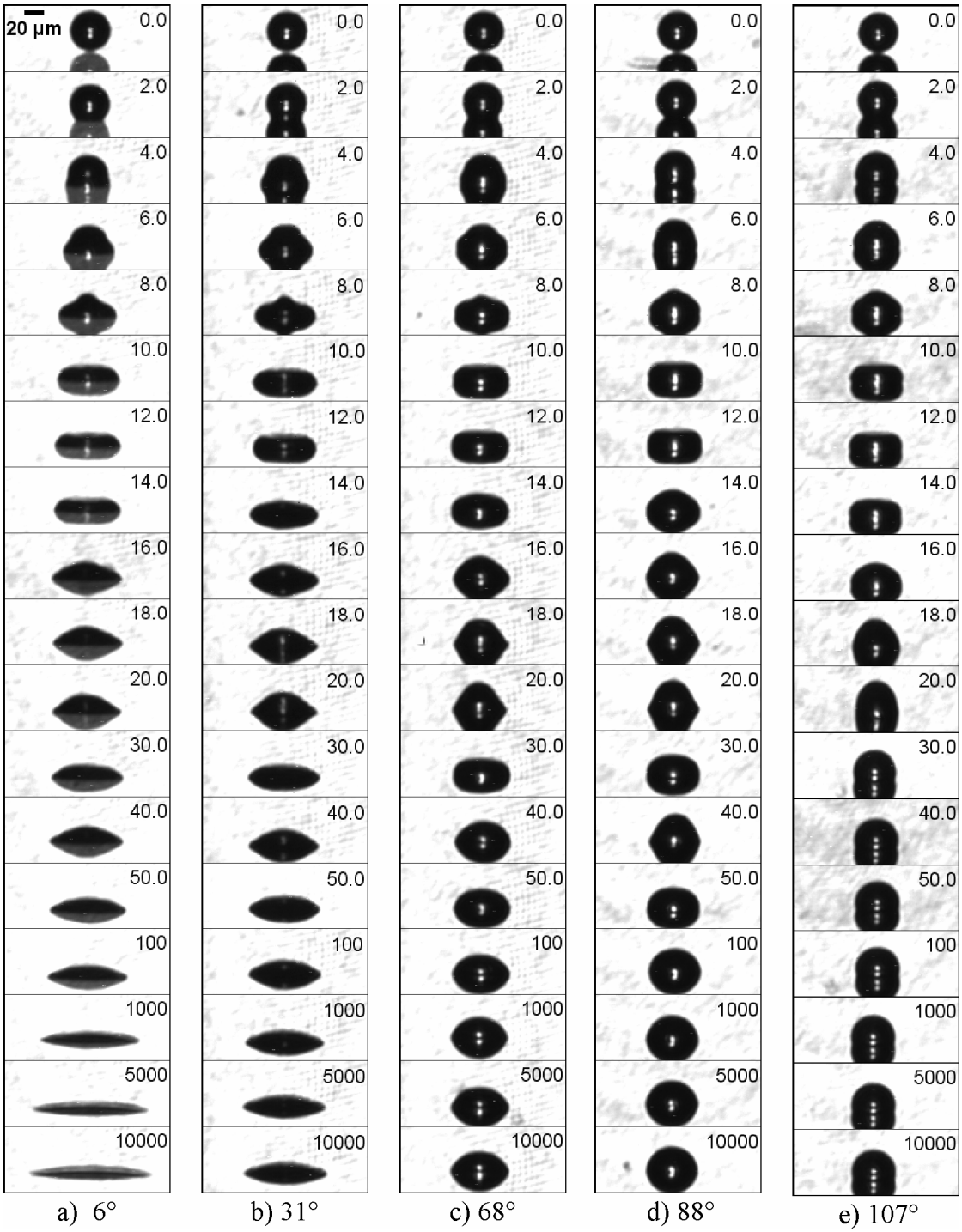

Figure 5-1: Sequence of images for drop impaction on five substrates: impact speed = 2.21 m/s, drop diameter = 40.9 µm.

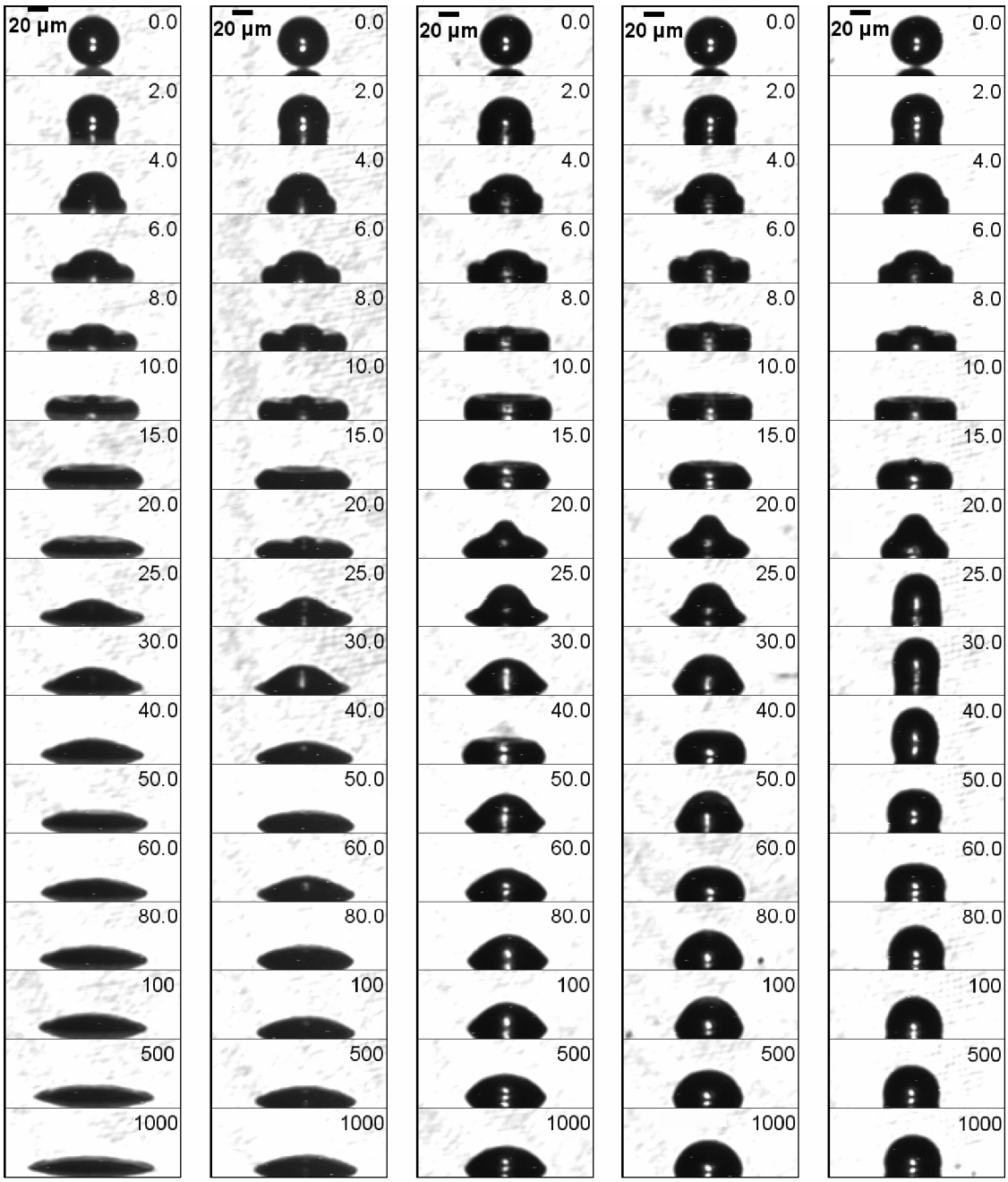

Figure 5-2: Sequence of images for drop impaction on five substrates: impact speed = 4.36 m/s, drop diameter = 48.8 µm.

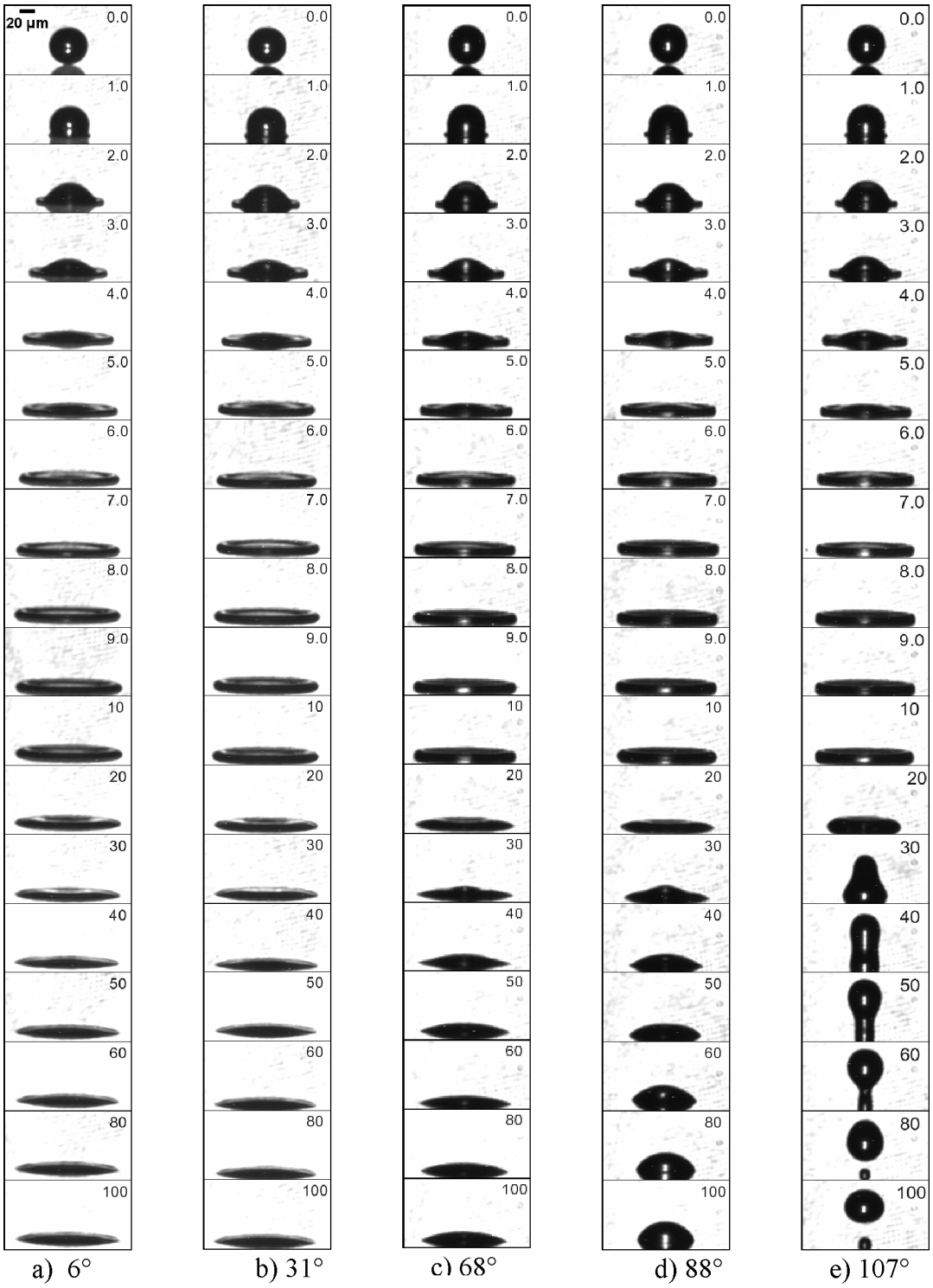

Figure 5-3: Sequence of images for drop impaction on five substrates: impact speed =12.2 m/s, drop diameter = 50.6 µm.

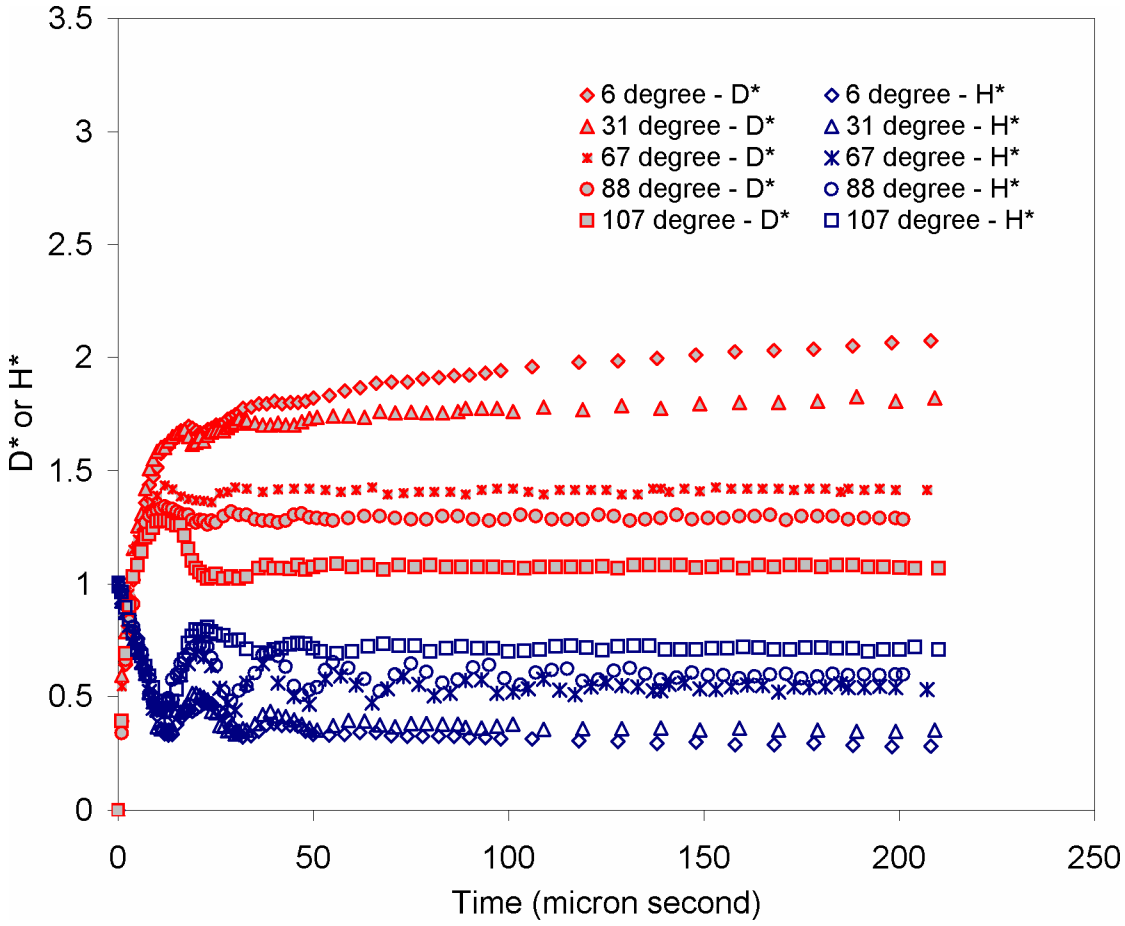

Figure 5-4: Variation of spreading ratio, D^*, and dimensionless drop height, H^*, on five substrates with time: U_0 = 2.21 m/s, D_0 = 40.9 μm, We = 2.77, Oh = 0.0165.

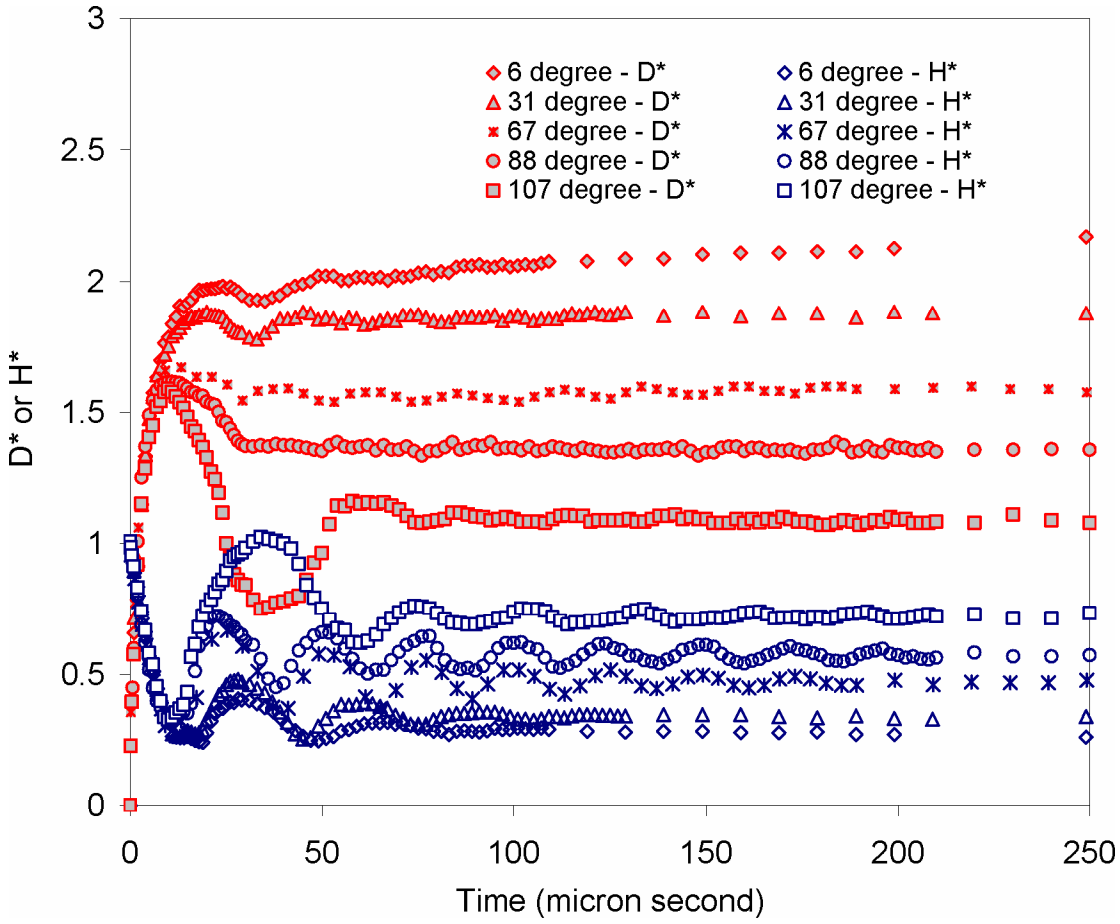

Figure 5-5: Variation of spreading ratio, D^*, and dimensionless drop height, H^*, on five substrates with time: U_0 = 4.36 m/s, D_0 = 48.8 μm, We = 12.8, Oh = 0.0151.

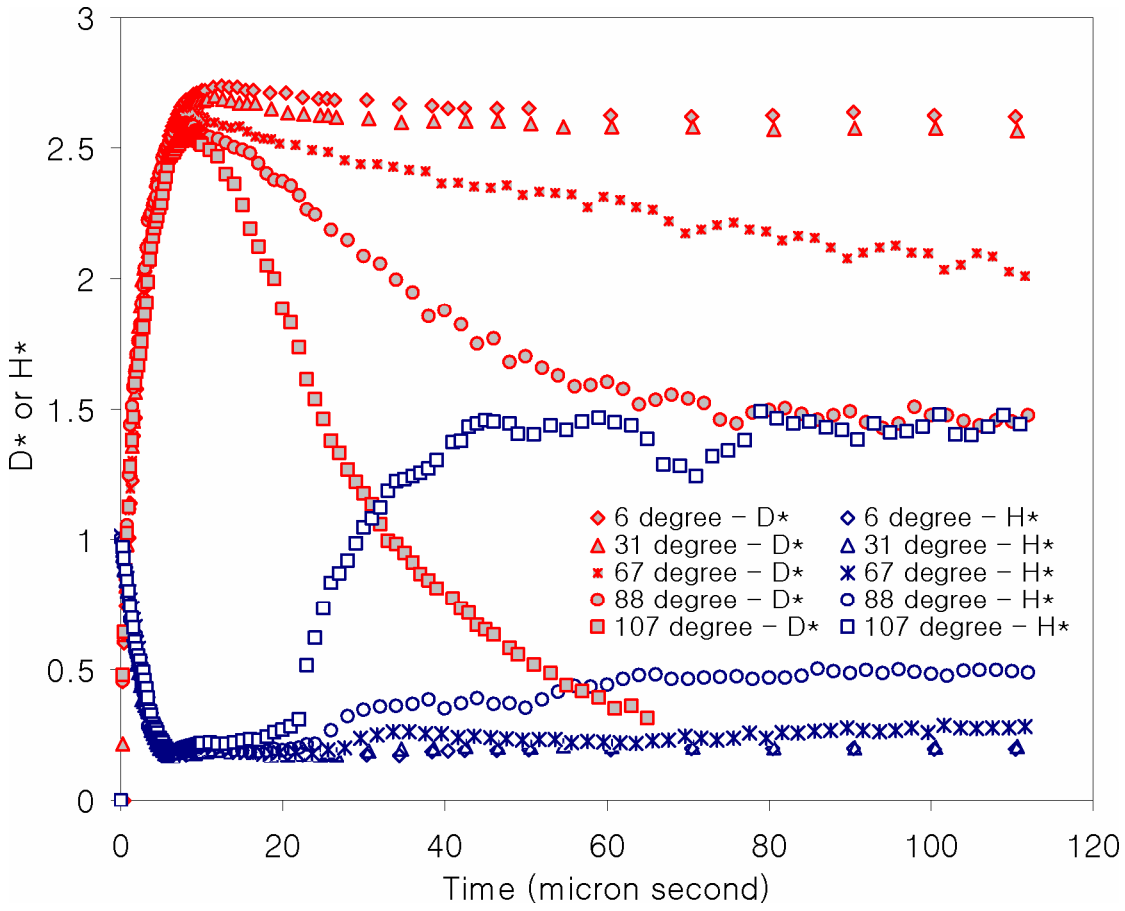

Figure 5-6: Variation of spreading ratio, D*, and dimensionless drop height, H*, on five substrates with time: U_0 = 12.2 m/s, D_0 = 50.5 μm, We = 103, Oh = 0.0148.

When the micron drop contacts the substrate, the contact area of the drop rapidly moves outward, with a drop shape initially resembling a truncated sphere. As the liquid continues to move radially outward, a nearly flat layer is formed with a shape dependent on both impact speed and substrate. For higher impact speed and/or lower contact angle surfaces, the layer spreads faster and further and is thinner at maximum spreading. The layer remains at maximum spreading for a short time, causing a flattening in the impaction curves (see Figures 5-4 – 5-6). The whole spreading stage lasts O (10) μs for the present study. Then the drop retracts under the action of surface tension at the contact line formed by the free surface of layer and substrate. The height of the liquid layer rises gradually, and the contact area of the layer on the substrate contracts. The extent of retraction depends on the impact velocity as well as the wettability of the substrate. On the hydrophobic surface with a contact angle of 107°, the extent of retraction increases with impact speed. Under an impact speed of 12.2 m/s, the drop recedes strongly and most of the drop separates for the substrate, which is referred to as rebounding. For hydrophilic surfaces, retraction becomes weaker as contact angle decreases, especially at impact speed of 12.2 m/s (see Figure 5-3). On the low-contact angle surfaces, after impaction, the drop spreads rapidly to a local maximum spreading ratio, pauses and insignificantly retracts, and then begins to spread again. Drop oscillation occurs until surplus energy is dissipated, and final equilibrium is reached.

5.2 Drop Spreading on Substrates

Four important factors in drop spreading on a surface are gravity, surface wettability, kinetic energy and viscous dissipation. The relative significance of these four factors can be expressed using the following dimensionless numbers: 1) Weber number (We), the ratio of kinetic energy to surface energy; 2) Reynolds number (Re), the ratio of inertial to viscous forces; 3) Froude number ($Fr = U_0^2/(r_0 g)$), the ratio of kinetic energy to gravitational potential; and 4) cosθ, where θ is the contact angle of drop on the substrate. Without consideration of initial kinetic energy, it has been shown by theoretical analyses for gravity-driven and wettability-driven spreading that $d(t) \sim t^{1/8}$ [53] and $d(t) \sim t^{1/10}$ [20, 83], respectively, where $d(t)$ is the diameter of the spreading drop base and t is the time. If the drop impacts the substrate with a finite speed, the initial spreading is greatly affected by kinetic energy, and $d(t) \sim t^{1/2}$ [8]. Theoretical analyses have been made to predict the spreading process initially dominated by kinetic energy [36, 44].

For present experimental results, as shown in Figures 5-4, 5-5 and 5-6, the spreading curves are very similar for the five substrates during initial spreading (first several micron seconds), indicating that kinetic energy of the drop is dominating during this stage. As the drop spreads and kinetic energy of the drop is dissipated or converted into the surface energy due to the increase in surface area of the spreading drop, liquid-substrate interaction becomes more important, and the spreading curves for the various substrates separate. For decreasing equilibrium contact angle, the drop spreads further over a longer period of time.

5.2.1 Maximum Spreading Ratio, D^*_{max}

Maximum spreading ratio (D^*_{max}) is an important parameter in DOD inkjet printing because it significantly affects the dot size left by the inkjet drop on a substrate after evaporation [3]. Several models [32, 54, 61, 62, 73], based on experimental results

of millimeter-drop impaction, have been built to predict D^*_{max}. The only model based on micron-size inkjet drops was constructed by Asai et al., 1993, [3]; however, the model does not include the effect of contact angle. In Table 5-1, the present experimental results are compared with predictions from six models. The model predictions show reasonable agreements with the experimental results for micron-scale drops, but with slight over-prediction for most cases. Here, the experimental results of D^*_{max} for surfaces with low contact angle (6 and 31°) are the first peak in the D^* versus time curves although, after a short pause, the drop continues to spread to a higher D^*. The subsequent spreading is driven by the wettability of the surface, and is independent on the initial kinetic energy.

The results given in Table 5-1 are plotted in Figures 5-7 a-c. At We = 103, all model predictions agree with the experimental values within 10%, with exceptions of the model of Fukai et al. (1998) [32], which over-predicts D^*_{max} for low-contact-angle surfaces by more than 10%. Moreover, maximum spreading ratio becomes less dependent on the equilibrium contact angle, varying from 2.54 to 2.74 for surfaces with contact angle ranging from 107 to 6°. For low-We impaction (We = 2.77 and 12.8, see Figures 5-7 a and b, respectively), most of the models provide acceptable predictions for large-contact-angle surfaces (88° and 107°). However, for low-contact-angle surfaces, the difference between model predictions and experimental results are significant, for example, up to 50% for the model of Mao et al. (1997) [54] when We = 2.77 and θ = 6°. In contrast, predictions of the model of Park et al. (2003) [61] agree with the experimental results with deviation less than 10% for both low- and high-We impactions. This model considers energy dissipated during spontaneously spreading, which leads to lower predictions for low-contact-angle surfaces than those of other models. This

Table 5-1: Comparison of D^*_{max} for present experiments with predictions of six models.

Re	We	Contact angle (degrees)	D^*_{max}						
			Experimental results	Predictions					
				Park et al. (2003) [61]	Fukai et al. (1998) [32]	Mao et al. (1997) [54]	Pasandideh-Fard et al. (1996) [62]	Scheller et al. (1995) [73]	Asai et al. (1993) [3]
100.9	2.77	6	1.69	1.73	3.32	3.15	3.63	1.43	1.40
		31	1.68	1.60	2.79	2.68	3.11	1.43	1.40
		67	1.44	1.59	1.80	1.85	2.25	1.43	1.40
		88	1.34	1.50	1.46	1.52	1.92	1.43	1.40
		107	1.28	1.40	1.28	1.30	1.72	1.43	1.40
238	12.8	6	1.98	1.86	3.06	2.57	2.73	1.87	1.75
		31	1.88	1.96	2.8	2.41	2.58	1.87	1.75
		67	1.68	1.90	2.13	2.02	2.2	1.87	1.75
		88	1.62	1.82	1.81	1.82	1.99	1.87	1.75
		107	1.57	1.72	1.60	1.67	1.86	1.87	1.75
689	102.9	6	2.74	2.57	3.28	2.94	2.70	2.65	2.73
		31	2.7	2.57	3.21	2.89	2.67	2.65	2.73
		67	2.64	2.51	2.98	2.75	2.56	2.65	2.73
		88	2.6	2.46	2.82	2.66	2.49	2.65	2.73
		107	2.54	2.41	2.68	2.58	2.43	2.65	2.73

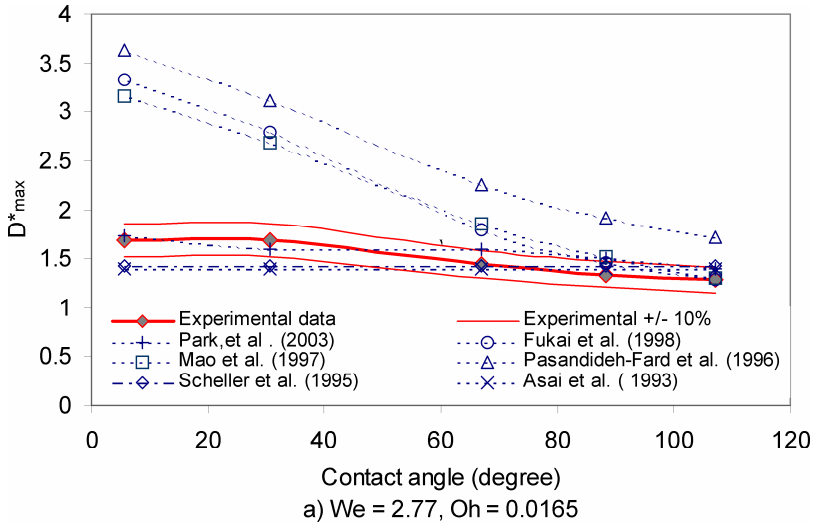

a) We = 2.77, Oh = 0.0165

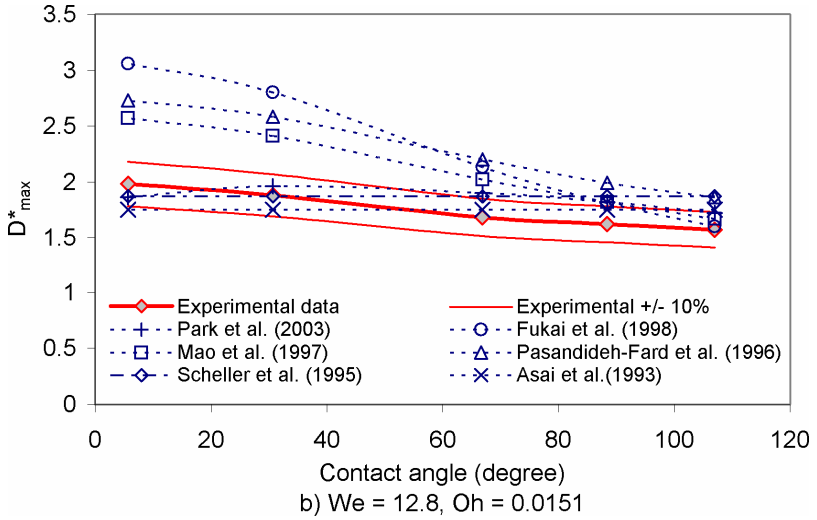

b) We = 12.8, Oh = 0.0151

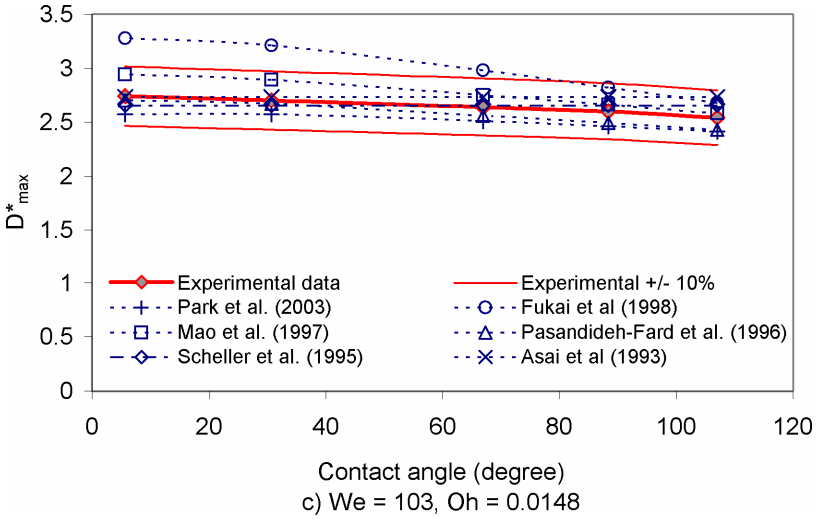

c) We = 103, Oh = 0.0148

Figure 5-7: Comparison of experimental results with predictions of six models.

demonstrates that spontaneously spreading dissipation is important for low-We impactions, especially for low-contact-angle substrates. This can be seen in Figure 5-8 where spontaneous spreading dissipation is compare with kinetic energy of an impacting drop, both scaled by total surface energy of impacting drop, $\pi D_0^2 \gamma$. Dimensionless spontaneous spreading dissipation, E_{diss}, is $1-\left(2-3\cos\theta+\cos^3\theta\right)^{1/3}$ [61], and dimensionless initial kinetic energy, E_k, is *We/12*. At low We and low contact angle, the magnitudes of spontaneous energy and initial kinetic energy are of the same order of magnitude. Thus, if only viscous dissipation is considered, as in models of Mao et al. [54], Pasandideh-Fard et al. [62], and Fukai et al. [32], predictions do not agree well with experimental results.

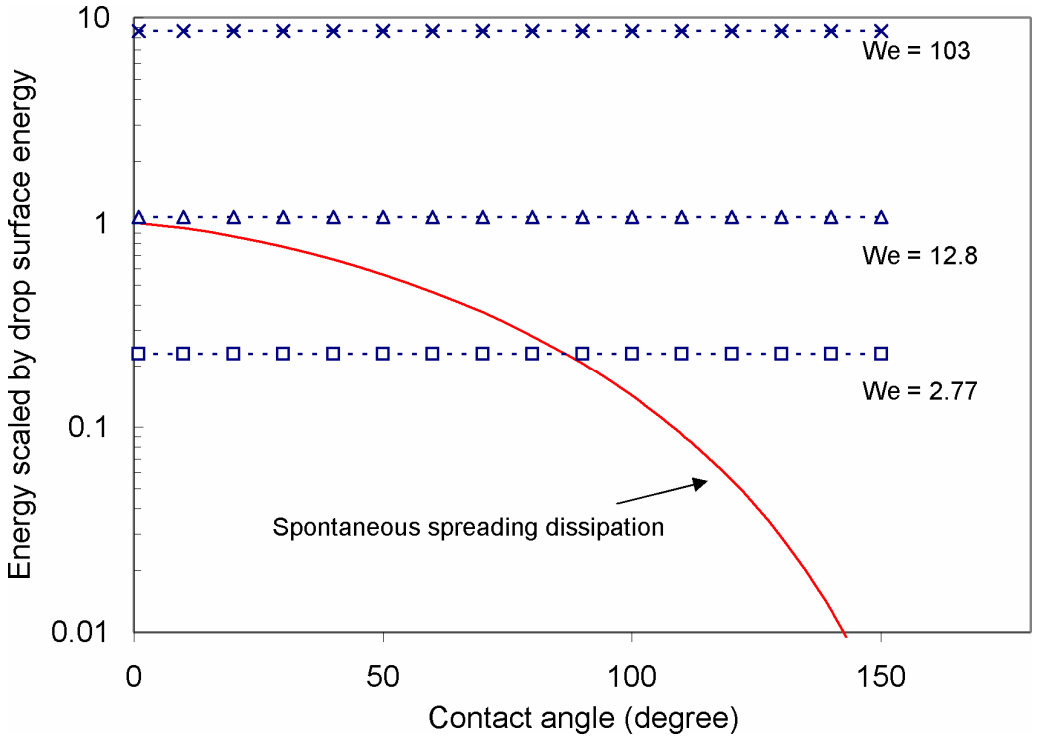

Figure 5-8: Comparison between spontaneous spreading dissipation and kinetic energy of impacting drop, scaled by total surface energy of impacting drop, $\pi D_0^2 \gamma$. The solid line is the dimensionless spontaneous dissipation, E_{diss}, and the dash line is the dimensionless initial kinetic energy, E_k = *We/12*.

Predictions of the model of Asai et al. [3] agree within 10% of the experimental results even though the model does not consider the effect of surface-liquid interactions. This can be expected because the model is a correlation of the experimental results for micron-drop impaction. The model of Scheller et al. [73] also gives a good fit for the present data. This model is based on theoretical analysis with the correlations of millimeter-drop impaction results, neglecting the effect of the equilibrium contact angle.

5.2.2 Dimensionless Time, t^*_{max}, to Reach D^*_{max}

How rapidly the drop deforms to the maximum spreading extent is an interesting topic. Spreading time not only influences the roles of such additives as polymer, particles, and surfactant in drop impaction, but also is related to the evaporation and solidification processes. The time to reach D^*_{max} is usually scaled by D_0/U_0 to obtain t^*_{max}. Chandra and Avedisian [13] assumed that $t^*_{max} = 1$. Pasandideh-Fard et al. [62] used an analytical approach to obtain that $t_{max}^* = 8/3$, and Mao et al. [54] and Park et al. [61] adopted this value in their models. Our experimental results for t_{max} and t^*_{max}, listed in Table 5-2, show a strong dependence on impact speed as well as equilibrium contact angle, and t^*_{max} increases with increasing We and/or decreasing θ. At the highest impact speed (U_0 = 12.2 m/s), t^*_{max} is about triple that at the lowest impact speed (U_0 = 2.21 m/s). From the present experiments, t^*_{max} ranged from 0.65 to 2.99; therefore, it is not acceptable to treat as a constant.

Table 5-2: Dimensionless time, t^*_{max}, oscillation time and dissipation time

Drop diameter (μm)	Impact velocity (m/s)	Contact angle (°)	t_{max} (μs)	t^*_{max} [a]	Oscillation period [b] (μs)	Dissipation time [c], (μs)
40.9	2.21	6	18	0.97	10.9	470
		31	17	0.92		
		67	13	0.70		
		88	12	0.65		
		107	12	0.65		
48.8	4.36	6	24	2.14	14.2	669
		31	20	1.79		
		67	12	1.07		
		88	11.2	1.00		
		107	10	0.89		
50.6	12.2	6	12.4	2.99	15.0	719
		31	11.6	2.80		
		67	9.4	2.27		
		88	8	1.93		
		107	8	1.93		

a. Scaled by D_0/U_0.
b. Oscillation time = $t_{ca} = (\rho r_0^3/\gamma)^{1/2}$ [74]. r_0 is the radius of drop before impaction.
c. Dissipation time = $\rho(r_0/2)^2/\mu$ [74].

5. 3 Post-Spreading Evolution of Drop on Substrate

After the drop reaches the maximum spreading position, it may retract under the action of surface tension at the contact line formed by the free surface of liquid layer and the substrate. The contact base of the drop on the substrate shrinks and the height of the layer increases. Subsequently, the drop oscillates on the substrate until the equilibrium state is reached. The extent of retraction depends on drop impact speed as well as the equilibrium contact angle of the liquid on the substrate.

5.3.1 Retraction and Rebound

After reaching D^*_{max}, retraction of drops depends on equilibrium contact angle and impact speed. For very hydrophilic substrates, such as thermally oxidized silicon wafers and glass slides, the retraction of the contact area is insignificant because the liquid layer is arrested at the contact line (see Figures (5-1) – (5-6)). As θ increases, the tendency to retract increases.

Dimensionless height ($H^* = H_s/D_0$) of the retracting drop at maximum retraction versus We number is shown in Figure 5-9. For the hydrophobic surface with θ = 107˚, the maximum retraction height, H^*_{max}, increases with We and rebounding occurs when H* exceeds a critical value. However, for hydrophilic surfaces (θ = 6, 31, 67, and 88˚), the retraction height of drop decreases with We. Moreover, from Figure 5-9, it can be seen that the H^*_{max} for 88˚ at three Weber numbers is lower than that for 107˚. As can be seen in Figure 5-2 e, at We = 12.8 a neck develops at the contact base of the drop when θ = 107˚ and at time = 30 μs; however, necking does not occur for θ = 88˚ even at We = 103 (see Figure 5-3 d). This suggests that θ plays a more important role in retraction than We.

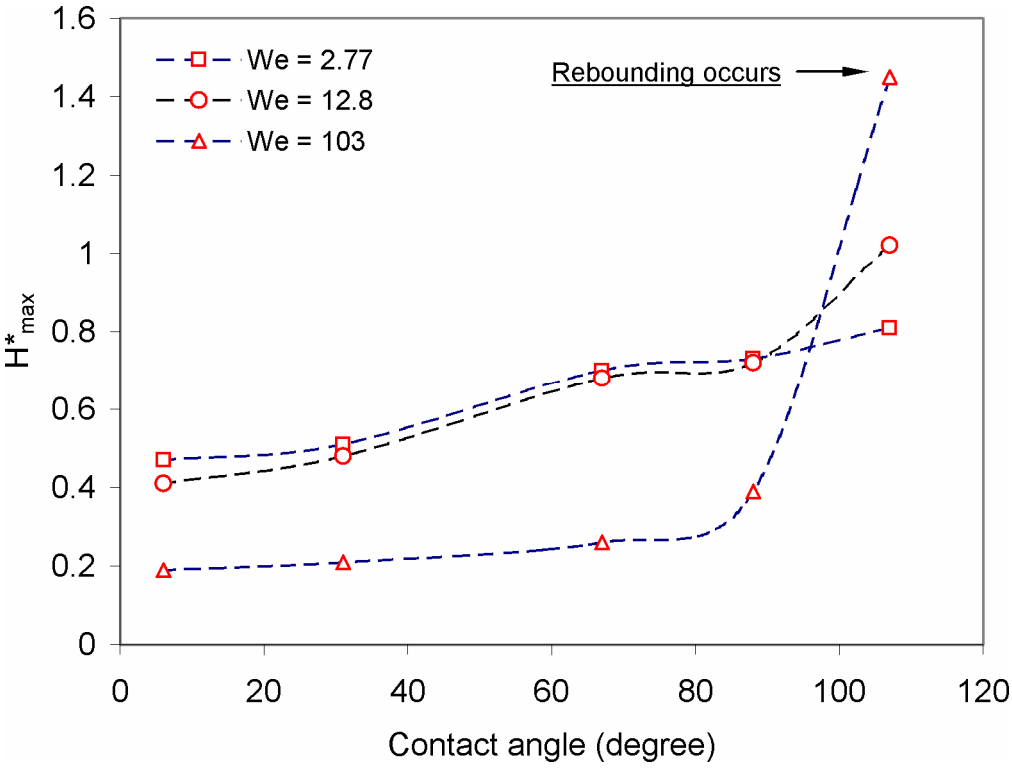

Figure 5-9: Maximum dimensionless height (H^*_{max}) during drop retraction versus θ for three Weber numbers. Note that rebounding only occurs at We = 103 and θ = 107º.

In the present experiments for θ = 107°, rebounding occurs for impact speeds of 10.6 and 12.2 m/s, but not for impact speeds of 2.21 and 4.36 m/s. According to the rebounding model of Mao et al. [54], when excess rebound energy $E^*_{ERE} > 0$, rebounding occurs. The values of E^*_{ERE} are 0.082 and 0.142 for impact speeds of 10.6 and 12.2 m/s, respectively. Thus, the model correctly predicts rebounding for both cases. For θ = 88° and U_0 = 12.2 m/s, $E^*_{ERE} = -0.17 < 0$, suggesting no rebounding occurs, which agrees with our experimental result. However, for a drop speed of 12.2 m/s and a contact angle of 98°, no rebounding is observed experimentally; however, E^*_{ERE} is about 0.008, indicating the occurrence of rebounding. Thus, the rebounding model of Mao et al.

agrees well with our micron-drop impaction experiments, but it should be used carefully for $E^*_{ERE} \sim 0$.

5.3.2 Relaxation to Equilibrium State

Before a drop reaches its equilibrium state on a substrate, it goes through a relaxation process (oscillates, dissipating surplus energy). The relaxation process is determined by D^*_{max} since excess surface energy increases with D^*_{max}. Three kinds of oscillatory behaviors are observed in the present experiments as the drop relaxes to its equilibrium position. First, the drop overshoots its equilibrium position during the spreading stage, and then the contact base of the drop retracts and oscillates around its equilibrium position. This mode can be seen in Figures 5-4 and 5-5 for θ = 67, 88, and 107˚. For the second type, the drop overshoots its equilibrium position greatly, and then oscillations in D* and H^* are observed as the drop retracts toward its equilibrium position, as shown in Figure 5-6 for θ = 67 and 88°. For the third type, the drop undershoots its equilibrium position. After a short pause, the drop starts to spread again and continues to spread to a higher D^*. Oscillations in D* and H^* are observed as the drop spreads, as shown in Figures 5-4 and 5-5 for θ = 6 and 31˚.

The mechanisms for spreading, retracting and oscillating are different. Dimensionless spreading and retracting are related to We, Oh and θ; the period of oscillation is scaled by the drop capillary time, $(\rho D_0^3 \gamma)^{1/2}$; and dissipation time is scaled by $\rho(D_0/2)^2/\mu$ (see table 5-2) [74]. The dissipation time is much longer than the period of oscillation. In present experiments, the oscillation processes are completed in about 500 μs for most cases, but the spreading may continue.

The spreading ratio at the equilibrium drop position, D^*_e, can be estimated from the equation of Ford and Furmidge [28], which is based on the equilibrium contact angle for a drop placed at zero speed on the surface. The spreading ratio at the observed final drop position, D^*_f, on the substrate may be different from D^*_e, depending on the drop's relaxation history. In Table 5-3, D^*_f for different initial conditions and substrates are compared with D^*_e.

Due to the limitations of observation time (about 120 μs), the equilibrium position for We = 103 may not be reached. For low contact angle surfaces (θ = 6 and 31˚), spreading was extremely slow and may not have terminated even after 10,000 μs where We = 2.77. However, for We = 2.77 and 12.8 on the surface with θ = 67, 88 and 107˚, the slope of the D^* curve appears to be zero at last observation time (see Figures 5-4, 5-5 and 5-6), and the drop appears to be at the equilibrium position, but different from D^*_e. For θ = 67 and 88˚, D^*_f increases with We number; and for θ = 107˚, D^*_f is close to D^*_e.

Continuous spreading occurs for low θ (6 and 31˚) and We = 2.77 and 12.8, as shown in Figure 5-10. Assuming that the relationship between D^* and dimensionless time t (scaled by capillary time, $t_{ca} = (\rho D_0^3 \gamma)^{1/2}$), has the form $D^* = g\, t^n$ [2], where g and n are constants, the data were fitted by a power regression equation. Here, the constant *n* depends on the wettability of surfaces and is in the range of 0.7 – 0.9 and 0.2 – 0.3 for glass slide and SiO_2 wafer, respectively. For a given We, the values of g are almost identical for glass slide and SiO_2 wafer. Note that D^*_{max} for We = 2.77 and 12.8 are almost identical in the present experimental results (see Table 5-1), suggesting that g may be scaled by D^*_{max}. Continuous spreading on the substrate with low θ (6 and 31˚) does not occur for We = 103. The slope of the plot of D^* versus time appears to be zero at the

Table 5-3: D^*_m, D^*_f and D^*_e for micron drops impacting various substrates.

Drop diameter (μm)	Impact velocity (m/s)	We	Contact angle (°)	D^*_m	D^*_f [a]	D^*_e [b]
40.9	2.21	2.77	6	1.69	2.95[e]	3.71
			31	1.68	2.00[c]	2.11
			67	1.44	1.44[c]	1.52
			88	1.34	1.29[d]	1.28
			107	1.28	1.07[d]	1.07
48.8	4.36	12.8	6	1.98	2.40[e]	3.71
			31	1.88	1.96[c]	2.11
			67	1.68	1.58[c]	1.52
			88	1.62	1.36[c]	1.28
			107	1.57	1.08[d]	1.07
50.6	12.2	103	6	2.74	2.62[g]	3.71
			31	2.7	2.57[g]	2.11
			67	2.64	2.05[e]	1.52
			88	2.6	1.45[c]	1.28
			107	2.54	-- [f]	1.07

a. D^*_f is the final drop position on the substrate at last observation time (about 10,000, 1000, and 120 μs for We of 2.77, 12.8, and 103, respectively).
b. D^*_e is the equilibrium drop position estimated from the equation of Ford and Furmidge [28], using equilibrium contact angle measured for millimeter-size drop.
c. Slope of D^* curve appears to be zero at last observation time (see Figures 5-4, 5-5 and 5-6), and position appears to be the equilibrium position, which is different from D^*_e.
d. Slope of D^* curve appears to be zero at last observation time (see Figures 5-4, 5-5 and 5-6), and position appears to be the equilibrium position, and ≈ D^*_e.
e. Slope of D^* curve appears to be nonzero at last observation time (see Figures 5-4, 5-5 and 5-6), and position appears not to be the equilibrium position.
f. Drop rebounded.
g. Slope of D^* curve appears to be zero at last observation time (see Figure 5-6), and position appears not to be the equilibrium position.

last observation time (see Figures 5-6); however, the observation time is only ≈ 120 μs. We believe that the spreading has paused as observed for We = 2.77 for the highly hydrophobic surface, and D^* will increase for longer observation time.

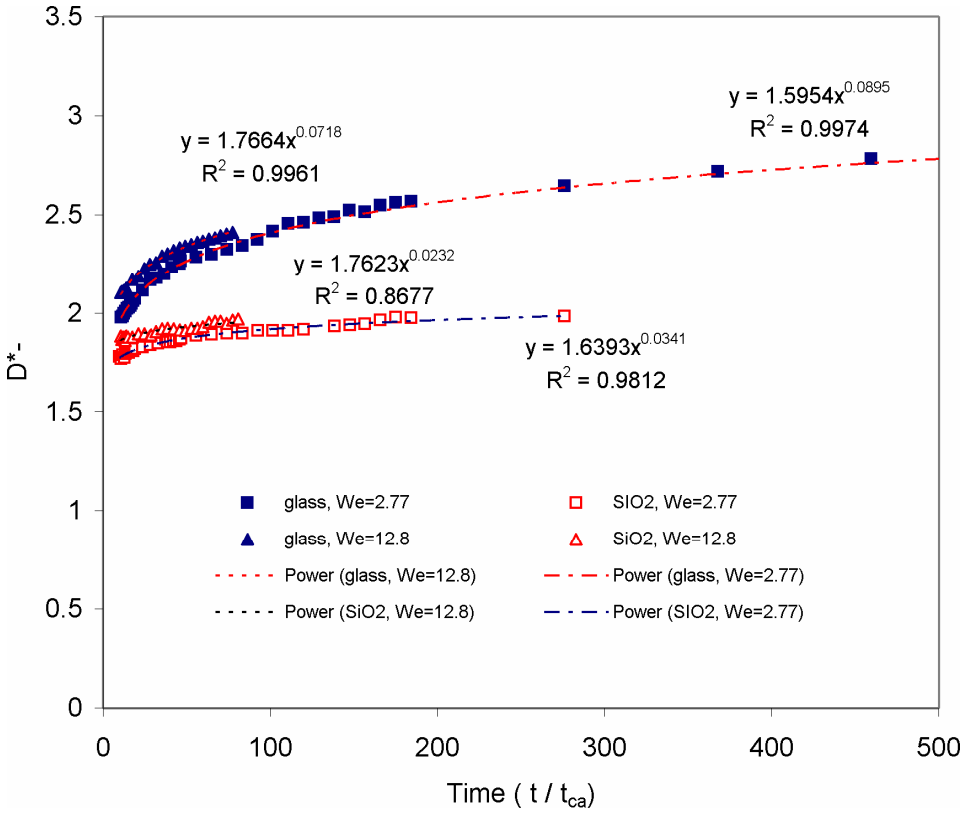

Figure 5-10: Drop spreading on substrates with low θ: glass slide, θ = 6˚, and SiO_2 wafer, θ = 31˚. The time is scaled by the capillary time $t_{ca} = (\rho D_0^3 \gamma)^{1/2}$, also shown in Table 5-2.

5.4 Instability Related to Drop Impaction on Substrates

Two phenomena due to Rayleigh-Taylor instability are often encountered during millimeter-drop impaction on substrates: fingering, which refers to evolution of the frontal undulations during the spreading of the liquid layer; and splashing, where the crown created after drop impaction breaks up into smaller secondary droplets. Fingering and splashing are related to Re, Oh, the roughness of substrates, and properties of the surrounding fluid [56, 63, 84, 90].

Under the conditions of the present study, the spreading drop exhibits a smooth round shape during the whole deformation process. No fingering or splashing was observed (see Figures 5-1 to 5-3). However, another event that is often encountered for inkjet deposition, a drop impacts on a liquid film from a previous drop, was observed. We recorded a water drop with a speed of 15.1 m/s and a diameter of 46.5 μm impacting a water film left by a previous drop on a SiO_2 wafer. The scenario of crown formation is shown in Figure 5-11, with an interframe time of 1 μs. The whole process from the drop reaching the film to crown formation and retraction to the film lasts about 20 μs. The variations of the crown height and diameter with time are plotted in Figure 5-12. During the whole process, the crown does not show any instability along its rim, i.e., no fingering or splashing was observed. According to the criteria of Cossaali et al. [15], splashing occurs if K (= $We \cdot Oh^{-2/5}$) [56], a dimensionless parameter, is greater than a critical value, $K_s = 2100 + 5880\ H^{1.44} = 3195$, where H = thickness of liquid layer/D_0. For the present experiments, H = 0.3 and thus $K_s = 3195$. Since K = 778, which is much smaller than K_s, the criteria of Cossaali et al. correctly predicts that splashing will not occur for our micron-scale experiments. From Table 3-3, the maximum value of K in DOD inkjet

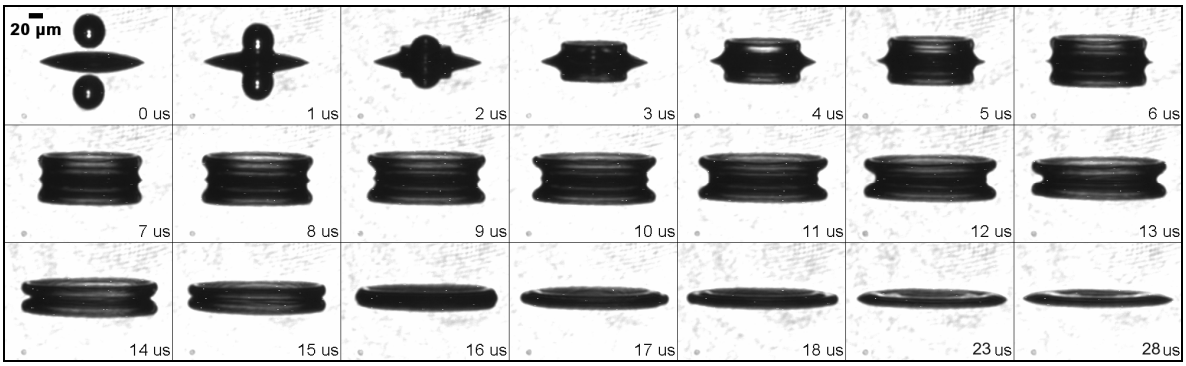

Figure 5-11: Growth and decay of crown formed by a water drop impacting on a water film left on a SiO_2 wafer by a previous drop (impact velocity = 15.1 m/s and drop diameter = 46.5 µm).

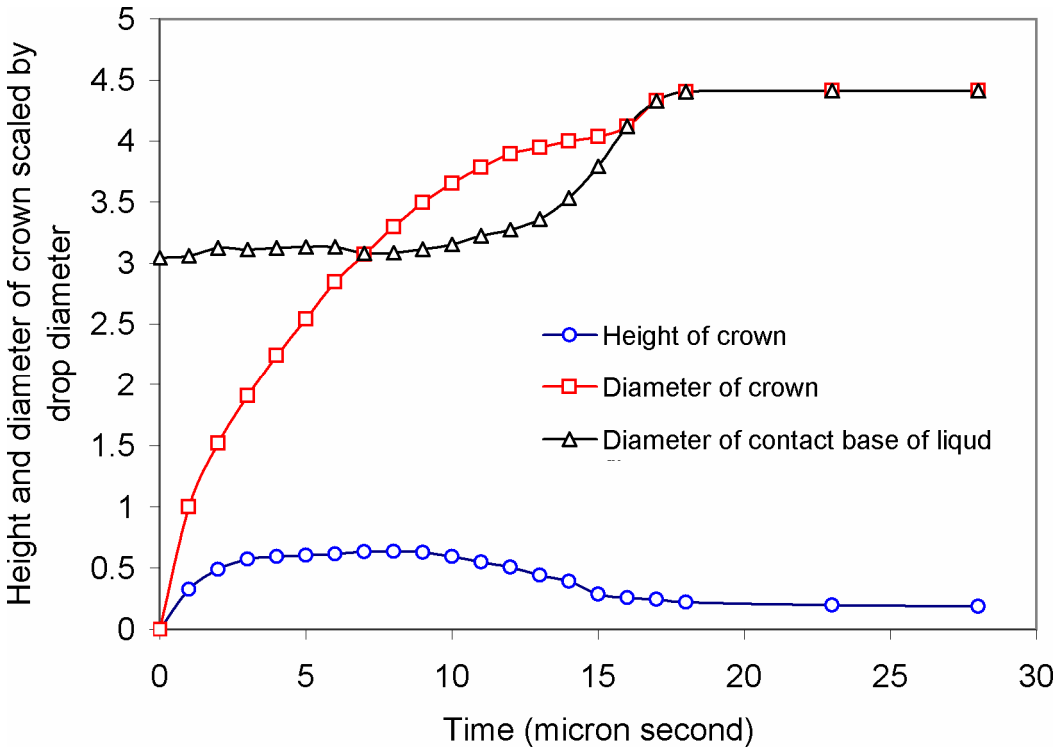

Figure 5-12: Height and diameter of crown vs. time, corresponding to Figure 5-13.

printing is less than 1600, which is much lower than the lowest possible value of K_s (2100 when H=0). If the model of Cossaali et al. is applicable for a micron-drop impaction on a liquid film, it can be concluded that splashing due to drop impaction on pre-existing liquid film will not occur for in inkjet printing, which is desirable for the applications of DOD inkjet printing. However, note that D^*_f after impaction on the film is larger than D^*_f for a single drop impacting a dry SiO_2 wafer.

5.5 Evaporation of Drops Deposited on Substrates

Drying of a liquid layer formed by the impaction of a micron-scale drop on a substrate was investigated. Single drops with diameter of 37.9 μm and impact speed of about 2.0 m/s were deposited on four substrates with different equilibrium contact angles, and photographs of the drops from impaction through drying were taken (see Figure 5-13). The variation of drop contact diameter and height, scaled by initial drop diameter, during drying are shown in Figure 5-14. Since the time for the liquid layer to dry (O (1) s) is relatively long compared to the time for the impaction process (O (10^{-4} to 10^{-2}) s), a camera capable of continuously photographing the process at a frame speed of 1000 fps was used. Since the interframe time is 1 ms, the impaction process is over in one frame for three of the substrates; however, the impaction process on the highly hydrophilic surface (contact angle of 6º) last longer as can be observed in Figures 5- 13a and 5-14.

The images in Figure 5-13 show the evolution of the drop profile on the four substrates. After the impaction process is completed and little evaporation has occurred, the shape of the drop is close to a spherical cap. At the early stage of evaporation on the hydrophilic surfaces (see Figure 5-13 b and c), the contact base of drop remains constant, while the height of the drop decreases gradually. Thus, the contact angle of the drop on the substrate decreases with the evaporation of liquid. Near the end of drying, the contact base of the drop begins to recede asymmetrically. At the beginning of evaporation on the hydrophobic surface, the contact line of the drop recedes and the drop height decreases simultaneously, with the contact angle of drop on the surface varying insignificantly. However, near the end of drying, the behavior is similar to that on hydrophilic surfaces: the contact angle of the drop on the substrate decreases with the evaporation of liquid, and then the contact base of the drop recedes asymmetrically.

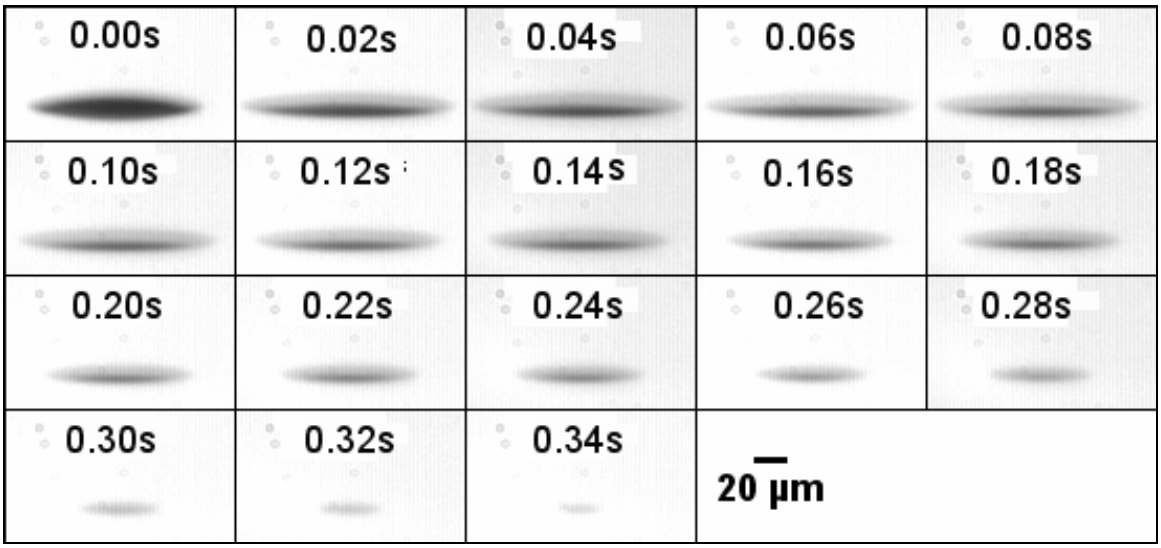

a) Contact angle = 6˚

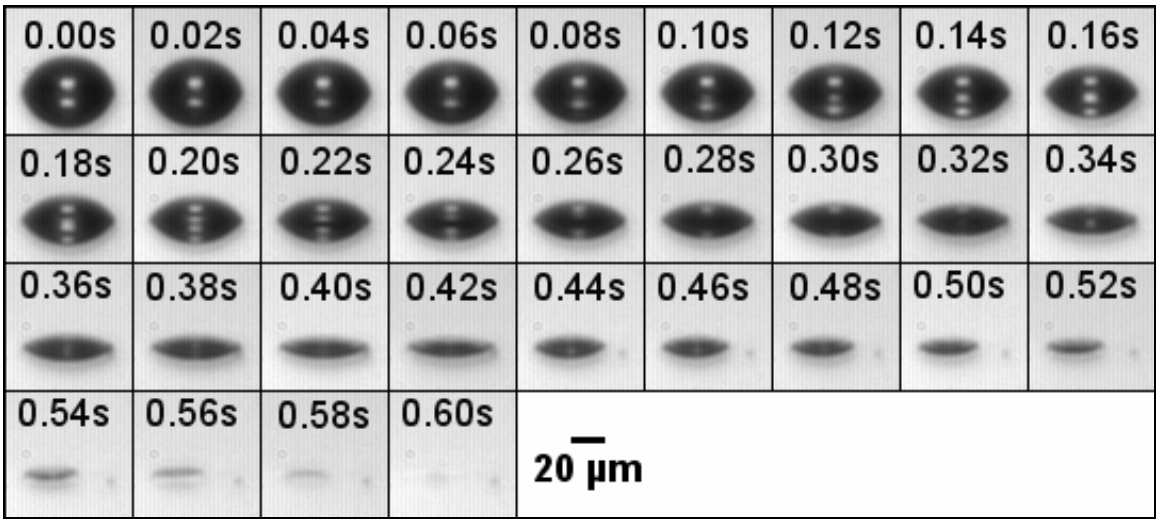

b) Contact angle = 67˚

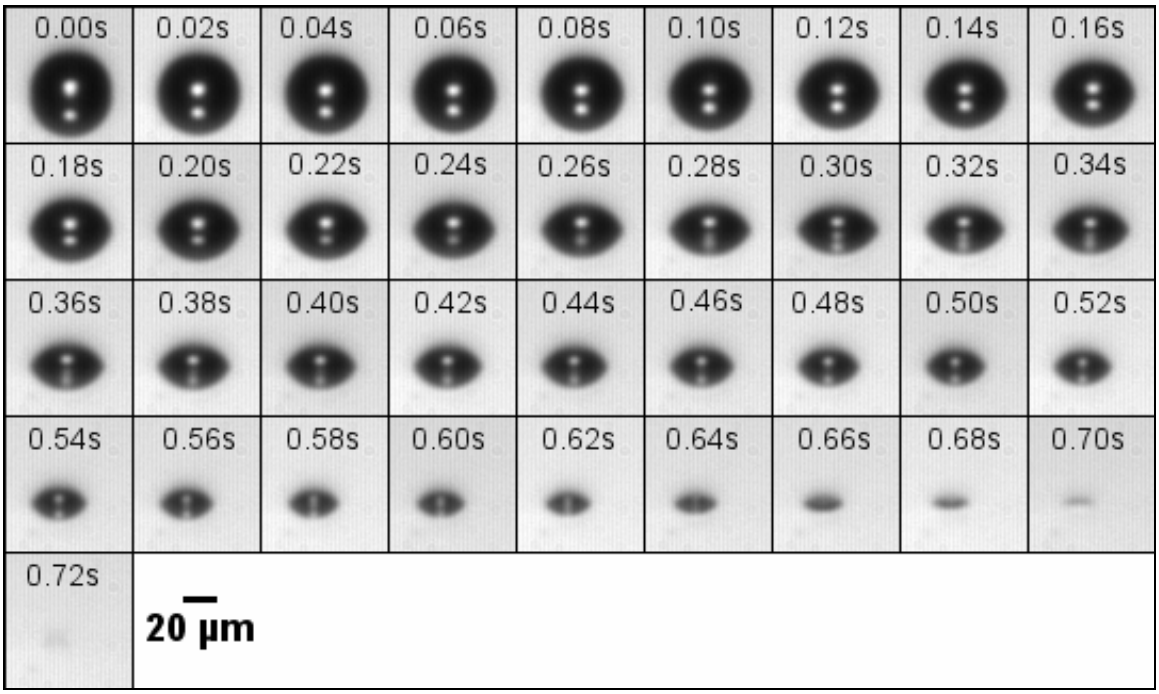

c) Contact angle = 88˚

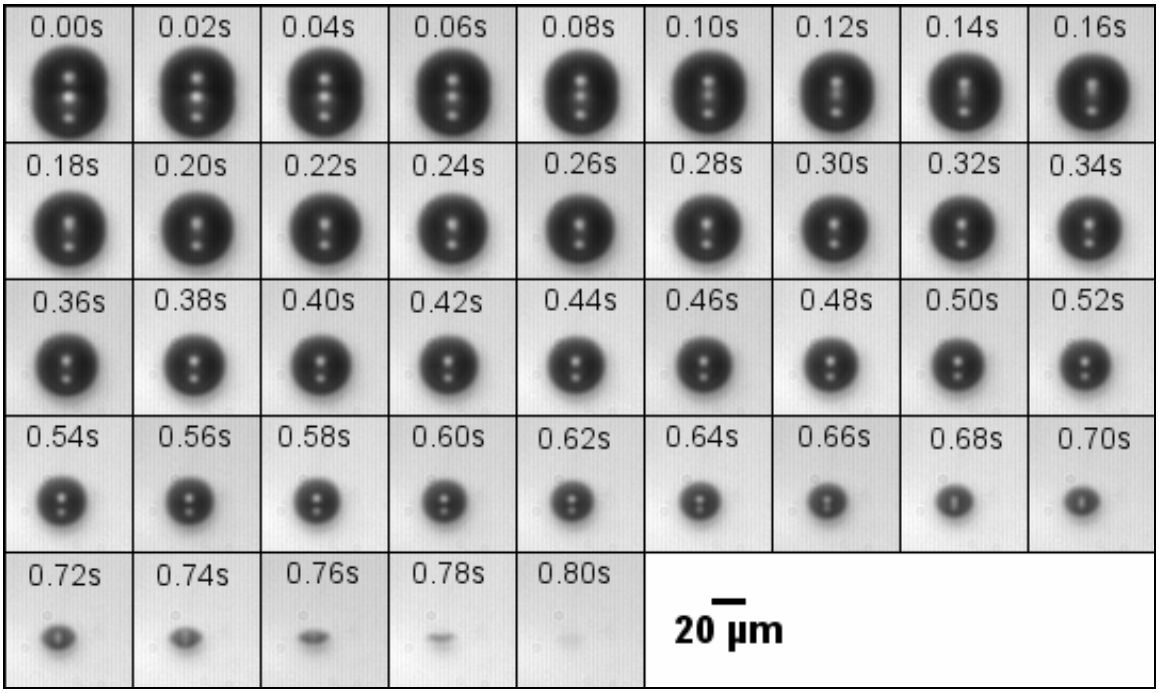

d) Contact angle = 107˚

Figure 5-13: Photographs of drops from impaction through drying on four substrates (drop size = 37.9 µm).

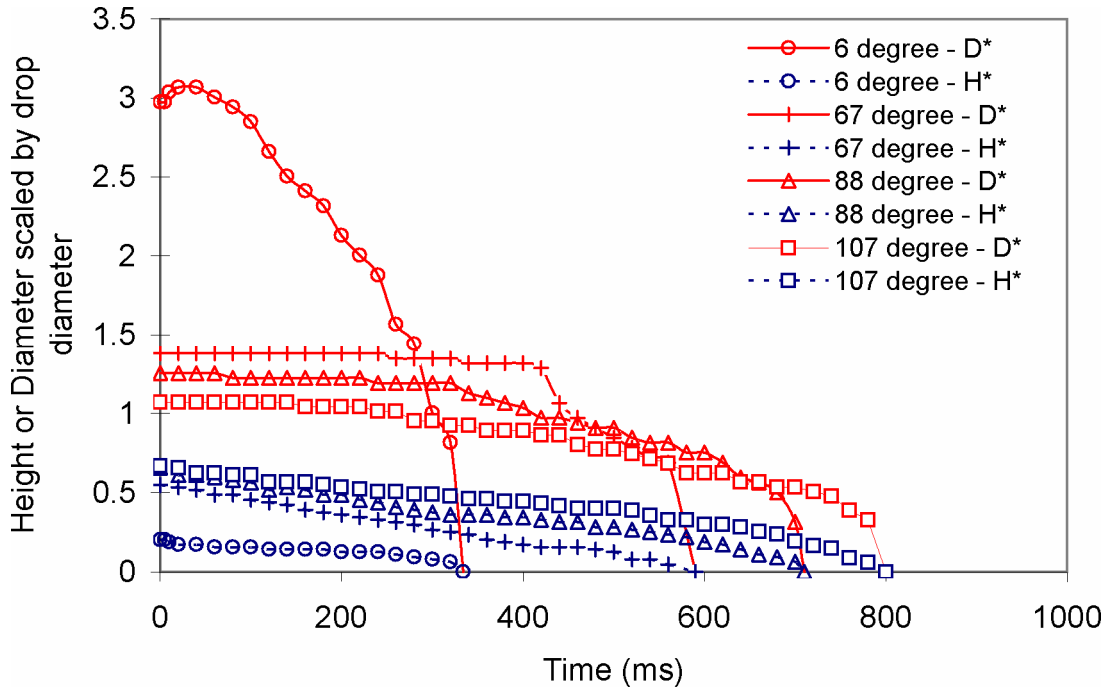

Figure 5-14: Variation of dimensionless drop contact diameter and height during drying.

The whole drying process on all of the substrates last less than one second. With decreasing contact angle, surface area over which evaporation occurs increases, and the total time for the drop to evaporate thus decreases, as can be see in Figure 5-14.

5.6 Comparison between Micron-Drop and Millimeter-Drop Impactions

In order to identify the effect of drop size on the drop impaction process and to determine the validity of scaling the drop impaction process from millimeter scale to micron scale, we conducted millimeter-size drop impaction tests with the same We and Oh and almost the same $cos\theta$ as those for the micron-drop impaction tests discussed in the previous sections. The results for the millimeter drops (D_0 = 2.23 mm) are compared with those for the micron drops (D_0 = 40.9 – 50.5 μm) in Figures 5-15, 5-16, and 5-17, where the diameter of the contact area is scaled by D_0 and time is scaled by D_0/U_0 (4.1 – 18.5 μs and 1.33 - 8.26 ms for micron drops and millimeter drops, respectively). The mixture of glycerin and water used for the millimeter-drop impaction has a lower surface tension than the distilled water used for the micron-drop impaction, and the contact angles of the millimeter drop are slightly smaller than those of the micron drops on the same substrate (see Table 3-4).

As shown in Figures 5-15, 5-16, and 5-17, under the same We and Oh, the millimeter-drop and micron-drop impactions on same substrates exhibit a very similar evolution process from spreading, oscillation to the equilibrium status, except that the micron drops show a slightly lower D^* and retracts more strongly from D^*_{max}. During initial spreading, the millimeter-drop and micron-drop behaviors are almost identical. When spreading approaches D^*_{max}, the millimeter drops have a higher spreading ratio. The discrepancy in D^*_{max} for millimeter drops and the corresponding micron drops is about 10 % for most of the cases. The millimeter and micron drops start to recoil at almost the same moment, but the millimeter drop recoils less and slower than the corresponding micron drop. During relaxation, the oscillation cycles for the two sizes of drops are very close, and the decaying behaviors of the oscillation amplitudes are similar.

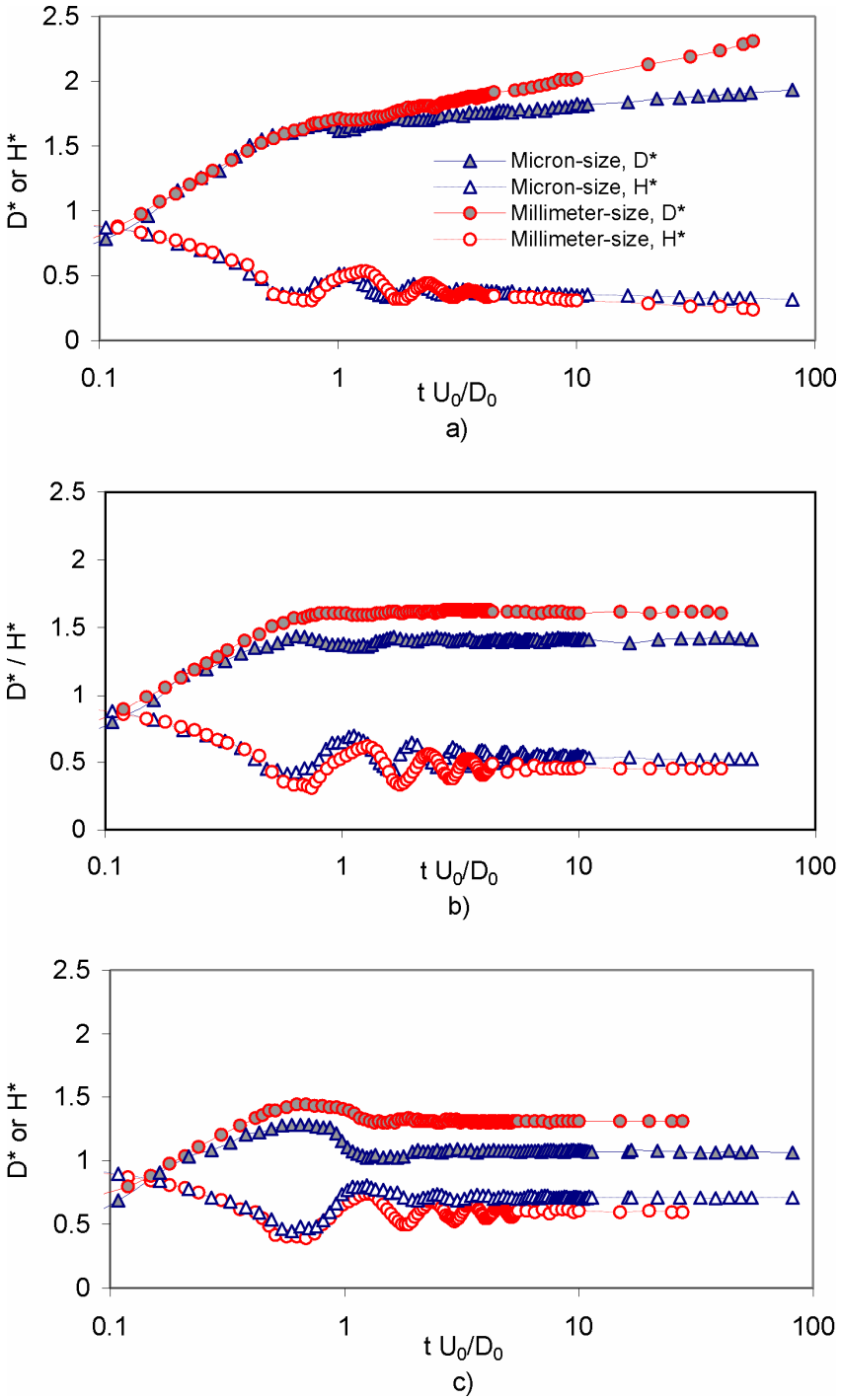

Figure 5-15: Comparison of dimensionless drop contact diameter and height for millimeter-drop and micron-drop impactions with We = 2.74, Oh = 0.0163 ~ 0.0165, and surfaces: a) SiO2 Wafer, θ = 31 and 24˚ for micron drop and millimeter drop, respectively; b) 9:1 OH/CH_3 SAM on gold coated silicon wafer, θ = 67 and 62˚ for micron drop and millimeter drop, respectively; c)100% CH_3 SAM on gold coated silicon wafer, θ = 107 and 99˚ for micron drop and millimeter drop, respectively.

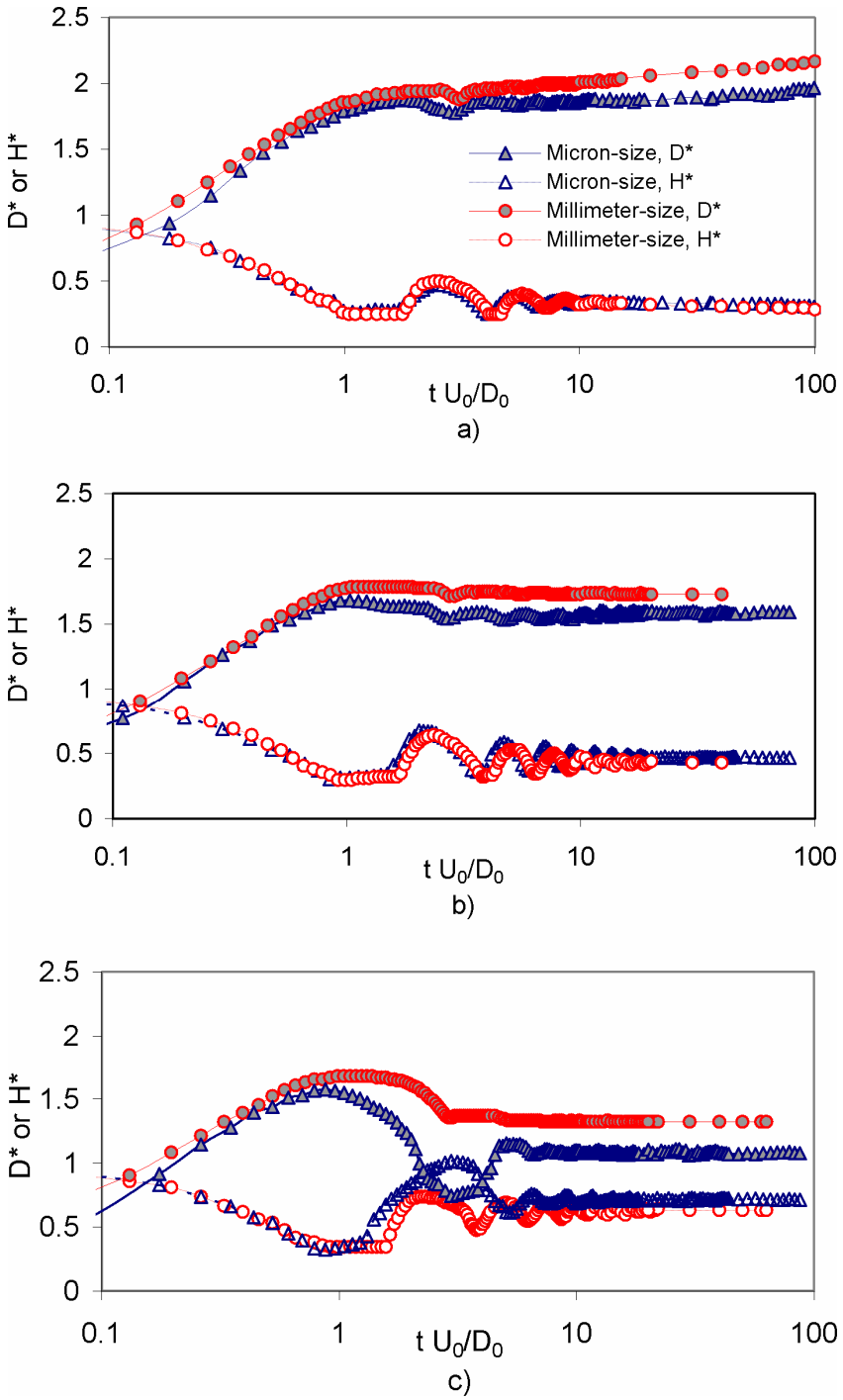

Figure 5-16: Comparison of dimensionless drop contact diameter and height for millimeter-drop and micron-drop impactions with We = 12.7 ~ 12.8, Oh = 0.0148 ~ 0.0151 and surfaces: a) SiO2 Wafer, θ = 31 and 24˚ for micron drop and millimeter drop, respectively; b) 9:1 OH/CH_3 SAM on gold coated silicon wafer, θ = 67 and 62˚ for micron drop and millimeter drop, respectively; c)100% CH_3 SAM on gold coated silicon wafer, θ = 107 and 99˚ for micron drop and millimeter drop, respectively.

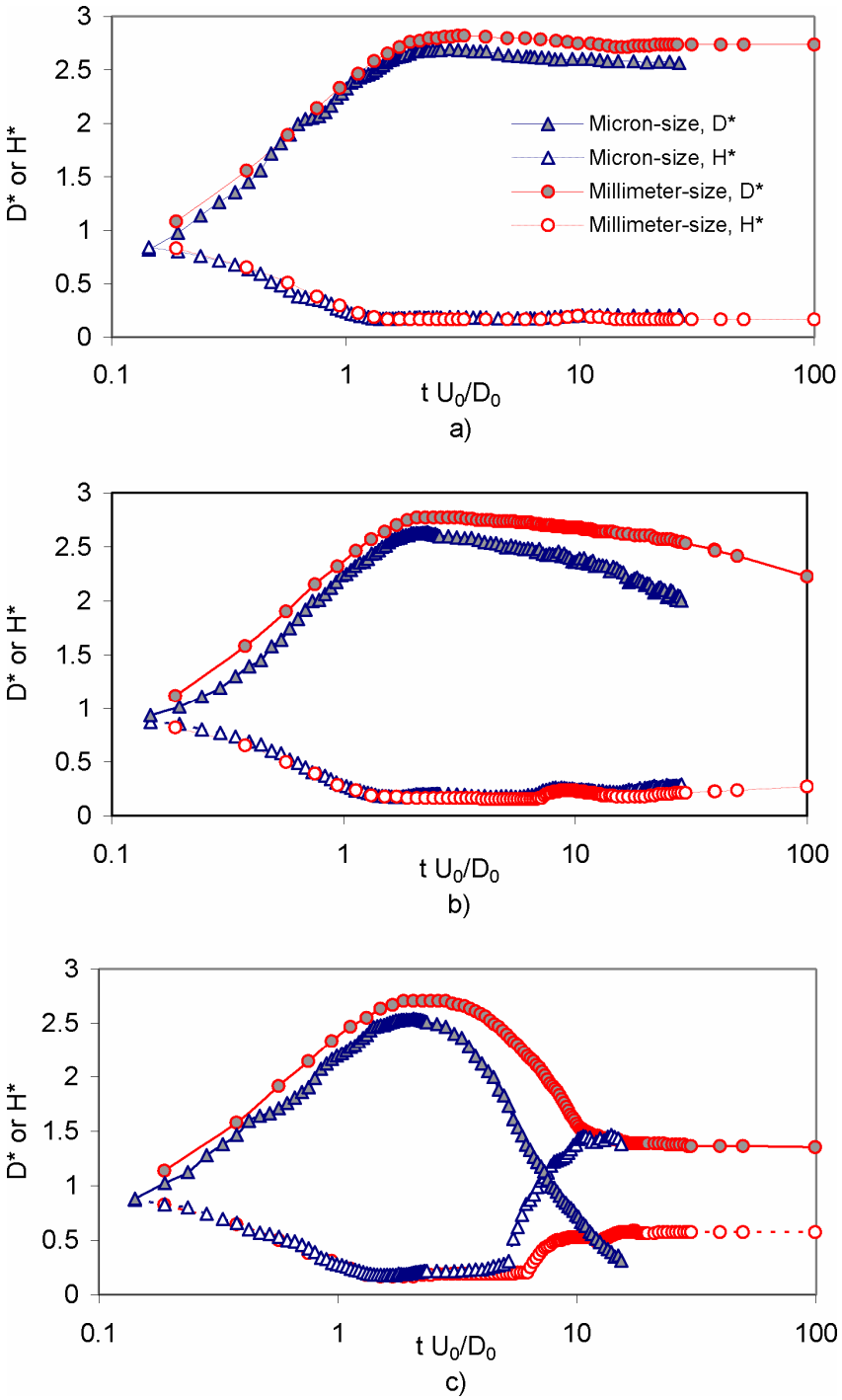

Figure 5-17: Comparison of dimensionless drop contact diameter and height for millimeter-drop and micron-drop impactions with We = 103 ~ 105, Oh = 0.0146 ~ 0.0148 and surfaces: a) SiO2 Wafer, θ = 31 and 24˚ for micron drop and millimeter drop, respectively; b) 9:1 OH/CH_3 SAM on gold coated silicon wafer, θ = 67 and 62˚ for micron drop and millimeter drop, respectively; c)100% CH_3 SAM on gold coated silicon wafer, θ = 107 and 99˚ for micron drop and millimeter drop, respectively.

At the final position of the drop on the substrate, D^*_f of the millimeter drop is larger than that of the micron drop.

Two plausible reasons for the differences in the D^* vs. t^* curves for the millimeter and micron drops are: 1) The contact angle of the millimeter drop on a given substrate is lower than that of the micron drop; distilled water and mixtures of glycerin and water were used to generate the micron and millimeter drops, respectively; and 2) The role of gravity in millimeter-drop impaction is more significant than in micron-drop impaction.

One test was conducted where We and Oh were identical to those for the tests shown in Figure 5-17 c. The contact angles for the micron and millimeter drops were adjusted by varying the ratios of OH/CH_3 applied to the silicon wafer until the contact angles were 98 and 99° for the micron and millimeter drops, respectively. For the same We, Oh, and θ, the D* versus t* curves are closer and the difference in D^*_{max} is smaller (compare Figures 5-17 c and 5-18). However, difference between the micron-drop and millimeter-drop curves during the impaction process still exits. These observations suggest that differences in contact angle explains some of the differences in the micron- and millimeter-drop impaction results, but is not the only reason for the differences.

Froude number ($Fr = U_0^2/(r_0 g)$), the ratio of ratio of inertial forces to gravitational forces, is useful in showing the basis for the second reason. As shown in Table 5-4, Fr is much larger for the micron drops than that for the millimeter drops. Thus, the role of gravity in millimeter-drop impaction is more significant than in micron-drop impaction. For the impaction process of millimeter drops, especially during the spreading stage, the effect of gravity is not negligible when the impact speed is low. For example, at impact speed of 0.27 m/s, gravitational force is up to 15% of the inertial

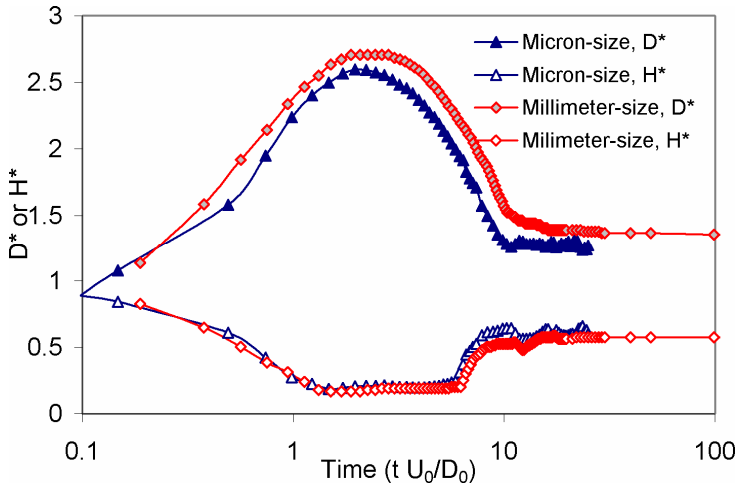

Figure 5-18: Comparison of millimeter-drop and micron-drop impaction at the same We = 103-105, Oh = 14.6 – 14.8 and θ = 98 -99°.

Table 5-4: Comparison of Froude and Bond numbers for millimeter-size and micron-size drops under the same We and Oh.

Regime	Impact velocity (m/s)	Drop size (μm)	Fr	Bo
Micron-size	2.21	40.9	2.44×10^{4}	2.28×10^{-4}
	4.36	48.8	7.95×10^{4}	3.24×10^{-4}
	12.2	50.5	6.01×10^{4}	3.47×10^{-4}
Millimeter-size	0.27	2230	6.67	0.82
	0.58	2230	30.8	
	1.67	2230	255	

force. Therefore, the effect of gravity leads to a larger D^*_{max} for millimeter drops than for micron drops. Moreover, the Bond number, $Bo = \rho g D_0^2/\gamma$, the ratio of gravitational to surface force, is about 0.82 for millimeter-size drops, but only $O(10^{-4})$ for micron drops, suggesting that gravity can not be neglected and slightly flattens the millimeter-size drops, causing the final resting dimensionless contact diameter to be larger.

CHAPTER 6

CONCLUSIONS AND RECOMMENDATIONS

We experimentally examined the dynamics of DOD drop formation and micron-drop impaction on well-characterized surfaces. The parameters were selected in the typical range of DOD inkjet printing. In this chapter, we will summarize the conclusions based on experimental results and give some recommendations for future work.

6.1 Conclusions

An apparatus has been developed for visualizing DOD drop formation and impaction on substrates, for drop sizes and impaction speeds of the magnitudes encountered in application. Using a pulsed laser, a motorized stage, a CCD camera, an inkjet head, signal generators and other control devices, sharp images with sufficient temporal resolution have been obtained. Several steps are taken to minimize the "first drop problem" so that excellent reproducibility is achieved. Through the present experimental setup, the processes of DOD drop formation and deposition can be recorded with sufficient temporal and spatial accuracy to allow comparisons against numeric and facilitate engineering design.

DOD Drop Formation A typical process of DOD drop formation consists of several stages: ejection and stretching of liquid, pinch-off of liquid thread from the nozzle exit, contraction of liquid thread, breakup of liquid thread into primary drop and satellites, recombination of primary drop and satellites, and drop oscillation to equilibrium state. During the ejection stage, the ejection speed increases with the driving signal voltage or lower viscosity of liquids and surface tension is insignificant. Our experiments indicate that the first breakup time, t_{b1}, at which the liquid pinches off from

the nozzle exit and becomes a free liquid thread, is related to liquid properties as well as the signal waveform. An abrupt pinch-off from the nozzle can be initiated by a larger negative pressure in the fluid chamber, which is tunable through the driving signal waveform. After pinch-off from the nozzle exit, the free liquid thread contracts and further (or second) breakup may occur, producing a primary drop and satellite(s). Two modes of the second breakup are observed in our experiments: end-pinching where the liquid thread pinches off from an almost spherical head, and multiple breakup due to capillary waves. For water threads, end-pinching occurs for the low voltage signal (19.6 volts), and multiple breakups occur for the high voltage signal (21.6, 23.6 and 25.6 volts). For the 5-cP liquid threads, only one end-pinching occurs for all the voltages. The first and second breakup times can be approximated by $t_b \sim t_{ca} / \alpha_{\max}^*$, but the proportionality constants are different for the two breakups due to their different mechanisms. The pinch-off of the liquid thread from the nozzle exit (the first breakup) occurs during stretching of the liquid thread. If end-pinching (the second breakup) takes place, it occurs during contraction of the thread. The maximum limit for the free thread length without breakup is approximately $\zeta / \alpha_{\max}^* + 2$ with ζ near unity. During the contraction of liquid thread, the retreating speed of the liquid thread tail is mainly determined by capillary speed, v_{ca}. If breakup of the free liquid thread occurs, the primary drop and satellite are formed. A necessary condition for the recombination of the primary drop and satellite is that $v_p < a v_{ca}$, where the value of a for our experiments is between 2.8 and 3.6. The primary drop and satellites size depend on the liquid properties and driving signal. As the driving voltage increases, the primary drop speed increases, but drop size is not significantly affected; however, as surface tension increases and/or viscosity decreases, the primary drop size increases. Increasing driving voltage leads to larger satellites, and may produce satellites that do not recombine with the primary drop.

Micron-drop impaction Our results indicate that scaling of micron-drop impactions from millimeter-drop impaction, based on the dimensionless numbers Oh, We and cosθ, is valid. Plots of D^* vs. tD_0/U_0 and H* vs. tD_0/U_0 for micron and millimeter drops at the same dimensionless numbers are similar except that D* of millimeter drops is usually slightly larger during the whole process. The discrepancy is ascribed mainly to the effect of gravity. For the millimeter drop, the role of gravity in impaction is more significant than for the micron drop.

The experimental results for micron-drop impaction show that the initial spreading is dominated by We and Oh, with negligible effects of θ. As spreading continues, the effect of θ becomes pronounced, and D^*_{max} increases with θ; however, for high-We impaction (103), the effect of θ on D^*_{max} is less significant than for low-We impaction (2.77 and 12.8). Existing models for predicting D^*_{max} give good predictions with deviations less than 10% from present experimental results for high-We impaction (We=103), even though most of these models were built based on the millimeter-drop impaction experiments. For low-We impaction, the predictions of most of these models do not agree well with present experimental results, especially on the low-contact angle surfaces. However, the model of Park, et al. [61] is an exception: it gives a good prediction (less than 10%) for high-We impaction as well as low-We impaction. The consideration of spontaneous spreading dissipation by this model indicates that the spontaneous spreading dissipation is not negligible, which is supported by our calculations. In addition, based on our results for micron drops, the dimensionless time to reach D^*_{max} is not a constant as used in several previous investigations, but ranges from 0.6 to 2.99, depending on We and contact angle.

Drop retraction from D^*_{max} depends on the We as well as θ: For hydrophilic surfaces, the retraction height decreases as We increases; but, on the contrary, for hydrophobic surfaces, the retraction height increases with We, and rebounding occurs

when We exceeds a critical value. The rebounding model of Mao's et al. [54] correctly predicts rebounding in present experiments for most cases. On the very hydrophilic surfaces, D* reaches a local maximum, slightly retracts, and then increases. Spreading, driven by wettability, follows the form $D^* = gt^n$, where g and n are two constants related to We and θ, respectively. The final drop position, D^*_f, increases with both θ and We.

Fingering and splashing do not occur in present experiments on dry solid substrates as well as liquid film. In the drop impaction on the liquid film, a crown was formed, but did not breakup into droplets. For dimensionless parameters typically of DOD inkjet printing, splashing criteria of Cossalli et al. [15] indicates that splashing will not occur for DOD inkjet printing. Micron drops evaporate very rapidly (< 1 second) on substrates in atmospheric air in the present experiments. Drying time increases as θ increases.

6.2 Recommendations

The system developed in this dissertation research can be used not only to investigate the dynamics of DOD drop formation and micron-size drop impaction on various substrates, but also to provide an approach to generate and track well-controlled micron-scale drops. The system can find applications in fields such as collision and coalescence of micron-droplets serving as a chemical reactor, simulation of aerosol-drug delivery in human lungs, evaporation and icing or solidification of drops, and droplet-based manufacturing [29].

DOD Drop Formation Our experiments are based on the low-viscosity Newtonian flow. These experimental results could be generalized in many applications of DOD generators because the normal working viscosity of liquids for DOD drop generators is less than 20 cP. However, in some applications, complex liquids, such as colloidal dispersions or macromolecular solutions, are used. The jetting of particle-laden liquid and macromolecular extends the application of DOD inkjet technology to the

deposition of solid material and other material with high profit. The effects of particles on drop formation and impaction have been experimentally investigated recently [33, 57], but the research is mainly for millimeter-size drops. Further investigation of effects of particles and macromolecular on the dynamics of DOD drop formation and impaction is needed.

What occurs inside the printhead, i.e., ink chamber and nozzle, is another interesting, but complicated, topic. Our present work examines the dynamics of liquid after the liquid is ejected from the nozzle, i.e., what occurs outside of the print head. The experimental results presented here can be instructive for ink design and deposition control; however, other factors must also be considered since successful ink should be compatible with the printhead and have good jettability. These capabilities are determined in part by factors including generation and propagation of pressure wave, acoustic response of ink chamber and channel to the pressure wave. In this field, many questions are still open: 1) How the pressure wave produced by the piezo transducer is related to driving signals (waveform); 2) How the liquid inside the printhead responds to the pressure acted by piezo transducer; and 3) What are effects of printhead geometry on pressure wave and velocity profile of liquids inside the printhead? The answers to these questions will greatly benefit the design of the inkjet printer and its applications.

Theoretical simulation on DOD drop formation is worthwhile to attempt. It also has good commercial value because it will make ink and printhead design easier if the simulation matches experimental results. The theoretical analysis of the dripping mode of drop formation has attracted many researchers, and great progress has been made. These achievements provide rich information to initiate theoretical simulation work on DOD drop formation. Some commercial software, such as flow-3D and Fluent, also show satisfying results in simulating free-surface fluid problems and could be the starting point for conducting simulation of DOD drop formation.

Micron-Drop Impaction. The effect of physical or chemical heterogeneousness of substrates on the drop impaction process needs further investigation. Like many previous studies [65, 90], the present study used smooth surfaces as the impacted substrate. Thus, a hypothesis was made: O (D_0/R_a) << 1 (R_a is the roughness amplitude of substrates), i.e., the effect of the surface roughness is negligible. This assumption is not valid in many applications of inkjet printing. However, some experimental studies based on millimeter-drop impaction found that roughness [63] or chemical heterogeneousness [49] of substrates played important roles on the initial spreading as well as the final status of deposition. Roughness could lower the critical values of splashing occurrence, while chemical heterogeneousness of substrates complicated the final profile of drops on the substrates. Those investigations on the effects of the roughness on the millimeter-drop impaction were mainly conducted on the roughness scale of O (R_a/D_0) < 1. For inkjet depositions on fabrics, a scale of O (R_a/D_0) ~1 should be more appropriate. With the introduction of physical or chemical heterogeneousness of surfaces, drop instability on substrates may occur, which is another interesting topic worthy of further investigation.

Drop drying is an old problem, but is significant in inkjet printing, especially for the accurate depositions of such functional material as LED, where an even and uniform film left by the drop is required. However, the effect of coffee ring [19] is detrimental to the formation of an even film. A study on how to generate an even film, should fully investigate the effects of parameters, such as substrate temperature, surrounding humidity, and evaporation rate of liquid, as well as the parameters related to drop impaction that have been discussed in the present study. Although a lot of literature has focused on the evaporation of the millimeter drops or films on various surfaces, the application of conclusions from the millimeter-drop studies to micron drops may not be valid due to the large difference in surface-to-volume ratios. The evaporation time for millimeter drops is about O (1) hour, while that of micron drops is about O (100) ms in present study. Thus the drying process of micron drops becomes very sensitive to the

parameters associated with heat and mass transfer [41]. These parameters need to be re-examined, and their role in the final film and dot formation determined. In addition, the effects of surfactants, particles and macromolecules on the drying process and final film formation are interesting topics open for investigation. They should be critical to the control of even film formed by inkjet printing deposition.

APPENDIX

A.1 Photographic Parameters

When a camera is used to capture a high-speed object, the exposure time is a very important parameter. For continuous photography, the exposure time is often limited by the camera shutter. For flash photography, the exposure time is equal to the flash duration while the shutter is open. Generally speaking, the exposure time should be as short as possible to arrest motion in the picture. A very short exposure time is often achieved through an expensive camera or illumination source. From the economical viewpoint, the maximum permissible exposure time to obtain a sharp image is required to be calculated before the experimental setup is built up. Thus the lowest power of illumination source can be approximated. In this section, we summarize calculations of these parameters.

1. Maximum Permissible Exposure Time, T_{exp}

An empirical expression often used to determine the maximum permissible exposure time, $\underline{T_{exp}}$, of a CCD camera follows [64]:

$$T_{\exp} = \frac{2 \times \text{Pixel size}}{V_r}$$

where V_r = object's velocity × magnification.

In the our experiments, pixel size = 9.9 μm, magnification is about 12.2, for an object with a speed of 10 m/s; thus,

$$T_{\exp} = \frac{2 \times 9.9 \times 10^{-6}}{10 \times 12.2} = 160\ ns.$$

2. Efficient Energy of Illumination to Saturate CCD Sensor, *E*

For a CCD camera, the energy required to saturate the CCD sensor can be calculated as follows:

The number of photons to saturate the CCD sensor is

N_p = FWC/QE

where FWC is the full well capacity of sensor, and QE is the quantum efficiency.

The corresponding illumination energy is

$E = N_p \times h\nu$

where h is Planck's constant, $6.63\times10^{-34} J \cdot s$, and $\nu = \frac{c}{\lambda}$ is the frequency of light, c is the speed of light and λ is the wavelength of light.

3. Power of Illumination to Saturate CCD Sensor, *P′*

Illumination Power, *P′*, to saturate the CCD sensor is

$P' = E / T_{exp}$

4. Lowest Power of Illumination for a High-Speed Imaging System, *P*

If the illumination efficiency is η, and magnification of the optical system is δ, then the required power of the continuous illumination source or flash is

$P = \delta^2 P'/\eta$.

REFERENCES

[1] ADAMS, R. L. and ROY, J., "A One-Dimensional Numerical-Model of a Drop-on-Demand Ink Jet," J. Appl. Mech-T ASME, vol. 53, pp. 193-197, 1986.

[2] ALTERAIFI, A. M., SHERIF, D., and MOET, A., "Interfacial effects in the spreading kinetics of liquid droplets on solid substrates," J. Colloid Interf. Sci., vol. 264, pp. 221-227, 2003.

[3] ASAI, A., SHIOYA, M., HIRASAWA, S., and OKAZAKI, T., "Impact of an Ink Drop on Paper," J. Imaging Sci. Techn., vol. 37, pp. 205-207, 1993.

[4] ATTINGER, D., ZHAO, Z., and POULIKAKOS, D., "An Experimental Study of Molten Microdroplet Surface Deposition and Solidification: Transient Behavior and Wetting Angle Dynamics," J. Heat Transfer, vol. 122, pp. 544-556, 2000.

[5] BAIN, C. D., TROUGHTON, E. B., TAO, Y. T., EVALL, J., WHITESIDES, G. M., and NUZZO, R. G., "Formation of Monolayer Films by the Spontaneous Assembly of Organic Thiols from Solution onto Gold," J. Am. Chem. Soc., vol. 111, pp. 321-335, 1989.

[6] BASARAN, O. A., "Small-scale free surface flows with breakup: Drop formation and emerging applications," AIChE J., vol. 48, pp. 1842-1848, 2002.

[7] BERTOLA, V., "Drop impact on a hot surface: effect of a polymer additive," Exp. Fluids., vol. 37, pp. 653-664, 2004.

[8] BIANCE, A. L., CLANET, C., and QUERE, D., "First steps in the spreading of a liquid droplet," Physical Review E, vol. 69, pp. 016301, 2004.

[9] BOGY, D. B., "Drop Formation in a Circular Liquid Jet," Ann. Rev. Fluid Mech., vol. 11, pp. 207-228, 1979.

[10] BRENNER, M. P., SHI, X. D., and NAGEL, S. R., "Iterated Instabilities during Droplet Fission," Phys. Rev. Lett., vol. 73, pp. 3391-3394, 1994.

[11] BUSSMANN, M., CHANDRA, S., and MOSTAGHIMI, J., "Modeling the splash of a droplet impacting a solid surface," Phys. Fluids, vol. 12, pp. 3121-3132, 2000.

[12] CALVERT, P., "Inkjet printing for materials and devices," Chem. Mater., vol. 13, pp. 3299-3305, 2001.

[13] CHANDRA, S. and AVEDISIAN, C. T., "On the Collision of a Droplet with a Solid-Surface," Proc. R. Soc. London, Ser. A, vol. 432, pp. 13-41, 1991.

[14] CHEN, A. U. and BASARAN, O. A., "A new method for significantly reducing drop radius without reducing nozzle radius in drop-on-demand drop production," Phys. Fluids, vol. 14, pp. L1-L4, 2002.

[15] COSSALI, G. E., COGHE, A., and MARENGO, M., "The impact of a single drop on a wetted solid surface," Exp. Fluids., vol. 22, pp. 463-472, 1997.

[16] CREAGH, L. T. and MCDONALD, M., "Design and performance of inkjet print heads for non-graphic-arts applications," MRS Bull., vol. 28, pp. 807-811, 2003.

[17] CROOKS, R., COOPER-WHITEZ, J., and BOGER, D. V., "The role of dynamic surface tension and elasticity on the dynamics of drop impact," Chem. Eng. Sci., vol. 56, pp. 5575-5592, 2001.

[18] DE GANS, B. J., DUINEVELD, P. C., and SCHUBERT, U. S., "Inkjet printing of polymers: State of the art and future developments," Advanced Materials, vol. 16, pp. 203-213, 2004.

[19] DEEGAN, R. D., BAKAJIN, O., DUPONT, T. F., HUBER, G., NAGEL, S. R., and WITTEN, T. A., "Capillary flow as the cause of ring stains from dried liquid drops," Nature, vol. 389, pp. 827-829, 1997.

[20] DEGENNES, P. G., "Wetting - Statics and Dynamics," Rev. Mod. Phys., vol. 57, pp. 827-863, 1985.

[21] DIJKSMAN, J. F., "Hydrodynamics of Small Tubular Pumps," J. Fluid Mech., vol. 139, pp. 173-191, 1984.

[22] DORING, M., "Ink-jet Printing," Philips Tech. Rev., vol. 40, pp. 192-198, 1982.

[23] EGGERS, J., "Universal Pinching of 3D Axisymmetrical Free-Surface Flow," Phys. Rev. Lett., vol. 71, pp. 3458-3460, 1993.

[24] EGGERS, J., "Nonlinear dynamics and breakup of free-surface flows," Rev. Mod. Phys., vol. 69, pp. 865-929, 1997.

[25] EVANS, C. M., FOX, J. E., HALL, K. P., and GOODWIN, P. D., "Optimisation of Ink Jet Droplet Formation Through Polymer Selection," IS&T NIP 15, pp. 78-81, 1999.

[26] FEDORCHENKO, A. I. and WANG, A. B., "On some common features of drop impact on liquid surfaces," Phys. Fluids, vol. 16, pp. 1349-1365, 2004.

[27] FENG, J. Q., "A general fluid dynamic analysis of drop ejection in drop-on-demand ink jet devices," J. Imaging Sci. Techn., vol. 46, pp. 398-408, 2002.

[28] FORD, R. E., FURMIDGE, C. G. L., "Impact and spreading of spray drops on foliar surfaces," Wetting, Soc. Chem. Industry Monograph, vol. 25, pp. 417-432, 1967.

[29] FROHN, A. and ROTH, N., "Dynamics of droplets," 2000, Berlin ; New York: Springer. xi, 292 p.

[30] FROMM, J. E., "Numerical-Calculation of the Fluid-Dynamics of Drop-on-Demand Jets," IBM J. Res. Dev., vol. 28, pp. 322-333, 1984.

[31] FUKAI, J., ZHAO, Z., POULIKAKOS, D., MEGARIDIS, C. M., and MIYATAKE, O., "Modeling of the Deformation of a Liquid Droplet Impinging Upon a Flat Surface," Phys. Fluids a-Fluid, vol. 5, pp. 2588-2599, 1993.

[32] FUKAI, J., TANAKA, M., and MIYATAKE, O., "Maximum spreading of liquid droplets colliding with flat surfaces," J. Chem. Eng. Jpn., vol. 31, pp. 456-461, 1998.

[33] FURBANK, R. J. "Drop formation from particulate suspensions," Doctorial dissertation, Georgia Institute of Technology, Atlanta, 2004

[34] FURBANK, R. J. and MORRIS, J. F., "An experimental study of particle effects on drop formation," Phys. Fluids, vol. 16, pp. 1777-1790, 2004.

[35] GOEDDE, E. F. and YUEN, M. C., "Experiments on Liquid Jet Instability," J. Fluid Mech., vol. 40, pp. 495-511, 1970.

[36] GU, Y. G. and LI, D. Q., "A model for a liquid drop spreading on a solid surface," Colloids and Surfaces a-Physicochemical and Engineering Aspects, vol. 142, pp. 243-256, 1998.

[37] HARDALUPAS, Y., TAYLOR, A. M. K. P., and WILKINS, J. H., "Experimental investigation of sub-millimetre droplet impingement onto spherical surfaces," International Journal of Heat and Fluid Flow, vol. 20, pp. 477-485, 1999.

[38] HEINZL, J. and HERTZ, C. H., "Ink-Jet Printing," Adv. Imag. Electr. Phys., vol. 65, pp. 91-171, 1985.

[39] HENDERSON, D., SEGUR, H., SMOLKA, L. B., and WADATI, M., "The motion of a falling liquid filament," Phys. Fluids, vol. 12, pp. 550-565, 2000.

[40] HENDERSON, D. M., PRITCHARD, W. G., and SMOLKA, L. B., "On the pinch-off of a pendant drop of viscous fluid," Phys. Fluids, vol. 9, pp. 3188-3200, 1997.

[41] IKEGAWA, M. and AZUMA, H., "Droplet behaviors on substrates in thin-film formation using ink-jet printing," Jsme International Journal Series B-Fluids and Thermal Engineering, vol. 47, pp. 490-496, 2004.

[42] KANG, H. R., "Water-Based Ink-Jet Ink .3. Performance Studies," J. Imaging Sci., vol. 35, pp. 195-201, 1991.

[43] KELLER, J. B., "Breaking of Liquid-Films and Threads," Phys. Fluids, vol. 26, pp. 3451-3453, 1983.

[44] KIM, H. Y. and CHUN, J. H., "The recoiling of liquid droplets upon collision with solid surfaces," Phys. Fluids, vol. 13, pp. 643-659, 2001.

[45] KIM, H. Y., PARK, S. Y., and MIN, K., "Imaging the high-speed impact of microdrop on solid surface," Rev. Sci. Instrum., vol. 74, pp. 4930-4937, 2003.

[46] KOWALEWSKI, T. A., "On the separation of droplets from a liquid jet," Fluid Dyn. Res., vol. 17, pp. 121-145, 1996.

[47] LE, H. P., "Progress and trends in ink-jet printing technology," J. Imaging Sci. Techn., vol. 42, pp. 49-62, 1998.

[48] LEE, H. J. and KIM, H. Y., "Control of drop rebound with solid target motion," Phys. Fluids, vol. 16, pp. 3715-3719, 2004.

[49] LEOPOLDES, J., DUPUIS, A., BUCKNALL, D. G., and YEOMANS, J. M., "Jetting micron-scale droplets onto chemically heterogeneous surfaces," Langmuir, vol. 19, pp. 9818-9822, 2003.

[50] LEVIN, Z. and HOBBS, P. V., "Splashing of Water Drops on Solid and Wetted Surfaces - Hydrodynamics and Charge Separation," Philosophical Transactions of the Royal Society of London Series A-Mathematical and Physical Sciences, vol. 269, pp. 555-585, 1971.

[51] LIN, S. P. and REITZ, R. D., "Drop and spray formation from a liquid jet," Ann. Rev. Fluid Mech., vol. 30, pp. 85-105, 1998.

[52] LOPEZ, B., VADILLO, D., PIERRON, P., and SOURCEMARIANADIN, A., "Transient Phenomena During Drop Formation in DOD Printing," IS&T NIP, vol. 18, pp.170-175, 2002.

[53] LOPEZ, J., MILLER, C. A., and RUCKENSTEIN, E., "Spreading Kinetics of Liquid-Drops on Solids," J. Colloid Interf. Sci., vol. 56, pp. 460-468, 1976.

[54] MAO, T., KUHN, D. C. S., and TRAN, H., "Spread and rebound of liquid droplets upon impact on flat surfaces," AIChE J., vol. 43, pp. 2169-2179, 1997.

[55] MOUROUGOU-CANDONI, N., PRUNET-FOCH, B., LEGAY, F., VIGNES-ADLER, M., and WONG, K., "Retraction phenomena of surfactant solution drops upon impact on a solid substrate of low surface energy," Langmuir, vol. 15, pp. 6563-6574, 1999.

[56] MUNDO, C., SOMMERFELD, M., and TROPEA, C., "Droplet-Wall Collisions - Experimental Studies of the Deformation and Breakup Process," Int. J. Multiphas. Flow, vol. 21, pp. 151-173, 1995.

[57] NOTZ, P. K. and BASARAN, O. A., "Dynamics and breakup of a contracting liquid filament," J. Fluid Mech., vol. 512, pp. 223-256, 2004.

[58] OK, H. Y., "Effects of Paticles on Drop Impingement," Doctoral dissertation, Georgia Institute of Technology, Atlanta, 2005.

[59] PANTON, R. L., "Imcompressible Flow," John Wiley & Sons, Inc., New York, 1996.

[60] PARK, H., "Drop impingement and interaction with a solid surface," Georgia Institute of Technology, Atlanta, 2003.

[61] PARK, H., CARR, W. W., ZHU, J. Y., and MORRIS, J. F., "Single drop impaction on a solid surface," AIChE J., vol. 49, pp. 2461-2471, 2003.

[62] PASANDIDEHFARD, M., QIAO, Y. M., CHANDRA, S., and MOSTAGHIMI, J., "Capillary effects during droplet impact on a solid surface," Phys. Fluids, vol. 8, pp. 650-659, 1996.

[63] RANGE, K. and FEUILLEBOIS, F., "Influence of surface roughness on liquid drop impact," J. Colloid Interf. Sci., vol. 203, pp. 16-30, 1998.

[64] RAY, S. F. and BRITISH ASSOCIATION FOR HIGH SPEED PHOTOGRAPHY., "High speed photography and photonics," Bellingham, Wash.: SPIE Press. xxi, 402 p., 2002.

[65] RAYLEIGH, L., "On the instability of jets," Proc. London Math. Soc., vol. 10, pp. 4-13, 1879.

[66] REIN, M., "Phenomena of Liquid-Drop Impact on Solid and Liquid Surfaces," Fluid Dyn. Res., vol. 12, pp. 61-93, 1993.

[67] REIS, N., AINSLEY, C., and DERBY, B., "Ink-jet delivery of particle suspensions by piezoelectric droplet ejectors," J. Appl. Phys., vol. 97, pp. 094903, 2005.

[68] REMBE, C., PATZER, J., HOFER, E. P., and KREHL, P., "Realcinematographic visualization of droplet ejection in thermal ink jets," J. Imaging Sci. Techn., vol. 40, pp. 400-404, 1996.

[69] REMBE, C., WIESCHE, S. A. D., BEUTEN, M., and HOFER, E. P., "Investigations of nonreproducible phenomena in thermal ink jets with real high-speed cine photomicrography," J. Imaging Sci. Techn., vol. 43, pp. 325-331, 1999.

[70] RICHARD, D. and QUERE, D., "Bouncing water drops," Europhys. Lett., vol. 50, pp. 769-775, 2000.

[71] RIOBOO, R., BAUTHIER, C., CONTI, J., VOUE, M., and DE CONINCK, J., "Experimental investigation of splash and crown formation during single drop impact on wetted surfaces," Exp. Fluids., vol. 35, pp. 648-652, 2003.

[72] ROZHKOV, A., PRUNET-FOCH, B., and VIGNES-ADLER, M., "Impact of drops of polymer solutions on small targets," Phys. Fluids, vol. 15, pp. 2006-2019, 2003.

[73] SCHELLER, B. L. and BOUSFIELD, D. W., "Newtonian Drop Impact with a Solid-Surface," AIChE J., vol. 41, pp. 1357-1367, 1995.

[74] SCHIAFFINO, S. and SONIN, A. A., "Molten droplet deposition and solidification at low Weber numbers," Phys. Fluids, vol. 9, pp. 3172-3187, 1997.

[75] SCHULKES, R. M. S. M., "The contraction of liquid filaments," J. Fluid Mech., vol. 309, pp. 277-300, 1996.

[76] SHI, X. D., BRENNER, M. P., and NAGEL, S. R., "A Cascade of Structure in a Drop Falling from a Faucet," Science, vol. 265, pp. 219-222, 1994.

[77] SHIELD, T. W., BOGY, D. B., and TALKE, F. E., "A Numerical Comparison of One-Dimensional Fluid Jet Models Applied to Drop-on-Demand Printing," J. Comput. Phys., vol. 67, pp. 327-347, 1986.

[78] SIKALO, S., TROPEA, C., and GANIC, E. N., "Impact of droplets onto inclined surfaces," J. Colloid Interf. Sci., vol. 286, pp. 661-669, 2005.

[79] SIRRINGHAUS, H. and SHIMODA, T., "Inkjet printing of functional materials," MRS Bull., vol. 28, pp. 802-803, 2003.

[80] SLAYTER, E. M. and SLAYTER, H. S., "Light and electron microscopy," Cambridge [England] ; New York: Cambridge University Press. xvi, 312 p., 1992

[81] STONE, H. A., BENTLEY, B. J., and LEAL, L. G., "An Experimental-Study of Transient Effects in the Breakup of Viscous Drops," J. Fluid Mech., vol. 173, pp. 131-158, 1986.

[82] SUBRAMANI, H. J., YEOH, H. K., SURYO, R., XU, Q., AMBRAVANESWARAN, B., and BASARAN, O. A., "Simplicity and complexity in a dripping faucet," Phys. Fluids, vol. 18, pp. 032106, 2006.

[83] TANNER, L. H., "Spreading of Silicone Oil Drops on Horizontal Surfaces," Journal of Physics D-Applied Physics, vol. 12, pp. 1473-1484, 1979.

[84] THORODDSEN, S. T. and SAKAKIBARA, J., "Evolution of the fingering pattern of an impacting drop," Phys. Fluids, vol. 10, pp. 1359-1374, 1998.

[85] TIMMERMANS, J., "The physico-chemical constants of binary systems in concentrated solutions," Interscience. New York, 4 v. 1959.

[86] VAN DAM, D. B. and LE CLERC, C., "Experimental study of the impact of an ink-jet printed droplet on a solid substrate," Phys. Fluids, vol. 16, pp. 3403-3414, 2004.

[87] WALLACE, D. B. and HAYES, D. J., "Solder Jet-Optics Jet-Aroma Jet-Reagent Jet-Tooth Jet and other Applications of Ink-jet printing Technology," IS&T NIP 18, pp. 228-235, 2002.

[88] WORTHINGTON, A. M., "On the Forms Assumed by Drops of Liquids Falling Vertically on a Horizontal Plate," Proc. R. Soc. London, vol. 25, pp. 261-272, 1877.

[89] WORTHINGTON, A. M., "A Second Paper on the Forms Assumed by Drops of Liquids Falling Vertically on a Horizontal Plate," Proc. R. Soc. London, vol. 25, pp. 498-503, 1877.

[90] XU, L., ZHANG, W. W., and NAGEL, S. R., "Drop splashing on a dry smooth surface," Phys. Rev. Lett., vol. 94, pp. 184505, 2005.

[91] YARIN, A. L., "Drop impact dynamics: Splashing, spreading, receding, bouncing..." Ann. Rev. Fluid Mech., vol. 38, pp. 159-192, 2006.